

## Development of Iridium-based Nanostructures for Oxygen Evolution Reaction in PEM Water Electrolysis

Seongeun Park

Energie & Umwelt / Energy & Environment

Band / Volume 642

ISBN 978-3-95806-779-0





Forschungszentrum Jülich GmbH  
Institut für Energie- und Klimaforschung (IEK)  
Elektrochemische Verfahrenstechnik (IEK-14)

# **Development of Iridium-based Nanostructures for Oxygen Evolution Reaction in PEM Water Electrolysis**

Seongeun Park

Schriften des Forschungszentrums Jülich  
Reihe Energie & Umwelt / Energy & Environment

Band / Volume 642

---

ISSN 1866-1793

ISBN 978-3-95806-779-0

Bibliografische Information der Deutschen Nationalbibliothek.  
Die Deutsche Nationalbibliothek verzeichnet diese Publikation in der  
Deutschen Nationalbibliografie; detaillierte Bibliografische Daten  
sind im Internet über <http://dnb.d-nb.de> abrufbar.

Herausgeber  
und Vertrieb:           Forschungszentrum Jülich GmbH  
                                  Zentralbibliothek, Verlag  
                                  52425 Jülich  
                                  Tel.: +49 2461 61-5368  
                                  Fax: +49 2461 61-6103  
                                  zb-publikation@fz-juelich.de  
                                  www.fz-juelich.de/zb

Umschlaggestaltung:   Grafische Medien, Forschungszentrum Jülich GmbH

Druck:                    Grafische Medien, Forschungszentrum Jülich GmbH

Copyright:              Forschungszentrum Jülich 2024

Schriften des Forschungszentrums Jülich  
Reihe Energie & Umwelt / Energy & Environment, Band / Volume 642

D 82 (Diss. RWTH Aachen University, 2024)

ISSN 1866-1793  
ISBN 978-3-95806-779-0

Vollständig frei verfügbar über das Publikationsportal des Forschungszentrums Jülich (JuSER)  
unter [www.fz-juelich.de/zb/openaccess](http://www.fz-juelich.de/zb/openaccess).



This is an Open Access publication distributed under the terms of the [Creative Commons Attribution License 4.0](https://creativecommons.org/licenses/by/4.0/), which permits unrestricted use, distribution, and reproduction in any medium, provided the original work is properly cited.

## Abstract

Hydrogen is an important energy carrier in the coming future for sustainable energy systems. In particular, "green hydrogen" produced by water electrolysis is considered as an ultimate technology as it can greatly contribute to net-zero CO<sub>2</sub> emission. Accordingly, many green hydrogen targets and policies are being set around the world. The EU has announced plans to install 40 GW of green hydrogen electrolysis capacity in Europe by 2030, and Germany plans to produce up to 14 TWh of green hydrogen by 2030.<sup>1,2</sup>

Polymer electrolyte membrane (PEM) water electrolysis is the most promising system in the field of water electrolyzers because it offers advantages such as a wide operating range, high current density, and compact system design. It is expected to contribute to the production of green hydrogen, but unfortunately, the cost still needs to be reduced tremendously. Electrocatalysts are the most important part to focus on as they are based on platinum group metals (PGMs) and have the potential to reduce the high cost. In particular, iridium, the electrocatalyst for the anode side, is one of the scarcest elements, and its price is continuously increasing with significant fluctuations due to demand and limited production, which may be a bottleneck for large-scale application of PEM water electrolyzers.

In this work, the electrocatalysts for oxygen evolution reactions for PEM water electrolysis were explored. Novel nanostructures were synthesized and evaluated as electrocatalysts under acidic conditions. Since iridium is the only element that has reasonable electrocatalytic activity and stability, they are based on iridium as the main element and the research is focused on the better utilization of iridium in electrocatalysts from the structure point of view. The approach was followed by using transition metals to develop the catalyst structure, considering realistic conditions such as material cost. The electrocatalysts were analyzed and studied before and after electrochemical measurements.

## Kurzfassung

Wasserstoff ist ein wichtiger Energieträger für nachhaltige Energiesysteme der Zukunft. Insbesondere gilt "grüner Wasserstoff", der durch Wasserelektrolyse auf Basis von elektrischem Strom aus erneuerbaren Energien hergestellt wird, als vielversprechender Ansatz verfolgt, da er zu Netto-Null-CO<sub>2</sub>-Emissionen beitragen kann. Dementsprechend wurden jüngst auf der ganzen Welt zahlreiche Ziele und Maßnahmen für grünen Wasserstoff beschlossen. Die Europäische Union hat angekündigt, bis 2030 in Europa 40 GW an Elektrolysekapazitäten zu installieren, und die Bundesrepublik Deutschland plant, im Jahr 2030 bis zu 14 TWh grünen Wasserstoff zu produzieren.

Die Wasserelektrolyse mittels Polymerelektrolytmembran (PEM) ist die vielversprechendste Elektrolysetechnologie, da sie Vorteile wie einen großen Betriebsbereich, eine hohe Stromdichte und ein kompaktes Systemdesign vereint. Es wird erwartet, dass sie einen großen Beitrag zur Produktion von grünem Wasserstoff leisten wird, jedoch müssen die Kosten noch stark gesenkt werden. Die Elektrokatalysatoren sind dabei der wichtigste Ansatzpunkt, da in der PEM-Elektrolyse teure Platingruppenmetalle (PGMs) benötigt werden. Insbesondere Iridium, der häufigste Elektrokatalysator für die Anodenseite, ist eines der seltensten Elemente in der Erdkruste, dessen Preis aufgrund hoher Nachfrage und begrenzter Produktion kontinuierlich ansteigt, was einen Engpass für die großtechnische Anwendung von PEM-Wasserelektrolyseuren darstellen kann.

In dieser Arbeit wurden Elektrokatalysatoren für Sauerstoffentwicklungsreaktionen für die PEM-Wasserelektrolyse erforscht. Es wurden neuartige Nanostrukturen synthetisiert und als Elektrokatalysatoren unter sauren Bedingungen bewertet. Da Iridium das einzige Element ist, das eine angemessene elektrokatalytische Aktivität und Stabilität aufweist, basieren sie auf Iridium als Hauptelement. Die Untersuchungen konzentrieren sich auf die bessere Nutzung von Iridium in Elektrokatalysatoren aus struktureller Sicht. Als Ansatz wurde dazu die Verwendung von Übergangsmetallen zur Entwicklung der Katalysatorstruktur verfolgt, wobei realistische Bedingungen wie die Materialkosten berücksichtigt wurden. Die Elektrokatalysatoren wurden vor und nach elektrochemischen Messungen analysiert und untersucht.

## List of Abbreviation

### # -----

3D Three-dimensional

### B -----

BET Brunauer–Emmett–Teller

BSE Back-scattered electrons

### C -----

CA Chronoamperometry

CCUS Carbon capture, use and storage

CV Cyclic voltammetry

### D -----

DFT Density functional theory

### E -----

ECSA Electrochemically active surface area

EDX Energy-dispersive X-ray

EG Ethylene glycol

ESS Energy storage system

### F -----

FCC Face-centered cubic

FFT Fast Fourier transformation

### G -----

GCE Glassy carbon electrode

GRR Galvanic replacement reaction

### H -----

HAADF High-angle annular dark-field

HCP Hexagonal close-packed

HER Hydrogen evolution reaction

HFR High Frequency Resistance

### I -----

ICP-MS Inductively coupled plasma mass spectrometry

### L -----



LSV	Linear sweep voltammetry
<b>M</b> -----	
MEA	Membrane electrode assembly
<b>O</b> -----	
OER	Oxygen evolution reaction
ORR	Oxygen reduction reaction
<b>P</b> -----	
PEIS	Potentiostatic electrochemical impedance spectroscopy
PEM	Proton exchange membrane
PTL	Porous transport layer
PVP	Polyvinylpyrrolidone
<b>R</b> -----	
RDE	Rotating disk electrode
RHE	Reversible hydrogen electrode
<b>S</b> -----	
SE	Secondary electrons
SEM	Scanning electron microscopy
STEM	Scanning transmission electron microscopy
STP	Standard temperature and pressure condition (0 °C, 1 bar)
<b>T</b> -----	
TEM	Transmission electron microscopy
<b>X</b> -----	
XAS	X-ray absorption spectroscopy
XPS	X-ray photoelectron spectroscopy
XRD	X-ray diffractions

# Contents

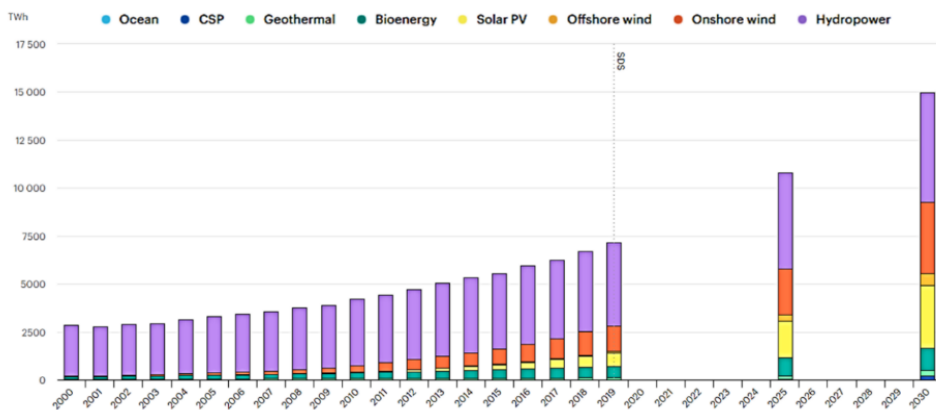
<b>1. Introduction .....</b>	<b>3</b>
1.1. Electrochemical water splitting .....	3
1.2. Proton exchange membrane (PEM) water electrolysis.....	7
1.3. Oxygen evolution reaction (OER) mechanism in acidic condition .....	10
1.4. Materials as electrocatalysts for OER in PEM water electrolysis.....	15
1.5. Approaches for the development of electrocatalysts .....	21
1.5.1. Hollow nanostructures .....	23
1.5.2. Alloying with transition metals .....	32
1.5.3. Facet control.....	36
1.6. Research goal .....	40
<b>2. Experimental procedures .....</b>	<b>42</b>
2.1. Material characterizations.....	42
2.1.1. Scanning electron microscopy (SEM) .....	42
2.1.2. Transmission electron microscopy (TEM) .....	44
2.1.3. X-ray diffractions (XRD) .....	46
2.1.4. X-ray photoelectron spectroscopy (XPS) .....	48
2.1.5. Inductively coupled plasma mass spectrometry (ICP-MS) .....	49
2.2. Electrochemical measurements .....	50
2.2.1. Three-electrode system.....	50
2.2.2. Single cell testing .....	52
<b>3. Results and discussion .....</b>	<b>55</b>
3.1. Bimetallic NiIr hollow nanoframes <sup>146</sup> .....	58
3.1.1. Synthesis of bimetallic NiIr hollow nanoframes .....	58
3.1.2. Structure characterization.....	58

3.1.3. Electrochemical measurements .....	67
3.1.4. Summary.....	72
3.2. Highly uniform IrO <sub>2</sub> nanospheres <sup>158</sup> .....	73
3.2.1. Synthesis of highly uniform IrO <sub>2</sub> nanospheres.....	73
3.2.2. Structure characterization.....	73
3.2.3. Electrochemical measurements .....	83
3.2.4. Summary.....	88
3.3. Ir-Ni hollow aerogel <sup>187</sup> .....	90
3.3.1. Synthesis of Ir-Ni hollow aerogel.....	90
3.3.2. Structure characterization.....	90
3.3.3. Electrochemical measurements .....	98
3.3.4. Summary.....	108
<b>4. Conclusions.....</b>	<b>109</b>
<b>5. References.....</b>	<b>112</b>
<b>List of Figures .....</b>	<b>130</b>
<b>List of Tables.....</b>	<b>135</b>

# 1. Introduction

## 1.1. Electrochemical water splitting

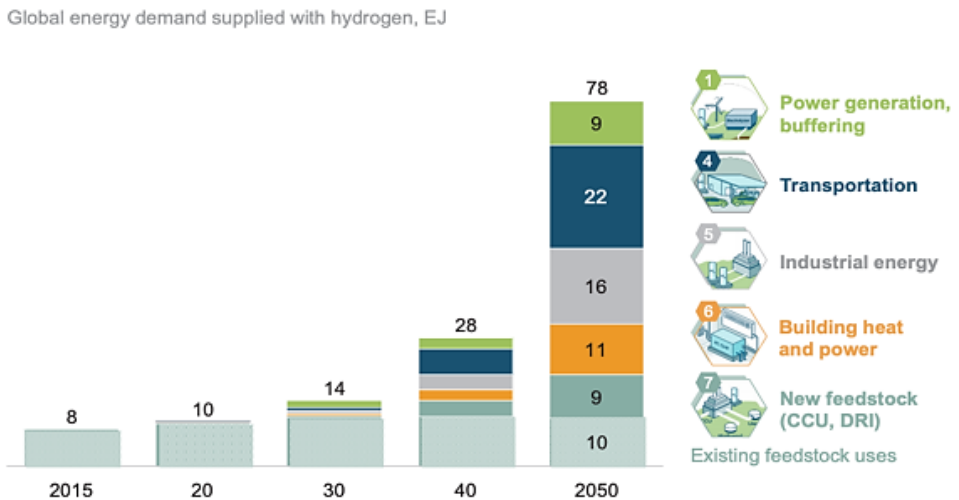
As concerns about environmental pollution and global warming continue, a lot of policies and strategies have been developed around the whole world to decrease the usage of coal fuels and convert the consumption into renewable energy.<sup>3,4</sup> Renewable energy is considered the ultimate solution for the upcoming future due to its sustainability and environmentally friendly property. As for solar energy and wind energy, the demand for renewable energy has grown, and the investment for the technology and infrastructure is also highly supported.<sup>5</sup> According to the International Energy Agency (IEA)'s release, the global electricity generation from renewable power sources was almost 27.0 % in 2019, which was the highest record so far.<sup>6</sup> However, more effort is pursued to reach the target for 2030 that is planned to cover more than half of power generation.



**Figure 1.** Renewable power generation by technology in the Sustainable Development Scenario, 2000-2030.<sup>6</sup>

**Figure 1** shows the developed renewable energy by technology since 2000.<sup>6</sup> As

shown in the figure, the renewable energy except hydropower takes up less than half of total generation so far, and it is considered that their restricted condition for energy production is one of the reasons for the sluggish development. The renewable energy collected from natural sources such as wind or sunlight is highly dependent on the region and weather.<sup>7,8</sup> Therefore, it should accompany a storage system to store the generated energy eventually, for the time the energy can be used later.<sup>9,10</sup> Up to now, the energy storage system (ESS) is mostly used to store the generated electricity, but it is heavy and carries the natural energy loss. From this point of view, hydrogen that can be stored and transported with convenience is a perfect energy carrier, which has an important role to boost the renewable energy markets.<sup>11</sup>

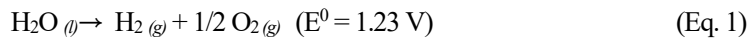


**Figure 2.** The potential demand for hydrogen by 2050.<sup>12</sup>

Hydrogen is a very attractive energy source. When it is used as fuel, it reacts with oxygen and can generate only water and heat without CO<sub>2</sub> emission, which is the reason why it is in the spotlight to reduce CO<sub>2</sub> emission. Furthermore, it has an excellent energy density (142 kJ·g<sup>-1</sup>) on a weight basis that is superior to oil (46 kJ·g<sup>-1</sup>) or natural gas (47 kJ·g<sup>-1</sup>), which makes hydrogen more attractive as a fuel.<sup>13</sup> It has

a huge potential to decarbonize by substituting major fields that demand a lot of energy as well as emit air pollutants including CO<sub>2</sub>, such as transport, power generation, and more.<sup>14,15</sup> Hydrogen Council reported that hydrogen energy will take about 18 % of the whole energy consumption by 2050, and it enables to decrease the emission of CO<sub>2</sub> by 6 billion tons per year.<sup>12</sup> **Figure 2** shows the global energy demand that will be supplied by hydrogen by 2050, and it is expected that more than 3.7 billion of oil will be substituted to hydrogen energy in 2050.<sup>12</sup>

Nowadays, hydrogen is divided into several categories that differ in energy source, method of production, and so on. Hydrogen can be produced mainly in four ways: 1) brown hydrogen obtained from the gasification of coal. This method is associated with the highest emission of greenhouse gases (19 tCO<sub>2</sub>/tH<sub>2</sub>),<sup>16</sup> 2) grey hydrogen produced by steam reforming of natural gas and water gas shifting. It is also associated with CO<sub>2</sub> emissions to the atmosphere (11 tCO<sub>2</sub>/tH<sub>2</sub>),<sup>16</sup> 3) blue hydrogen, in which CO<sub>2</sub> is captured and stored through carbon capture, utilization and storage (CCUS) in the production of brown or grey hydrogen, 4) green hydrogen, in which water is split into hydrogen and oxygen through electrolysis, which is free of CO<sub>2</sub> emissions. Unfortunately, about 95 % of the hydrogen produced in the world is still based on fossil fuels called brown and grey hydrogen, which makes the efforts to reduce CO<sub>2</sub> emissions meaningless. Research and development of 'green hydrogen' are therefore urgent. Electrochemical water splitting uses electricity to decompose water molecules into oxygen and hydrogen, and the reaction proceeds as follows under standard temperature and pressure (STP) conditions.



When the electricity from renewable energy can be used here, then there will be no CO<sub>2</sub> emitted in the hydrogen production process. This is evaluated as the most important synergetic technology to decarbonize the upcoming future, and many strategies are being planned for this worldwide. The European Union (EU) announced three steps project until 2050 to achieve carbon neutrality. They planned to displace the 'grey hydrogen' to 'green hydrogen' gradually. In particular, Germany published a

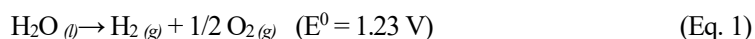
plan to construct the infrastructure for the production of 10 GW green hydrogen by 2040.

For water splitting, there are three main technologies mostly mentioned: alkaline water electrolysis, proton exchange membrane (PEM) water electrolysis, and solid oxide water electrolysis. Alkaline water electrolysis is a system that has been developed for the longest time with mature technology, so it is already commercialized. It uses non-platinum group metals as electrocatalysts such as nickel and cobalt, which makes it competitive in price. It also has a longer lifespan than other systems, which is approximately 10 years for a stack, but the current density is relatively low (0.2 – 0.6 A·cm<sup>-2</sup>) and operating conditions such as load range (20 – 40 %) or pressure (< 30 bar) are very limited due to the gas impurity.<sup>17–20</sup> Solid oxide water electrolysis operates at a very high temperature around 700 – 1,000 °C, which is useful in the environment requiring limited working conditions such as nuclear or geothermal power plants. Moreover, its efficiency reaches almost 100 % and when the heat from hot steam during operation can be considered for free/for granted, the efficiency is often calculated to be over 100 %. However, the high operating temperature causes a degradation issue including coarsening of electrodes and delamination from the electrolyte, which needs to be addressed.<sup>21,22</sup> Unfortunately, it is still at the research and development level. PEM water electrolysis will be discussed in the next chapter in detail.

## 1.2. Proton exchange membrane (PEM) water electrolysis

PEM water electrolysis is compared with alkaline water electrolysis which has been researched and developed for a long time, resulting in its fundamental technology being very well established. The alkaline water electrolysis requires lower cost than PEM water electrolysis because it does not require precious metal electrocatalysts by utilizing transition metals such as nickel and iron. However, it also has some disadvantages: lower current density (0.2 – 0.6 A·cm<sup>-2</sup>), low partial load range (20 – 40 %), a crossover of gases, etc.<sup>17,19,20</sup> In contrast, PEM water electrolysis has a higher current density (1.0 – 2.0 A·cm<sup>-2</sup>) and a wide partial load range (< 10 %).<sup>20,23,24</sup> Moreover, it can not only operate in quick system response, but also be compact in design. Due to the low gas crossover, high purity (99.99 %) of hydrogen is also achievable.<sup>20,23,24</sup> However, it has some challenging points such as low durability, which is 2 – 4 years of lifespan<sup>17,20</sup> and high cost for noble electrocatalysts, for example, iridium (4,150 USD/oz) and platinum (965 USD/oz).<sup>25</sup> It is because of the corrosive working environment that should operate under the high electrode potentials over 1.4 V in acidic conditions (pH 0 – 3) at the same time. Nevertheless, PEM water electrolysis is still preferentially studied and researched in the world because it has a great potential for development.

Regardless of the systems, in the splitting of water, the water molecules are split into hydrogen and oxygen by the application of electricity, and the entire reaction is expressed as follows.



At equilibrium, the minimum required energy for water splitting can be expressed as the Gibbs free energy under STP,  $\Delta G^0$  and calculated as (Eq. 2).

$$\Delta G^0 = nFE^0 = 2 \cdot 96485 \text{ C}\cdot\text{mol}^{-1} \cdot 1.23 \text{ V} = 237 \text{ kJ}\cdot\text{mol}^{-1} \quad (\text{Eq. 2})$$

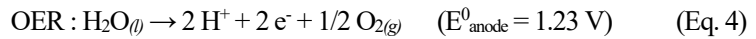
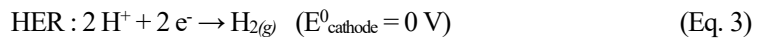


where  $n$  = number of involved electrons in the reaction

$F$  = Faraday's constant (96485 C·mol<sup>-1</sup>)

$E^0$  = Reversible voltage

This reaction is a combination of hydrogen evolution reaction (HER) and oxygen evolution reaction (OER) that occur separately on the cathode and anode, which can be different depending on the systems. For PEM water electrolysis using the acidic electrolyte, each reaction can be stated as follows.



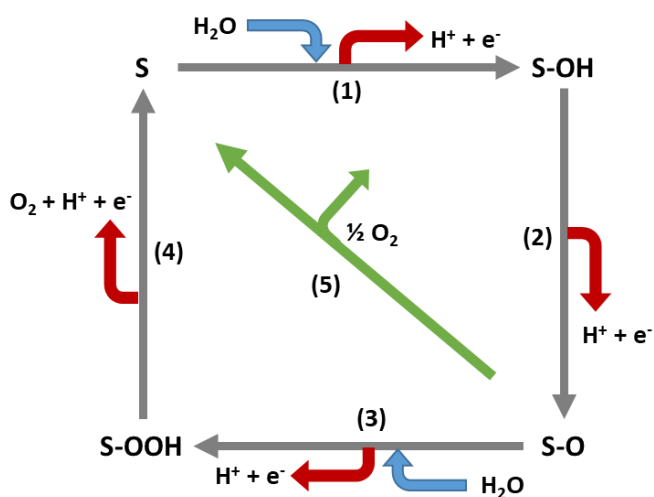
As shown above, in the case of HER on the cathode side two-electron transfer is involved. Since the initial state and the final state after reaction are equivalent at equilibrium, it allows the Gibbs free energy of the intermediates as the frequently mentioned descriptor for HER activity.<sup>26,27</sup> The Gibbs free energy will be presented as  $\Delta G_{\text{H}^*}$  where  $*$  denotes active site on the catalyst surface and  $\text{H}^*$  indicates adsorbed hydrogen atom on the catalyst surface. When platinum catalysts which are the most active for HER are used, the activation energy can be close to zero ( $\sim 0.09$  eV).<sup>28,29</sup>

On the contrary, the generation of oxygen on the anode side requires more additional energy to occur compared with HER, due to the complex and sluggish reaction kinetics that four electrons should be transferred per oxygen molecule. At least four elementary steps are required, and the activation energy is higher than in the one-electron transfer reaction. Besides, although the exactly needed potential (1.23 V) is applied it is difficult to observe the water splitting in reality due to the various kinetic barriers for the reaction. Therefore, for the generation of hydrogen and oxygen by water electrolysis in real, the potential higher than 1.23 V should be applied, and the additional potential is called 'overpotential'. Overpotential is divided and described in many ways but not strictly defined. The various kinds of overpotentials can be grouped into three in general: activation overpotential, ohmic overpotential,

concentration overpotential, which are observed in polarization curves in order. The ohmic overpotential and the concentration overpotential shown at higher current densities originate from the materials' resistance in the cell and insufficient supply. However, the activation overpotential seen at the beginning of the reaction relates to the rate of charge transfer, which is mainly due to intrinsic activation barriers at the electrodes. The overpotential can be reduced with the use of electrocatalyst, which is directly connected to the voltage efficiency of a cell. Accordingly, the development of electrocatalysts lowering the overpotential is highly important in the cost reduction of the electrolyzer, which accelerates the development of 'green hydrogen'.

### 1.3. Oxygen evolution reaction (OER) mechanism in acidic condition

OER Mechanism has been studied for a long time. Nevertheless, to this day no theory clearly explains the entire reaction process, since many intermediates are involved in the reaction and their reaction times are too short to interpret. It is also insisted that the mechanism can be varied because the electrocatalysts depend on the elements, compositions, facets, etc.<sup>30-32</sup> As the research results have been collected, several main hypotheses explain the OER mechanism in acidic media. Here, the most convincing theories that have gained acceptance are described as follows, and 'S' in the figure represents the active catalytic surface of electrocatalysts.



**Figure 3.** OER mechanisms for acidic conditions (S: the active catalytic surface).

The first model was proposed by Bockris in 1956, which is called as ‘the electrochemical oxide path’.<sup>33</sup> It consists of the steps (1), (2), and (5) as follows.





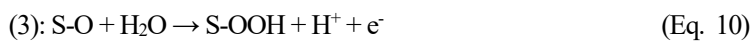
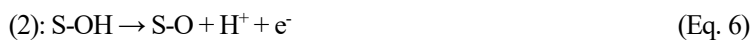
This hypothesis insists on a possibility that the  $\frac{1}{2} \text{O}_2$  can be directly released from the S-O. In this case, two S-O species should be combined and complete  $\text{O}_2$  with the regeneration of S sites, which requires a large activation barrier. In this study, Bockris also revealed that Tafel slope can indicate the rate-determining step in a certain mechanism. Tafel slopes are usually analyzed to understand the kinetics of the reaction and derived from the logarithmic OER polarization curves of the half-cell reaction. It describes how much the electric current can depend on the potential. Since it is under the assumption that the concentrations at the electrode and in the electrolyte are the same, it can be expressed as a function of the potential. For  $\text{RuO}_2$  as electrocatalyst, the analyzed Tafel slopes fit to the electrochemical oxide path well but with additional rearrangement steps. According to the mechanism, the Tafel slopes for each step are  $120 \text{ mV} \cdot \text{dec}^{-1}$  for step (1),  $40 \text{ mV} \cdot \text{dec}^{-1}$  for step (2), and  $15 \text{ mV} \cdot \text{dec}^{-1}$  for step (5). At higher potential over 1.52 V, the rate-determining step was found to be step (1). On the contrary, below 1.52 V, a Tafel slope of  $60 \text{ mV} \cdot \text{dec}^{-1}$  was obtained as the rate-determining step. To explain the difference of experimentally obtained Tafel slope values, substitutional detailed steps for the step (1) were proposed as below.



The substituted steps describe the intermediate ( $\text{S-OH}^*$ ) which is chemically the same as S-OH but energetically different. It indicates an additional rearrangement before it is oxidized further, and step (1-2) is the rate-determining step here. Castelli also revealed a similar OER mechanism using  $\text{RuO}_2$  (110) single crystals in relation to Tafel slopes in 1986.<sup>34</sup> At low potential below 1.52 V, the Tafel slope of  $\text{RuO}_2$  (110) single crystals was presented around  $60 \text{ mV} \cdot \text{dec}^{-1}$ , while polycrystalline samples recorded

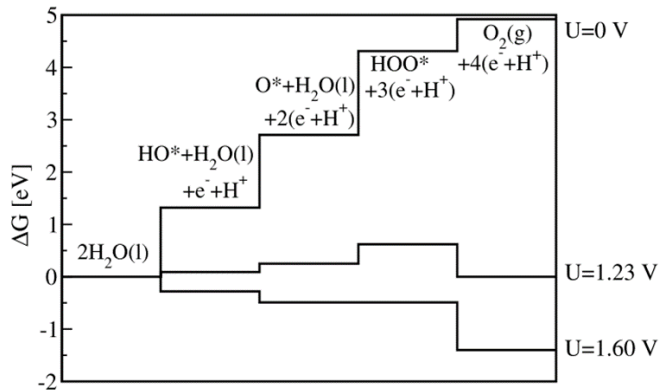
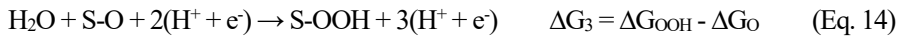
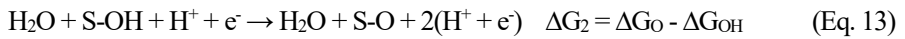
40 mV·dec<sup>-1</sup>. To account for this, it was proposed that the single crystals are subjected to the rearrangement prior to further oxidation, which may be related to the different energetic state on the (110) face with polycrystalline surface. Accordingly, the rate-determining step here will be step (1-2) and the step (1-1) will be at equilibrium. At high potential over 1.52 V, the RuO<sub>2</sub> (110) single crystals presented a Tafel slope of 120 mV·dec<sup>-1</sup>, which explained that the rate-determining step was changed from step (1-2) to step (1-1). The 40 mV·dec<sup>-1</sup> of Tafel slope for polycrystalline samples indicates that the reaction proceeds step (1), (2), and (5), and the rate-determining step here is step (2) when the step (1) is at equilibrium. As shown, the Tafel slopes can show different values, which allows a hypothesis about the OER mechanism and the rate-determining steps. The differences can occur from the layer properties that electrocatalysts have such as composition, crystallinity, and more. However, a determination of rate-determining step by only Tafel slope can be risky, since it can also indicate similar values depending on the material properties regardless of different rate-determining steps and different mechanisms. Accordingly, it should be referred to as one of the results to understand the reaction.

The second model is based on the density functional theory (DFT) calculations for metal oxides electrocatalysts from the perspective of thermochemical analysis, reported in 2007 by Rossmeisl et al.<sup>35</sup> The mechanism is based on the peroxide reaction intermediates, described as the grey rectangular in **Figure 3**.



It was proposed as the mechanism first and supported by the calculation of Gibbs free energy for each step in the reaction.<sup>35</sup> The mechanism displays each elementary

reaction whenever one electron is transferred. Each step can have different Gibbs free energy that is calculated as a function of the electrode potential, and the step having the largest value will be possibly the potential determining step. Accordingly, the entire reaction can be rewritten with the description of the Gibbs free energies as below. The Gibbs free energy for the steps are determined by the adsorption energy of the intermediates, that is, the catalyst.



**Figure 4.** The depiction about Gibbs free energies of the intermediates on O<sup>-\*</sup>-covered RuO<sub>2</sub> at three different potentials (U=0, U= 1.23, and U= 1.60 V).<sup>35</sup>

As an example, RuO<sub>2</sub> (110) was adopted and analyzed in the study. Ideally, each

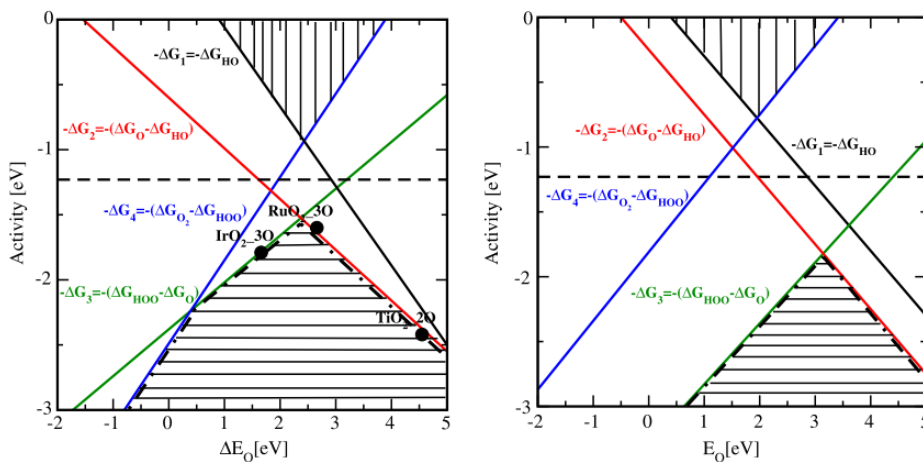
elementary reaction should require 1.23 eV of potential, but in real system using RuO<sub>2</sub> (110) as the electrocatalyst, each Gibbs free energy was calculated under an applied potential U as follows:  $\Delta G_1 = 1.32 \text{ eV} - eU$ ,  $\Delta G_2 = 1.39 \text{ eV} - eU$ ,  $\Delta G_3 = 1.60 \text{ eV} - eU$ ,  $\Delta G_4 = 0.65 \text{ eV} - eU$ . It means that the third step will be the potential determining step in this reaction since it requires the largest potential and at least 1.60 eV of potential should be provided to make the reaction occur. **Figure 4** describes visually the Gibbs free energies of the intermediates for OER on RuO<sub>2</sub> (110) surface. At the 1.23 V of equilibrium potential, the reaction steps are uphill, on the contrary, when 1.60 V of potential is applied, all the reaction steps are downhill in free energy, meaning that it becomes thermodynamically feasible.





principle.<sup>38</sup> The volcano plot presents the activity for oxygen evolution in conjunction with the enthalpy for the formation of a higher oxidation state for electrocatalysts. According to his explanation, oxides that are oxidized with difficulty cannot be very active because the intermediates adsorb too weakly. Conversely, oxides that are oxidized with ease may also not be very active because the intermediates adsorb too strongly. This implies that balanced adsorption for intermediates is essential in the catalytic reaction. Various metal oxides were studied, which resulted in the volcano shaped-curve showing that RuO<sub>2</sub> and IrO<sub>2</sub> located on the top of the volcano plot closest the most.

The volcano plot became a great tool to predict the electrocatalytic activity for materials. It was remarked via DFT-computational studies by Rossmeisl et al. in 2007 as **Figure 6**.<sup>35</sup> The study is based on the OER mechanism that includes four consecutive single electron transfer reactions and explains them by using oxygen chemisorption energies for intermediates.



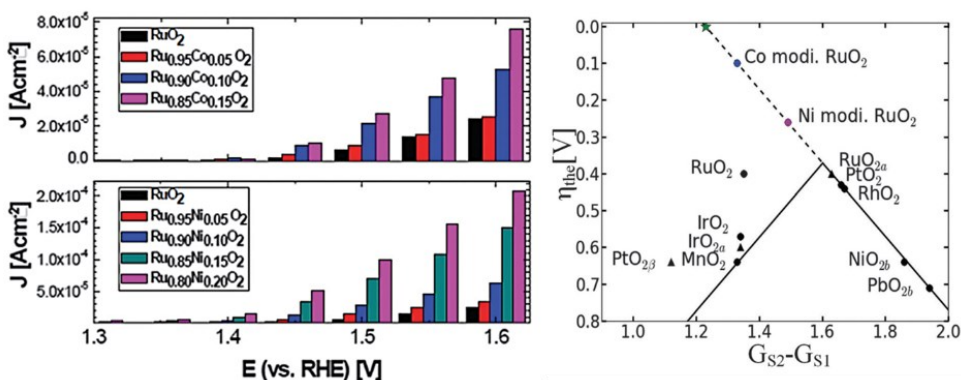
**Figure 6.** The theoretical activity of the four charge transferring steps of oxygen evolution depicted as function of the oxygen binding energy for (left) oxide surfaces and (right) metal surfaces.<sup>35</sup>

**Figure 6** shows the electrocatalytic activity as a function of oxygen binding energy. Each line shows the Gibbs free energy for each step in the OER mechanism, and the activity has been plotted as a negative value of Gibbs free energy. The dashed lines and the shaded areas describe the resulting volcano. In the case of the oxides (**Figure 6**, left), the interaction with water is small, and for the metal surfaces (**Figure 6**, right), the interaction with water has been taken into account, which results in the stabilized -OH and -OOH by comparison with -O. Since the equilibrium potential of 1.23 eV is expressed as the horizontal dashed line, the most optimized catalyst materials should be close to the line. As the strength of oxygen binding on the surface, too weak or too strong oxygen binding area was cut off, which is outside of the red (S-O formation) and green (S-OOH formation) lines. Based on the peak of under volcano (~2.3 eV), RuO<sub>2</sub> showed a slightly weaker oxygen binding energy and IrO<sub>2</sub> showed a slightly stronger oxygen binding energy, resulting in the activity of RuO<sub>2</sub> being higher than that of IrO<sub>2</sub>, and it was supported by other studies.<sup>39-41</sup> For instance, Shan et al. reported that RuO<sub>2</sub> nanoparticles showed 2.5 times higher mass-normalized electrocatalytic activity with 109.3 A·g<sup>-1</sup> than 43.6 A·g<sup>-1</sup> for IrO<sub>2</sub> nanoparticles at 330 mV of overpotential in 0.05 M H<sub>2</sub>SO<sub>4</sub> electrolyte.<sup>39</sup> In the study that compared rutile IrO<sub>2</sub> and RuO<sub>2</sub> nanoparticles by Lee et al., it was also reported that RuO<sub>2</sub> recorded 11 A·g<sup>-1</sup> when IrO<sub>2</sub> showed 3 A·g<sup>-1</sup> of catalytic activity at 0.25 V of overpotential in 0.1 M HClO<sub>4</sub> electrolyte.<sup>40</sup>

In the case of metal surfaces (**Figure 6**, right), the best achievable metal catalysts are around 3.2 eV, indicating that the required overpotential is higher than that for the best metal oxide catalyst surface. It is explained that the surface of purified metals has a very strong oxygen binding energy additionally required. However, it has been already reported that OER occurs on metal surfaces only when they are sufficiently covered with oxygen, and in reality, metal surfaces usually meet this condition, following the same trends with oxides.<sup>42</sup>

As the research to figure out the OER mechanism has been accumulated and the reaction descriptors have been reported, the materials for electrocatalysts no longer need to be limited in the volcano plot. Since the OER depends on the relationship

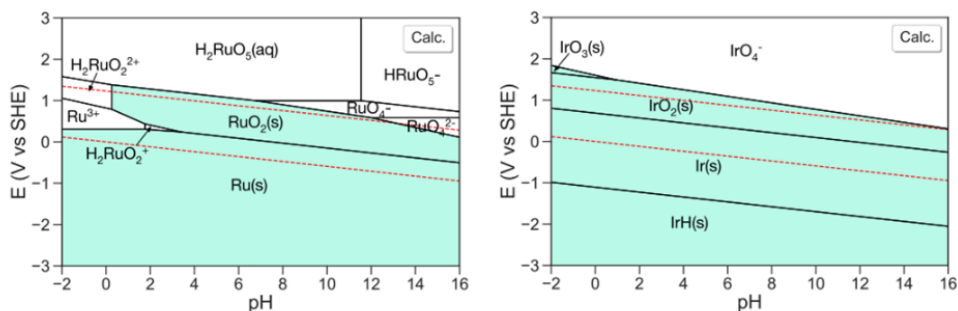
between the adsorption energies of the reaction intermediates and the reactivity of the catalyst surface, the catalytic activity can be improved by modifying the active sites. Halck et al. reported the catalytic activity beyond the existed volcano plots with the Co / Ni modified RuO<sub>2</sub> (**Figure 7**).<sup>30</sup> To overcome the limitation, nickel or cobalt was incorporated into the RuO<sub>2</sub> surface by co-precipitation with ruthenium during synthesis, which achieved a proton donor–acceptor functionality on the bridge surface sites of RuO<sub>2</sub> that were conventionally inactive. It may be confined that the catalytic activity occurs on the coordination unsaturated sites on the catalyst surface; however, with the modification by the introduced cation such as cobalt or nickel, the active sites can be formed with the unsaturated oxygen bonds by the surface metal cations, called as activated 'bridge' sites. They explained that these activated bridge sites can adsorb hydrogen from 'S-OH' and 'S-OOH' easier (S stands for the active catalytic surface), which leads to the decreased overpotentials of bare RuO<sub>2</sub>. The Co / Ni modified RuO<sub>2</sub> showed around 10-fold improved performance compared to bare RuO<sub>2</sub>.



**Figure 7.** The current density for OER on Co / Ni modified RuO<sub>2</sub> (left) and volcano curve of the theoretical overpotential for OER based on the DFT calculations (right).<sup>30</sup>

For the catalyst for OER in acidic conditions, not only the activity but also the stability of electrocatalysts must be considered because of its corrosive working

environment as mentioned earlier. That is the reason why  $\text{IrO}_2$  is evaluated as the state-of-the-art catalyst for OER in PEM water electrolysis. Even though  $\text{RuO}_2$  presents the highest catalytic activity,  $\text{RuO}_2$  has been reported frequently regarding its vulnerable durability by dissolving in the acidic electrolyte during the reaction.<sup>40,43,44</sup> On the contrary, iridium presents superior stability in the working condition for PEM water electrolysis, which is supported by the iridium Pourbaix diagram (Figure 8) and other previous research.<sup>43,45,46</sup> Cherevko et al. performed a comparative study for OER and HER using  $\text{RuO}_2$ , Ru,  $\text{IrO}_2$ , and Ir thin film electrodes.<sup>45</sup> Under the conditions that the morphologies of electrodes and other experimental parameters were identically provided, it was found that the dissolution was increased as the order of  $\text{IrO}_2 \ll \text{RuO}_2 < \text{Ir} \ll \text{Ru}$  during OER regardless of electrolytes, which indicated that iridium is more stable than ruthenium and oxidized surface is more resistant than metal surface to the dissolution.



**Figure 8.** Calculated Pourbaix diagram for ruthenium (left) and iridium (right).<sup>46</sup>

Unfortunately, iridium, which is one of the rarest elements on earth, has limited annual production. According to the USGS minerals yearbook, the global iridium annual production from 2014 to 2018 was noticed as 5.2 – 7.7 tons.<sup>47,48</sup> Under the assumption that 25 % of the produced iridium can be used for PEM water electrolysis and the state-of-the-art technology is applied at  $3 \text{ W}\cdot\text{cm}^{-2}$  and  $2 \text{ mg}_{\text{Ir}}\cdot\text{cm}^{-2}$ , approximately 2.6 –

3.5 GW can be produced in the year of 7 tons production.<sup>49,50</sup> Considering that a target of 40 GW electrolysis capacity for renewable hydrogen by 2030 in Europe, the circumstance urges to utilize iridium more efficiently. Catalyst development is one of the crucial keys to reduce the iridium usage but achieve the target. Bernt et al. explained the effects of well-structured catalyst material to the reduction of iridium, performed within the Kopernikus P2X project.<sup>51</sup> In the study, 'High-structured' catalyst with a  $0.3 \text{ mg}_{\text{Ir}} \cdot \text{cm}^{-2}$  loading was introduced, which showed the same performance with commercial  $\text{IrO}_2/\text{TiO}_2$  from Umicore at a  $2.5 \text{ mg}_{\text{Ir}} \cdot \text{cm}^{-2}$  loading. The evaluation was performed in  $5 \text{ cm}^2$  single cells at  $80 \text{ }^\circ\text{C}$  using  $50 \text{ }\mu\text{m}$  Nafion 212 membranes and  $0.3 \text{ mg}_{\text{Pt}} \cdot \text{cm}^{-2}$  loading of cathodes. Both electrocatalysts showed  $3.4 \text{ A} \cdot \text{cm}^{-2}$  of current density at  $1.79 \text{ V}$  corresponding to a cell voltage efficiency of  $70 \text{ \%}_{\text{LHV}}$ , which would be iridium-specific power densities of  $0.41 \text{ g}_{\text{Ir}} \cdot \text{kW}^{-1}$  for the commercial  $\text{IrO}_2/\text{TiO}_2$  ( $2.5 \text{ mg}_{\text{Ir}} \cdot \text{cm}^{-2}$ ) and  $0.05 \text{ g}_{\text{Ir}} \cdot \text{kW}^{-1}$  for the high-structured catalyst ( $0.3 \text{ mg}_{\text{Ir}} \cdot \text{cm}^{-2}$ ). It clearly indicates that even though the catalyst loading was decreased over 8 times, if the cell performance can be sustained, the iridium-specific power density goes down dramatically, which presents the importance of catalyst development well.

## 1.5. Approaches for the development of electrocatalysts

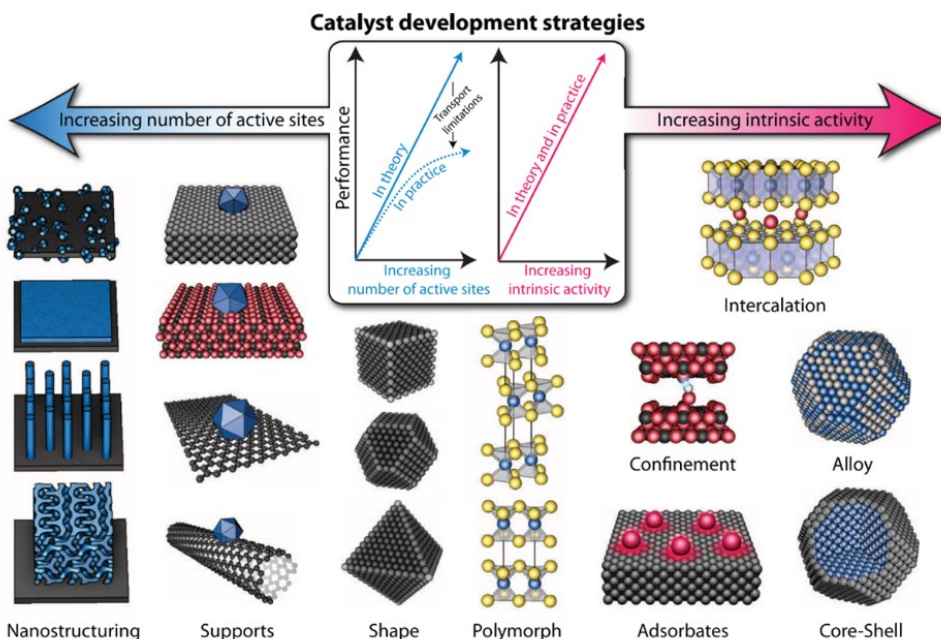
Catalytic activity can be improved mainly in two ways: increasing the number of active sites and increasing intrinsic catalytic activity. The two strategies are not absolutely separated and can be satisfied at the same time. The number of active sites can be simply increased by increasing the catalyst loading, but it has some limitations in the process such as fabrication of electrode, charge, and mass transport. Accordingly, it is usually achieved by modifying catalyst structure. Decreasing particle size of catalysts or fabrication of hierarchical structures is preferred since they are highly effective ways to expose more surface area.<sup>52,53</sup> Formation of open morphology has been also popularly reported such as hollow nanocubes or hollow nanoframes as it can utilize the surface inside of the structure as well.<sup>54-57</sup> Adopting conductive supporting materials can be also helpful, which induces that the catalytic particles can be dispersed onto them well and supported by boosted charge transfer.<sup>58-60</sup> In this case, care should be taken in the selection of supporting materials, as some materials such as carbon or carbide/nitride are easily oxidized under the working conditions and can damage the electrode eventually.<sup>61-63</sup>

Increasing intrinsic catalytic activity affects the catalytic performance more directly, as it can reduce the required catalyst loading for the same performance, which will be connected to the improvement of process and cost reduction overall. The intrinsic activity is strongly correlated to surface energy, which can be controlled by several factors: chemical composition that can be changed by doping or alloying, structural disorders that usually appear in hollow nanostructures, coordination of exposed surfaces or facets, and more.

In particular, for the development of electrocatalyst for OER in the PEM water electrolyzer, the stability of electrocatalysts is an eminently challenging issue. As mentioned previously, the working condition for anode side is highly acidic (pH 0 – 3) and high potential over 1.4 V is applied, so the materials are easily subject to irreversible oxidation or dissolution into the electrolytes during oxygen evolution. This severely limits the choice of materials for the electrocatalyst in noble metals such as ruthenium or iridium. Luckily, it has been reported that the stability can be also enhanced by some strategies introduced above. For instance, additional dopant in the

catalyst structure can prevent the declining stability by obstructing atomic rearrangement of catalysts and constructing a firm alloy phase.<sup>64</sup> It is highly demanding, but the stability of electrocatalysts must be considered for PEM water electrolysis with the improvement of catalytic activity.

Research and development of electrocatalysts have been carried out not only for water splitting, but also for other applications such as methanol oxidation, CO<sub>2</sub> electrolysis, photoelectrochemistry, and more.<sup>65–69</sup> In previous research, some main approaches are commonly used in the development of electrocatalysts. Here, some representative approaches are presented in the following chapters.



**Figure 9.** Schematic illustration of catalyst development strategies.<sup>70</sup>

### 1.5.1. Hollow nanostructures

Fabrication of hollow nanostructures can bring many merits in electrocatalytic reactions. Since catalytic reaction occurs only at the surface of the catalysts, it is essential to increase the frequency of catalytic events by exposing more surface of catalysts, and hollow nanostructures are more effective to expose their surfaces than solid structures.<sup>71-73</sup> Wang et al. prepared Pt icosahedral nanocages and evaluated the catalytic activity measured at 0.9 V for oxygen reduction reaction (ORR).<sup>74</sup> By comparison with commercial Pt/C ( $0.35 \text{ mA}\cdot\text{cm}^{-2}$ ), the Pt icosahedral nanocages showed  $3.5 \text{ mA}\cdot\text{cm}^{-2}$  of 10.0 times improved specific activity and almost 7 times increased mass activity of  $1.28 \text{ A}\cdot\text{mg}_{\text{Pt}}^{-1}$ . If there are even some holes on the surface of hollow nanostructures, that is, the walls are porous, then the reactant can access to the atoms on the inner surfaces, which boosts the catalytic reaction more. Zhang et al. explained that hollow and porous structures can produce catalytic activity on both inside and outside of catalyst structures by evaluating their platinum hollow nanocages. They revealed that around 20 % of the total surface area originated from small holes covering the nanocages and presented that the one-third of platinum usage could be saved with the structures to achieve the same performance.<sup>75</sup> It indicates that fabrication of hollow nanostructures is economical by minimizing the unused mass inside that cannot participate in the catalytic reaction, but also maximizing the efficiency of catalyst use. It was also reported that hollow structures can increase the possibility of reaction events by confining the reactants inside of the structures.<sup>76</sup>

Moreover, it enables to possess the structural disorders or defects that favors to the electrocatalytic reaction by inducing them during synthesis, which enhances the intrinsic catalytic activity.<sup>77-79</sup> The disorders or defects are usually produced when the core part is dissolved, which tunes the energy states of the active sites. For instance, it has been reported that the interface lattice mismatch originated from the core and shell generates the strain on the catalyst surface, which modulates the surface energy states.<sup>77,80</sup> Chattot et al. proved that microstrain in the structure can boost the electrocatalytic property by evaluating nanostructures with different densities of grain boundary.<sup>79</sup> In this study, the crystallite size and chemical composition of catalyst



particles were controlled similarly with 3 nm of crystallite size and PtNi stoichiometry of 85:15, but the degree of disorder was discriminated. Among the six kinds of nanostructures (solid, hollow, core-shell, etc.), 'sea sponge' like PtNi/C nanostructures having microstrain the most showed 9.3-fold boosted ORR specific activity compared to commercial Pt/C, and all of the evaluated nanostructures showed a trend to increased catalytic activity in proportion to the amount of microstrain.

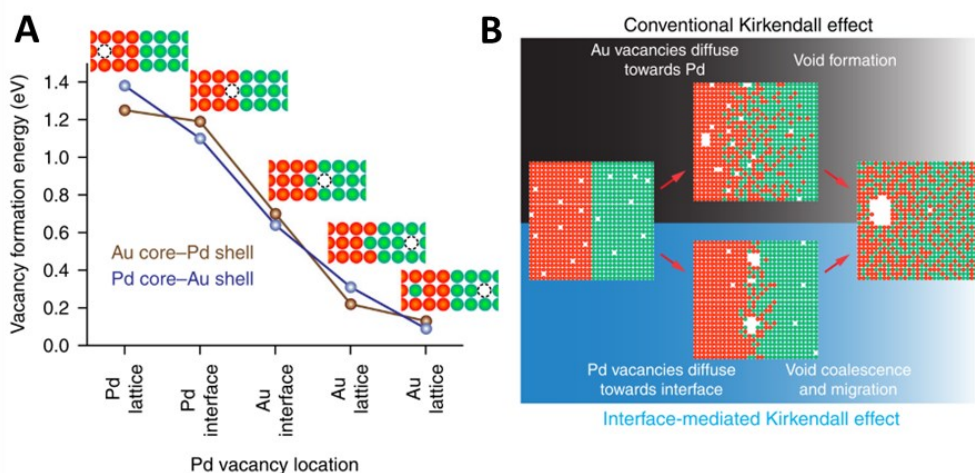
Various kinds of hollow nanostructures have been reported including nanoframes,<sup>56,57,76,81,82</sup> nanospheres,<sup>83</sup> nanocubes,<sup>55,84</sup> and so on.<sup>85-87</sup> For the fabrication of hollow structures templates should be set first. The templates can be prepared in advance or fabricated *in-situ* with the second materials that are desired for the structures. When pre-synthesized templates are used, the syntheses are much more efficiently controlled. Depending on the template structures, the morphology or facet of final structures can be diverse and simply modified. Moreover, the fabrication procedure can be divided into steps separately, which enables to manage each step with convenience. On the other hand, the adoption of an *in-situ* synthesized template demands a more elaborate plan for synthesis. The deposition of desired materials should be followed during or after the formation of the template directly, so the kinetics between materials participating in the synthesis are highly important. The well-constructed *in-situ* syntheses can save the costs for the production of materials in the end. When the structures are completely formed, the fabrication of hollow parts is induced. In the following contents, the frequently used methods to fabricate hollow structures are introduced with other literature.

- **Kirkendall effect**

The Kirkendall effect is an interfacial mediated motion between two types of metals caused by different diffusion rates. It occurs when two different materials are in close proximity and diffusion can occur between them. Since the diffusion coefficients of the two materials are usually different, diffusion is described by the vacancy mechanism described by Fick's 1st law. The flux of atoms from the material with the higher diffusion coefficient will be greater, bringing the net flux of atoms from the material with the higher diffusion coefficient into the material with the lower diffusion coefficient. Then,

a flow of vacancies is created in the opposite direction to create equilibrium in the flow of atoms, resulting in an overall movement of the lattice.

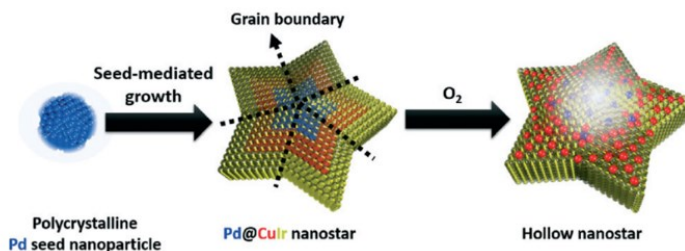
In a fabrication of hollow nanostructures, it occurs when the inner metal diffuses outward rapidly and the outer metal moves inward slowly. Due to the difference between their diffusion rates, voids form inside, which are called 'Kirkendall voids'. The final structures can be obtained as core-shell structures or as fully alloyed hollow structures, depending on the experimental conditions.



**Figure 10.** Formation energy of Pd vacancies and a schematic illustrating interface-mediated Kirkendall effect. (A) DFT calculations of the formation energy of a Pd vacancy at different locations of the Au-Pd layered structure. (B) A schematic comparison of the conventional Kirkendall effect and the observations of interfacial void formation and void migration in this study. (Green: Au atoms, Red: Pd atoms)<sup>88</sup>

Chee et al. explained the Kirkendall effect in relation to the effects of material properties by studying Au-Pd bimetallic nanoparticles during heat treatment with *in-situ* morphology characterization.<sup>88</sup> They observed the migration of voids at the

bimetallic interface with time and explained it by DFT calculation (**Figure 10**). It revealed that regardless which material is core or shell, the vacancy flux is directly towards the Au, and it is because that higher vacancy formation energy in Pd induces the vacancy flux heading to Au which diffuses slower. They also highlighted that the intermixing of Au and Pd, that is, the Au atoms diffused into the Pd lattice can boost the flow of vacancies with the further decreased vacancy formation energy, which induces the alloying of the two metals. As one of the fabrication methods for hollow nanostructures, it has been frequently reported that hollow nanostructures synthesized by the Kirkendall effect presented the improvement in catalytic activity.<sup>89–93</sup> Bang et al. reported a novel hollow Pd/CuIr nanostar structure with a formation of double layer assisted by Kirkendall effect.<sup>89</sup> It was initiated from the Pd@CuIr core-shell nanostar, which was attempted to dissolve the Cu component by oxidation (**Figure 11**). However, it rather induced the Pd coating on the inner surface and completed the double layer hollow nanostars, which is attributed to the boundary extension from Pd core to CuIr shell and outward diffusion of Cu along the boundaries. In the electrochemical measurements, the hollow Pd/CuIr nanostar showed approximately 5 times improved catalytic activity for OER compared with the Pd@CuIr core-shell nanostar.



**Figure 11.** Schematic illustration of the formation process for a hollow bilayer Pd/CuIr nanostar.<sup>89</sup>

- **Galvanic replacement reaction (GRR)**

The galvanic replacement reaction, a very powerful tool for fabricating hollow nanostructures, occurs via the difference in standard reduction potentials between two metal components.<sup>94,95</sup> In this reaction, one metal, which has a relatively low reduction potential, is sacrificed as template by oxidation and the other, which has a higher reduction potential, displaces the space. Accordingly, the choice for the pair of metals that will be participated in the reaction is important to succeed in the replacement reaction. The overall galvanic replacement reaction can be described as below when the standard reduction potential of material 'A' is lower than material 'B', and the energy for entire reaction is positive.



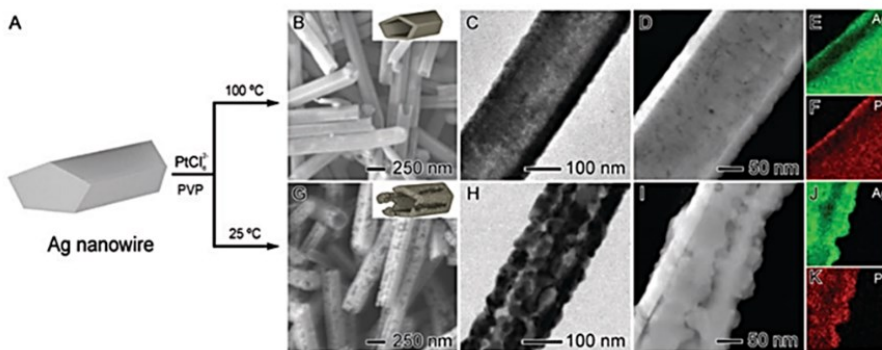
**Table 1.** Standard reduction potential for metals mostly used.<sup>96</sup>

Reduction reaction	E° (V vs. SHE)
$Mn^{2+} + 2e^- \rightarrow Mn$	-1.19
$Zn^{2+} + 2e^- \rightarrow Zn$	-0.76
$Fe^{2+} + 2e^- \rightarrow Fe$	-0.45
$Co^{2+} + 2e^- \rightarrow Co$	-0.28
$Ni^{2+} + 2e^- \rightarrow Ni$	-0.26
$Cu^{2+} + 2e^- \rightarrow Cu$	+0.34
$Ru^{2+} + 2e^- \rightarrow Ru$	+0.46
$Ag^+ + e^- \rightarrow Ag$	+0.80
$Pd^{2+} + 2e^- \rightarrow Pd$	+0.95
$Ir^{3+} + 3e^- \rightarrow Ir$	+1.16
$Pt^{2+} + 2e^- \rightarrow Pt$	+1.18
$Au^{3+} + 3e^- \rightarrow Au$	+1.50

**Table 1** shows the standard reduction potentials for the metals most commonly used for galvanic replacement reaction. As can be seen from the table, the transition metals located on the first row have relatively lower standard reduction potentials than noble metals that resist oxidation or corrosion, which made them popular as the pairing for galvanic replacement reaction.

Galvanic replacement reaction occurs especially better on the sites which have relatively high surface energies, for example, defects, disorders, or steps. Sun et al. observed the morphological change of Ag nanocubes in the galvanic replacement reaction with Au precursor as the reaction time.<sup>97</sup> In this reaction, the deposited Au atoms showed a tendency to grow epitaxially on the Ag nanocubes due to the small lattice mismatch of Au (4.086 Å) and Ag (4.078 Å). It started with a pit formation and continued to a partial cavity, which completed the porous and hollow Au nanocage.

The galvanic replacement reaction can also induce diverse morphologies of nanostructures by tuning one experimental condition. Rodrigues et al. achieved AgPt nanotubes with smooth or rough surfaces by only changing the temperature for the galvanic replacement reaction between Ag and  $\text{PtCl}_6^{2-}$ .<sup>98</sup>



**Figure 12.** Morphology observation of AgPt nanotubes with smooth (B-F) and rough surfaces (G-K).<sup>98</sup>

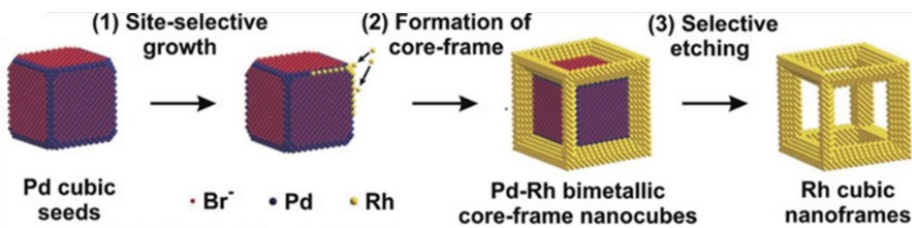
When the reaction proceeded at 100 °C, Pt was replaced with Ag as the same

morphology of the original Ag nanowire structure (**Figure 12**). However, when the reaction occurred at room temperature, the precipitation of AgCl crystals happened onto the surface of Ag nanowires, which induced a further Pt deposition on them. As a result, rough surfaces of AgPt nanotubes were achieved, which exposed more Pt surface atoms than the AgPt nanotubes with smooth surfaces. Which oxidation state of precursor is used for the replacement reaction in the beginning also affects the outcome, explained by the stoichiometric difference. Au et al. compared the galvanic replacement reaction with Ag nanocubes using two different oxidation states of Au precursors.<sup>99</sup> When  $\text{AuCl}_4^-$  was used in the reaction, three  $\text{Ag}^+$  ions should be used to reduce the one  $\text{Au}^{3+}$  ion, resulting in the Au nanocages having even some holes. On the contrary, in the case of using  $\text{AuCl}_2^-$  as Au precursor, each one  $\text{Ag}^+$  ion was enough to reduce one  $\text{Au}^+$  ion, which created Au nanoboxes having thicker walls than the wall of Au nanocages.

The galvanic replacement reaction can be an easy and simple means of improving electrocatalytic activity, as described many times in the literature.<sup>98,100–104</sup> Hong et al. achieved improved catalytic activities for ORR with synthesized Pd-Pt alloy hollow nanostructures.<sup>101</sup> The syntheses initiated from Pd octahedral and cubic nanocrystals as sacrificial templates, which produced various Pd-Pt hollow structures from octahedral nanocages with porous walls to dendritic hollow nanocrystals depending on the used amount of reductant. In the evaluation for ORR with 0.1 M  $\text{HClO}_4$  electrolyte, the octahedral nanocages exhibited 3.8 times enhanced mass activity ( $764.7 \text{ mA}\cdot\text{mg}^{-1}$ ) compared to Pt/C ( $200.5 \text{ mA}\cdot\text{mg}^{-1}$ ). It is ascribed by the higher surface area as well as the beneficial surface facet for ORR induced during the reaction, which will be discussed in the next chapter 'facet control'. Wang et al. synthesized polycrystalline Ni-Ir nanocages from Ni templates by galvanic replacement reaction.<sup>105</sup> The already prepared Ni templates were submerged into the iridium precursor solution for the galvanic replacement reaction, which completed the  $\text{Ni}_{2.53}\text{Ir}$  nanocages with concentrated iridium in the thin shell. The  $\text{Ni}_{2.53}\text{Ir}$  nanocages were evaluated as electrocatalysts for OER in acidic electrolyte and showed 302 mV of overpotential to reach a current density of  $10 \text{ mA}\cdot\text{cm}^{-2}$ , which is 2.1 times higher activity than commercial Ir-black.

## • Selective etching

Selective etching can be defined as the removal of specific facets in nanocrystals or less stable components to control the structure such as shape, size, and composition. It can use pre-synthesized materials as templates and remove the parts that need to be removed selectively via chemical or oxidative etching step, so the resulting structures are highly dependent on the original templates. Accordingly, it is a versatile method to define the desired morphologies or shapes with ease by controlling the templates, which is frequently used to design hollow nanostructures such as nanoframes, nanocages, nanotubes, etc.<sup>84,106–108</sup> However, the etching condition such as etching strength or rate should be previously confirmed to avoid any damage to the final structure, since the etching conditions are generally very harsh to remove the templates (e.g., 3 M HCl solution). Zhang et al. successfully fabricated the Pt nanocages possessing {100} and {111} facets that presented enhanced catalytic activity for ORR.<sup>75</sup> To achieve the structures, Pd nanocrystals with the defined facets were prepared first, followed by depositing the Pt atomic layer. The Pd nanocrystals were removed via selective etching using an aqueous solution containing FeCl<sub>3</sub> and HCl (pH 0.55) at 100 °C, which obtained the Pt nanocages with walls as thin as three atomic layers (0.7 nm thick) and their surfaces terminated in {100} or {111} facets that show the improvement in both of activity and durability for ORR in acidic electrolyte. The Rh hollow nanoframes reported by Xie et al. were achieved via oxidative etching using an etchant based on the Fe<sup>III</sup>/Br<sup>-</sup> coupling.<sup>109</sup> As the seed structures, Pd nanocubes were used, which were slightly truncated at corners and edges and possess {100} facet covered by Br<sup>-</sup>. Due to the Br<sup>-</sup> capped {100} facets, selective nucleation and growth of Rh occurred only on the corners and edges of Pd, which formed Pd-Rh bimetallic core–frame concave nanocubes. The Rh hollow nanoframes were obtained after the removal of the Pd core by selective etching conducted in an aqueous solution using the Fe<sup>III</sup>/Br<sup>-</sup> pair and HCl at 100 °C (**Figure 13**). The produced Rh hollow nanoframes achieved Rh {110} planes on the surface which is known as a great catalytic activity for Rh material.



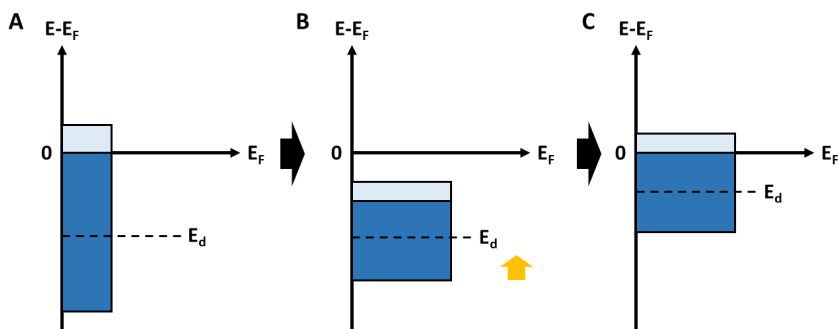
**Figure 13.** Schematic illustration of the fabrication procedure for Rh nanoframe.<sup>109,110</sup>



### 1.5.2. Alloying with transition metals

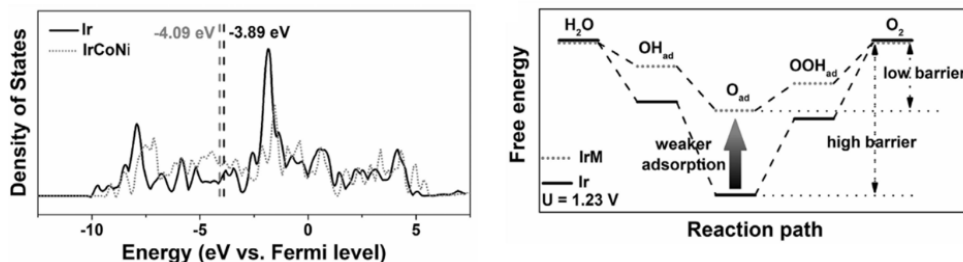
Alloying with transition metals is a very popular and common strategy to develop noble metal-based electrocatalysts.<sup>69,111–114</sup> Although the nanostructures alloyed between noble metals have been steadily reported, however, the 3d transition metals located on the first row (e.g., Mn, Fe, Co, Ni..) are used the most due to their advantages. The 3d transition metals are abundant and relatively cheaper, which is less burdensome in terms of price and production for long-term.<sup>115,116</sup> Moreover, they can play an important role as templates in the design of catalyst structures since they can be not only synthesized as diverse shapes with convenience but also eliminated easily.<sup>113,117</sup>

The biggest advantage of alloying with transition metals is 'd-band engineering'.<sup>54,118–121</sup> The d-band engineering is an optimization of binding energy by tuning the d-band structure, which can be related to the increase of intrinsic catalytic activity eventually. It approaches the balance between adsorption and desorption of adsorbates on the catalyst surface from the perspective of electronic structure. The binding energy is strongly related to the position of the d-band center, which can be altered by the interaction between different metal species. Explaining in detail, when the atoms are strained by tensile strength the d-band width shrinks, which makes the d-band center shifted upward to Fermi level to keep the d-band occupancy (**Figure 14**). This upshift of the d-band center contributes to the stronger adsorption for the reaction intermediates than before. Of course, the opposite movement of the d-band center can also occur when the atoms are under compressive strength. In that case, the d-band width can be broadened, followed by a downshift of the d-band center, which causes the weaker adsorption of adsorbates. Accordingly, it is important to determine the d-band center in the optimal position to boost the desired reaction.



**Figure 14.** The upshift of the d-band center when the atoms are applied by tensile strength.

As an example, Strasser et al. synthesized PtCu@Pt core-shell nanocrystals and proved the strain-dependency on the catalytic activity for ORR with them.<sup>122</sup> Since PtCu core had a smaller lattice than Pt, the Pt shell was applied by compressive strain, which induced the downshift of d-band center of the Pt surface. It weakened the adsorption energy of reaction intermediates, which led to the enhanced catalytic activity for ORR compared to unstrained conventional Pt. Feng et al. also reported how alloying with transition metals affected the d-band and catalytic activity in the end.<sup>83</sup> In this study, IrCoNi multimetallic porous hollow nanocrystals were synthesized, which showed 10 times improved catalytic activity for OER compared with commercial Ir/C. It was supported by DFT simulations showing that the d-band of IrCoNi models was shifted far away from Fermi level, which decreased the adsorption energy for intermediates (**Figure 15**). Consequently, it was proved that the alloyed Ir structures with 3d transition metals here can have the decreased activation energy for OER, supported by the 303 mV of overpotential to achieve 10 mA·cm<sup>-2</sup> which is around 10 times improved compared to the commercial Ir/C in the study.



**Figure 15.** (Left) Projected DOS of d-bands of Ir and IrCoNi models with corresponding d-band center as dash lines. (Right) Schematic illustration of reaction paths for OER.<sup>83</sup>


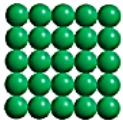

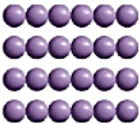

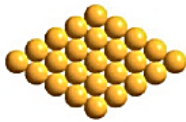
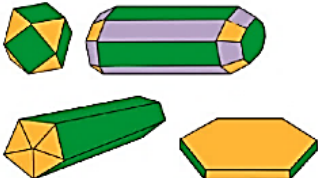
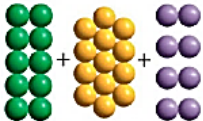
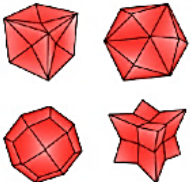
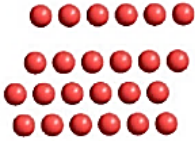
Alloying has been also reported as a strategy to improve the stability of electrocatalysts.<sup>64,123–126</sup> It is explained that the bimetallic or multimetallic composition modulates the thermodynamic stability of catalysts and enhances the compositional stability in the catalyst structures, which obstructs the dissolution or dealloying of catalysts and collapse of nanostructures.<sup>124,127–129</sup> To expect the improved stability, some points should be considered such as the optimal combination of elements, optimal compressive strain, and avoiding any phase segregation.<sup>77</sup> Wu et al. studied their ternary alloy PtPdCu catalysts as different compositions and obtained the optimized componential proportion showing the best mass activity and stability.<sup>129</sup> The study presents a strong correlation between the catalytic performance and the lattice constant, supported by the thermodynamically-stable Pt<sub>20</sub>Pd<sub>20</sub>Cu<sub>60</sub>/C catalyst showing the largest compressive strain of 4.1 % after 20,000 potential cycles, as well as high mass activity (1.66 A·mg<sub>Pt</sub><sup>-1</sup>) and high durability that shows no degradation even after 50,000 potential cycles. It was explained that the dealloying–realloying cycles functions as an effective self-healing process of the catalyst toward a thermodynamically stable alloyed material, which enhances the durability to the corrosion for both noble and base metals. The partial dissolution of base metals, Cu in this material (Pt<sub>20</sub>Pd<sub>20</sub>Cu<sub>60</sub>), into the electrolyte during the cycling in the beginning is followed by realloying of the remaining metals in the partially dealloyed nanoparticles. It is operated as a highly effective self-healing process toward a

thermodynamically stable alloy eventually.

### 1.5.3. Facet control

Facet control is a direct tool to increase the intrinsic electrocatalytic activity by inducing or exposing the desired facets for the reaction. Basically, most elements used as electrocatalysts (Ni, Cu, Ir, Pt, Pd, Ag, Au, Rh) have a face-centered cubic (FCC) structure, so the efforts for facet control are focused on FCC structure. For low-index facets of FCC structure, the specific surface free energies are ordered as  $\gamma(111) < \gamma(100) < \gamma(110)$ . As the (111) facets have a coordination number of 9, it was generally expected to have the highest stability among all facets, as well as the highly compacted atomic packing density, which can be a reason that the (111) atomic arrangements are intended in some research. Since ruthenium has a hexagonal close-packed (HCP) structure, different from other noble metals, it has been induced to have the FCC structure. Zhao et al. introduced a synthesis to achieve Ru cubic nanocages with a FCC structure, rather than the HCP structure that Ru normally has.<sup>108</sup> They prepared Pd cubic seeds as templates for FCC structure first and deposited Ru on the surface of Pd cubic, followed by the removal of Pd later. The successfully achieved FCC structure of Ru presented enhanced catalytic performance for ammonia synthesis by comparison with conventional ruthenium structure with HCP (0001).

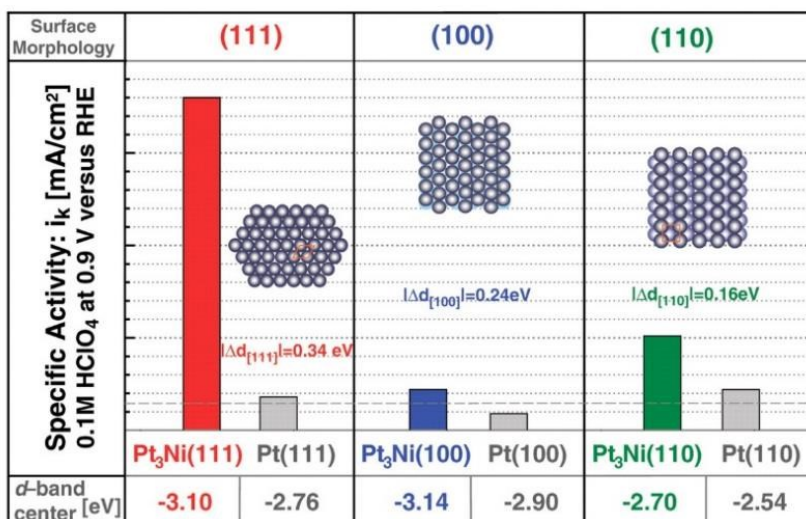
Looking further, the difference in surface energy for adsorption on each facet can be expanded. For instance, the facets in FCC structure can be classified into low-index facets including basal planes {100}, {110}, {111}, and high-index facets. **Figure 16** shows the illustration describing the exposed facets and atomic arrangements as the different shapes in the case of palladium. The low-index facets with high coordination numbers show relatively lower catalytic activity than high-index facets, and many studies attributed it to their lower surface energy. For this reason, research on high-index facets has a lot of attentions for the development of electrocatalysts nowadays.<sup>130–134</sup> High-index facets have a large number of terraces, steps, edges, kinks, and more potential defect sites with low coordination numbers on the surface, which can be attractive as electrocatalysts because of the high surface energy. For instance, Yu et al. reported that Pt concave nanocubes possessing high index facets such as {510}, {720} and {830} exhibited around 4-fold higher activity for ORR by comparison with Pt nanocubes with {100} facets.<sup>135</sup>

Nanocrystals with different shapes	Exposed facets	Atomic arrangements
	{100}	
	{110}	
	{111}	
	Mixed facets	
	High-index facets	

**Figure 16.** Reported polyhedral FCC shapes classified by their exposed facets, in case of palladium nanocrystals.<sup>106</sup>

However, facet control is a very sensitive technique that can bring entirely different results depending on the exposed surface properties for each catalyst material. The effects can be dramatically changed as the composition, structure, electrolyte, and so on. Stamenkovic et al. demonstrated that the well-defined (111) facet can be superior to the conventional (111) facet with Pt<sub>3</sub>Ni single crystals (**Figure 17**).<sup>136</sup> The Pt<sub>3</sub>Ni (111) surface possessed a tuned d-band center position and uncommon atomic

arrangements caused by the 50 at% Ni-rich composition of second atomic layer, which showed a 10-fold remarkably improved ORR activity compared to the Pt(111) and 90-fold to the conventional Pt/C. It noticed that the trend of activity as facets can be totally changed by modulation of composition and the followed surface property.



**Figure 17.** Influence of the surface morphology and electronic surface properties on the kinetics of ORR.<sup>136</sup>

The influence of electrolyte to the facet trends has been also reported.<sup>137–139</sup> Markovic and Ross compared the ORR activity with the typical low-index facets of Pt catalysts as different electrolytes.<sup>138</sup> When HClO<sub>4</sub> was used as electrolyte, the ORR activity showed a trend of Pt(110) > Pt(111) > Pt(100); however, in case of H<sub>2</sub>SO<sub>4</sub>, it was converted to Pt(110) > Pt(100) > Pt(111). They explained that this inconsistency is caused by the strong adsorption of SO<sub>4</sub><sup>2-</sup> on the Pt(111), which hindered the adsorption of reactants.

In conclusion, facet control is a highly sensitive method that requires delicate attention, since it is difficult to achieve the expected effects due to the many variables

affecting the results. Nonetheless, it is still a powerful and efficient tool to improve intrinsic catalytic activity of electrocatalysts when it is designed well and set up.



## 1.6. Research goal

The cost of PEM water electrolysis has been greatly reduced with many parts thanks to the technology that has progressed. However, the part of electrocatalysts for the anode side is stagnating, as a better catalyst than iridium has not been found. Iridium is the most preferred material in the working condition for PEM water electrolysis due to the durability that can be maintained as IrO<sub>2</sub> at pH 0 and below 1.55 V, which is the condition that RuO<sub>2</sub> is already dissolved. To get closer to the target 40 GW production of PEM water electrolysis by 2030 with the iridium available on a limited production, a significant reduction of iridium loading is required.<sup>51</sup> Unfortunately, the existing technology can hardly prevent the following reduction of power density.

The overarching goal of this research is to design, characterize, and evaluate novel nanostructures as electrocatalysts that present the improved electrocatalytic performance for OER in acidic conditions compared to the commercial iridium catalysts, with reduced iridium usage. To achieve this goal, several specific objectives could be set as below:

1. Fabricate the novel nanostructures using 3d transition metals. To use iridium efficiently, smart morphology of the structures is required to expose more iridium on the surface. Accordingly, the use of 3d transition metals should be considered in the design of synthesis not only to avoid the unnecessary use of iridium but also to obtain diversity and flexibility in the synthesis process and the final morphology of the structures. Every synthesis here utilized 3d transition metals as sacrificed templates or alloyed material with iridium. To confirm the efficient use of iridium in the novel nanostructures, the electrocatalytic activity is stated as iridium-specific mass activity by comparison with commercial iridium particles.
2. Explore the properties of iridium in syntheses. Iridium is a difficult material when it comes to designing or formulating a particular structure because it is the most corrosion-resistant metal. It may be the reason that iridium-based structures have been less reported than other platinum group metals such as platinum and palladium. Thus, it is important to understand the behavior of iridium in the development of novel nanostructures. For this, the synthesis

mechanism of each nanostructure was thoroughly investigated. In the given experimental conditions, it was observed how iridium was affected and how it was emerged in the structure (for example, it preferred to be deposited on the high surface energy area such as edges and vertices).

3. Apply the novel nanostructures to single cells. Many attractive nanostructures have been reported, but most of them end up in the electrochemical measurement using a three-electrode system that is convenient but difficult to implement the actual operating condition as it is, which can bring different testing results within a real single cell. In this research, the electrocatalytic performance of the designed nanostructures was evaluated in single cells, which enabled to observe the aspects of the electrocatalysts that are structured and alloyed with non-noble transition metals, in real cells. Furthermore, compared to the commercial iridium catalyst that is the state-of-the-art catalysts for OER, it was discussed whether the designed nanostructures are competitive and what should be considered and modified in the design of nanostructures to improve further.

The objectives were implemented with three different iridium-based nanostructures separately or in duplicate. Each nanostructure was designed using 3d transition metals, characterized, and evaluated in the following chapters.

## 2. Experimental procedures

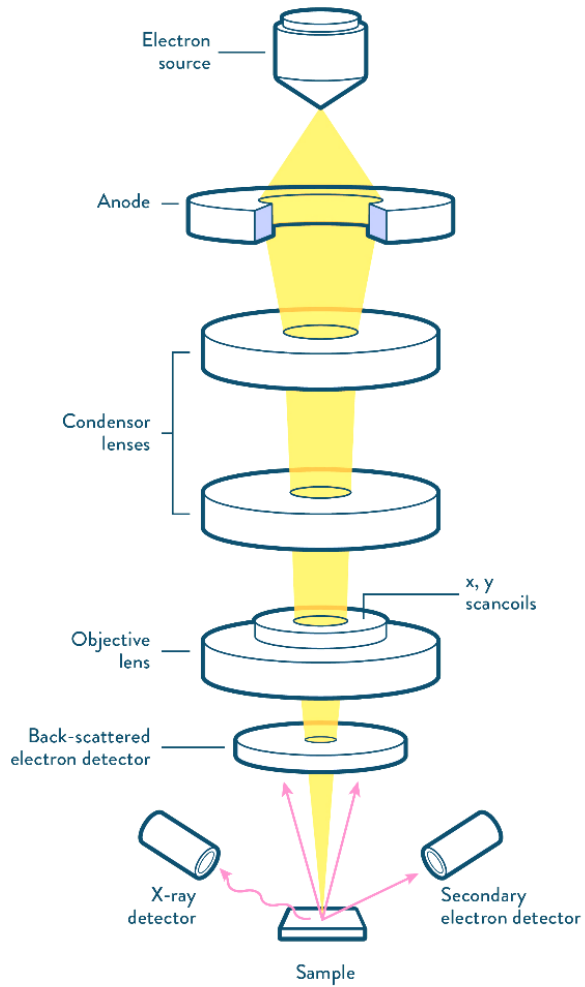
### 2.1. Material characterizations

#### 2.1.1. Scanning electron microscopy (SEM)

Scanning electron microscopy (SEM) is a powerful technique to analyze the morphology and the elemental distribution of a sample by scanning the surface with a focused beam of electrons (**Figure 18**). The electrons interact with atoms at various depths in the sample, which generate various types of signals such as secondary electrons (SE), back-scattered electrons (BSE), characteristic X-ray, and more. The SE signals are the electrons emitted from the top few nanometers of the surface of a sample, which creates the morphology of the sample by taking their intensities. The BSE signals are beam electrons reflected from the sample by elastic scattering. Since the intensity of BSE signals is strongly related with the atomic number ( $Z$ ) of the sample, it is used to obtain the distribution of different elements. If the element is heavier, it is displayed brighter than other elements in the sample, since the electrons deflect more strongly due to the bigger nuclei. Characteristic X-ray is emitted when the electron beam knocks off an electron from the inner shell of an atom. To fill the vacancy, another electron from an outer shell is attracted and moves, which releases the X-ray as much as the energy difference between the outer higher-energy and the inner lower-energy shell of the atom. As the energy of X-ray is distinctive to the specific element and transition, it enables to quantify the elemental composition in the sample by Energy-dispersive X-ray (EDX) spectroscopy.

For a sample preparation, the synthesized catalyst powder or catalyst coated electrode was dried thoroughly, since the moisture is detrimental to the equipment. The sample should be also electrically conductive, at least the surface. Accordingly, in case of metal oxide that has low electrical conductivity, the surface is coated with platinum or gold to increase the electrical conductivity. For the measurements here, the synthesized catalysts were coated by platinum sputtering for 30 seconds. Since the sample should be stabilized in the vacuum conditions and to the high energy beam of electrons, the sample is mounted on a specimen holder with a conductive adhesive. In this case, carbon tapes were used. The measurements were conducted on Hitachi

SU8000 at an accelerating voltage of 15 kV.



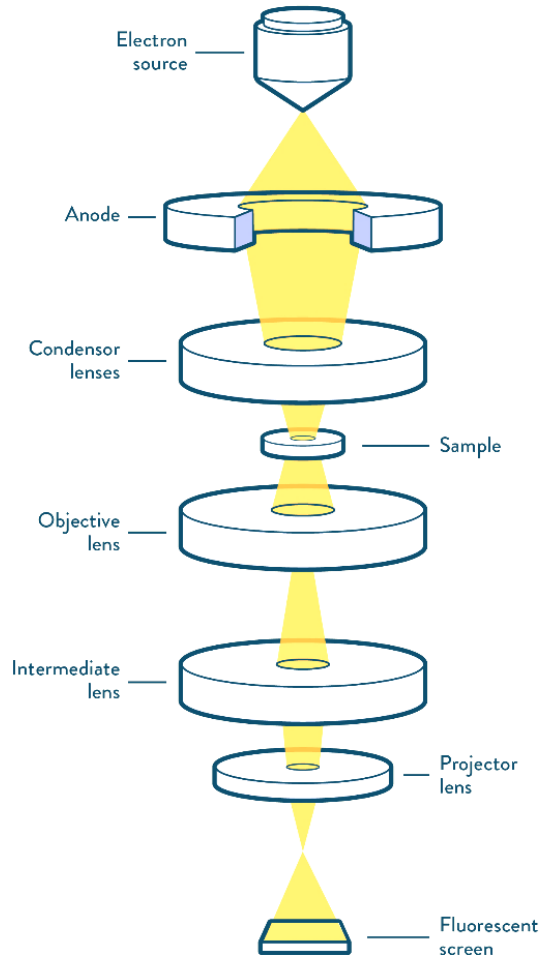
**Figure 18.** Schematic diagram of SEM<sup>140</sup>

### 2.1.2. Transmission electron microscopy (TEM)

Transmission electron microscopy (TEM) is a very useful tool in characterizing materials, especially for nanosized materials. It uses the transmitted electrons that pass through the sample. From the top of the microscope an electron source emits electrons that will go through a vacuum condition in the column of the microscope. The electrons are focused into a thin beam by the electromagnetic lenses (condenser lenses in **Figure 19**) and the beam passes through the sample. The objective lens placed after the sample blocks the high angle diffracted beam and increases the contrast of the image. By passing the projector lens, the magnification can be increased, and finally the image of the sample is recorded onto the fluorescent screen or a computer screen using a charge-coupled device (CCD) camera, which typically achieves 'bright field image'. Since it uses the transmitted electrons, TEM provides the information about inner structure of the sample such as morphology, stress state information, and crystal structure. It also enables to achieve optimal spatial resolution in better quality compared with SEM, which is 50 pm when SEM is limited to 0.5 nm. The functions of TEM can be extended with additional detectors or stages, and as one of the modified TEM scanning transmission electron microscopy (STEM) is commonly used. It is a combination of TEM and SEM, which possesses the advantages of both techniques that observe the inner structure as TEM, but also take the signals like X-rays that can be used in EDX spectroscopy investigations.

For a sample preparation, the electrocatalysts powders were suspended in isopropyl alcohol using a sonication bath until the suspension showed an even grayish color. The suspension was dropped onto a carbon coated copper TEM grid and dried at ambient conditions but avoiding any impurities. The dropping was repeated several times to spread enough amounts of particles on the grid.

In this study, STEM and EDX were conducted using an FEI (Thermo Fisher Scientific) Titan 80–200 electron microscope that utilized a probe corrector (CEOS) and a high-angle annular dark-field (HAADF) detector.<sup>141</sup> To achieve "Z-contrast" conditions, a probe semi-angle of 25 mrad was used with the detector having a 65 mrad inner collection angle. For the EDX elemental mapping, Ir L and Ni K peaks were used. TEM requires an ultrathin specimen less than 100 nm in general or a suspension on a grid, since the electrons in the beam interact with sample as mentioned above.



**Figure 19.** Schematic diagram of TEM<sup>140</sup>

### 2.1.3. X-ray diffractions (XRD)

X-ray diffractions (XRD) is a nondestructive technique to determine the crystal structure of a material. It enables to achieve the information on the sample such as crystallinity, crystal structure, phase, lattice parameters, orientation of a crystal or grain, and so on. The data can be produced by constructive and destructive interferences of monochromatic X-rays beam and a sample, which can be described by Bragg's Law as follows.

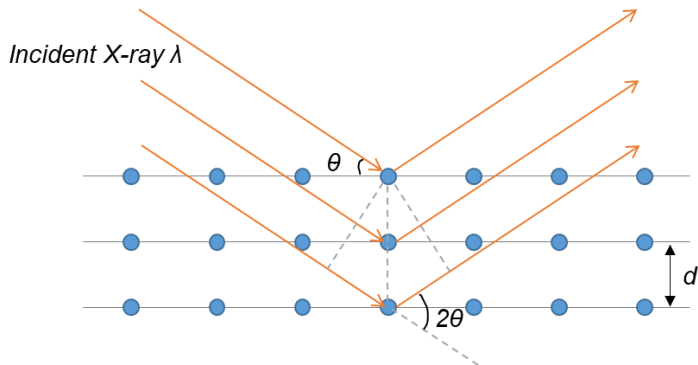
$$n \lambda = 2 d \sin\theta \quad (\text{Eq. 17})$$

where  $n$  = an integer called the order of reflection (1, 2, 3, ...)

$\lambda$  = the wavelength of the X-ray beam

$d$  = the spacing between diffracting planes

$\theta$  = the incident angle



**Figure 20.** Schematic diagram of the Bragg's law.

As shown in **Figure 20**, this law explains the relationship between the wavelength of monochromatic X-rays to the diffraction angle and the lattice spacing in a crystalline

sample. The diffracted X-rays are detected and collected. The sample is scanned through a range of  $2\theta$ , and in the case of powder samples, all possible diffraction directions of the lattice can be obtained due to the random orientation. Since each mineral has its d-spacings, the calculation of d-spacings from the diffraction peaks is useful to identify the material with the standard reference pattern data.

For a powder sample preparation, catalyst powder is ground by using a mortar and pestle to achieve fine particles. A certain amount of catalyst powders was stated and pressed on a silicon wafer to fully cover the spot and be compacted in 1 mm of height at least. The XRD measurements were performed in D8 DISCOVER (Bruker) using a Cu  $K\alpha$  source and LYNXEYE\_XE\_T as the detector. The range for measurements was set from  $10^\circ$  to  $120^\circ$  in a  $2\theta$  range with an increment of  $0.05^\circ$ . The peaks for silicon wafer that are already measured as the background are subtracted when the X-ray pattern is fitted.



#### 2.1.4. X-ray photoelectron spectroscopy (XPS)

X-ray photoelectron spectroscopy (XPS) is a technique for analyzing the surface of materials, which is a highly important tool in the research of catalysis. It determines the chemical and electronic states of elements on the sample surface, but also the elemental composition. When a monoenergetic X-ray beam is irradiated to the sample surface, the kinetic energy and electrons are ejected from the surface (from the top 1-10 nm in average), resulting in the XPS spectra. It is based on the photoelectric effect, which can be described as the following equation,

$$E_{\text{photon}} = E_{\text{binding}} + E_{\text{kinetic}} + \Phi \quad (\text{Eq. 18})$$

where  $E_{\text{photon}}$  is the energy of incident X-ray,  $E_{\text{binding}}$  is the binding energy of the electron of the element being measured,  $E_{\text{kinetic}}$  is the kinetic energy of the electron measured by instrument, and  $\Phi$  is a work function term. Since the  $\Phi$  is a proper correction factor that usually given as a constant by instrument,  $E_{\text{binding}}$  can be obtained by the equation. The binding energy depends on lots of factors, for example, the element measured, the orbital that the ejected electron was stated, and more. As each element has its unique set of XPS peaks at the binding energy positions, a subtle shift of XPS peak is related to a change of chemical or oxidation states.

Since the equipment is operated in the vacuum condition, the sample should be completely dried. In this study the XPS measurements were conducted in Phi5000 Versa Probell from ULVAC-Phi Inc. with Al K $\alpha$  as the monochromatic (1.486 keV) used as a source. The powder samples were pressed onto Indium foil to be sustained in the ultrahigh vacuum condition ( $<10^{-9}$  Torr) and fixed with clamps on a stainless-steel sample holder. The core-level spectra recorded with a pass energy of 23.5 eV, 0.1 eV energy step, and a spot size of 200  $\mu\text{m}$ . An electron flood gun and an Ar $^{+}$  ion gun were used for charge compensation. The spectra were charge corrected by setting the binding energy of the main C 1s component to 285 eV.

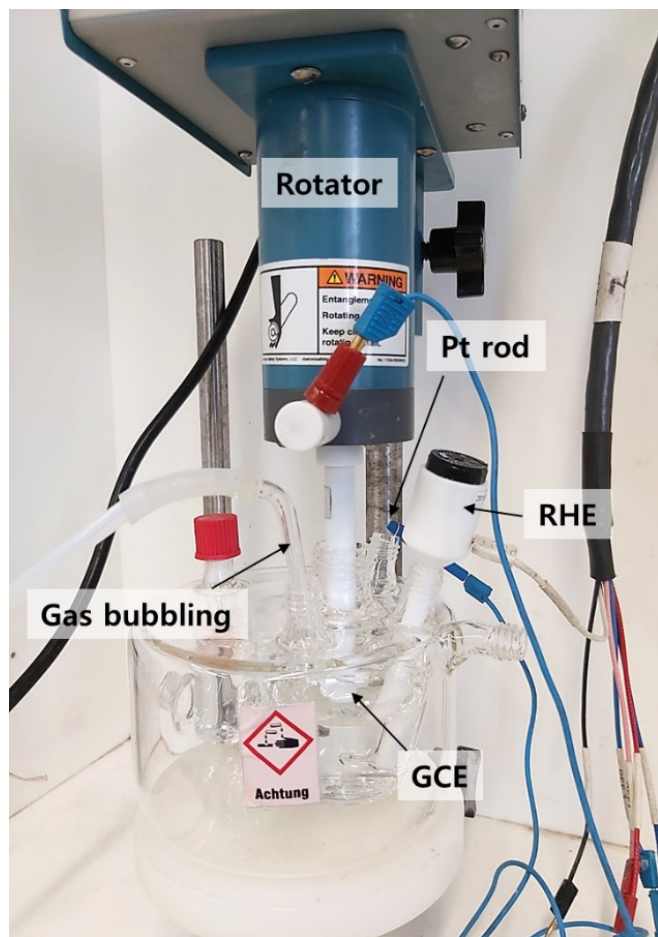
### 2.1.5. Inductively coupled plasma mass spectrometry (ICP-MS)

Inductively coupled plasma mass spectrometry (ICP-MS) is a mass spectroscopy to ionize the sample by using inductively coupled plasma. It detects dissolved metals in liquid samples at very low concentrations (parts per billion,  $\mu\text{g}\cdot\text{l}^{-1}$ ) and allows multiple elements to be measured simultaneously in a single analysis, which is one of its advantages. Moreover, it is used to determine isotopic ratios for the elements possessing more than one isotope. ICP-MS consists of six fundamental compartments: the sample introduction system, inductively coupled plasma (ICP), interface, ion optics, mass analyzer and detector.<sup>142,143</sup> From the sample introduction system, liquid samples are nebulized in a spray chamber and injected to the argon plasma in the form of a fine aerosol. The sample is atomized and ionized with the 6,000 – 8,000 K of high temperature plasma, which generates ions that were extracted into the ion optics through the interface region. The ion optics called as electrostatic lenses collects the ion beam and leads it to the quadrupole mass analyzer. The ions are separated in accordance with the mass-charge ratio by the mass analyzer and measured at the detector.

The ICP-MS was used to analyze the amount of each element in synthesized catalysts and to check the stability of materials with Agilent 7900 in this research. For a sample preparation, solid material should be destructed with nitric acid, or if necessary mixing with  $\text{H}_2\text{O}_2$ . The use of hydrochloric acid or sulfuric acid is not recommended, since hydrochloric acid can induce precipitates and the sulfur in sulfuric acid obstructs the analysis.<sup>143</sup> Moreover, the total dissolved solids content in samples should be kept below 0.2 % ( $=2\text{ g}\cdot\text{l}^{-1}$ ). In the case here, the catalyst powders were dissolved in 70 % nitric acid, with a  $1\text{ mg}\cdot\text{ml}^{-1}$  of concentration by sonication. When the catalyst powders are fully dissolved, the solution is diluted with deionized water (DI water) 100 times. Before the measurement, the sample was diluted 100-fold again and analyzed.

## 2.2. Electrochemical measurements

### 2.2.1. Three-electrode system



**Figure 21.** Three-electrode system for RDE measurements.

Three-electrode system uses a glass cell as shown in the figure above with a rotating disk electrode (RDE). A reversible hydrogen electrode (RHE) works as the reference electrode and a Pt mesh rod works as the counter electrode. As the working

electrode, a glassy carbon electrode (GCE) (diameter: 5 mm, area: 0.196 cm<sup>2</sup>) was used after the catalyst was coated onto it.

Before coating the catalyst, it should be sure that the surface of GCE is clean. The GCE can be typically polished with alumina suspension, and 0.05 μm of alumina was applied here. First, a few drops of the suspension are spread on the microcloth polishing pad, and the electrode is placed against the slurry. Next, the electrode is gently turned as a loop shape with a mild pressure. After polishing, the electrode is rinsed with DI water to remove the remaining alumina suspension on the surface. To make sure, the electrode was reversely ultra-sonicated with DI water here. These procedures should be performed before and after the usage of electrode for a well-maintained GCE.

The ink for catalyst coating was prepared by mixing 3.5 mg of catalysts with 0.7 mg of Vulcan X-72 as conductive material in DI water (7.6 ml), Isopropanol (2.4 ml), and 5 % of Nafion (40 μl). It was sonicated enough to achieve a homogeneous dispersion, and then 10 μl of the ink was dropped on the GCE, followed by drying naturally at ambient temperature, which results in the 17.8 μg·cm<sup>-2</sup> of catalyst loading. To reduce the variance of the results, it should be careful that the coated layer must cover the whole glassy carbon area uniformly but not the outside. The catalyst coated GCE is reversely fixed and held by the rotator. 0.5 M H<sub>2</sub>SO<sub>4</sub> was adopted as the acidic electrolyte and poured in the glass cell until all of the three electrodes can sink enough, and the cell was purged enough to form N<sub>2</sub> atmosphere before the measurements.

The electrochemical measurements were performed with a potentiostat (Biologic) at room temperature. Prior to measuring OER activity, the cyclic voltammetry (CV) was implemented for activation of the coated catalyst in the load range of 0.4 V to 1.4 V with a scan rate of 500 mV·s<sup>-1</sup>, followed by slower sweeping at a scan rate of 50 mV·s<sup>-1</sup> to determine the redox peaks. To evaluate OER activity, linear sweep voltammetry (LSV) was performed between 0.4 V to 1.7 V with a scan rate of 5 mV·s<sup>-1</sup> with O<sub>2</sub> saturated electrolyte. The LSV was performed again with the same condition if the durability test was implemented.

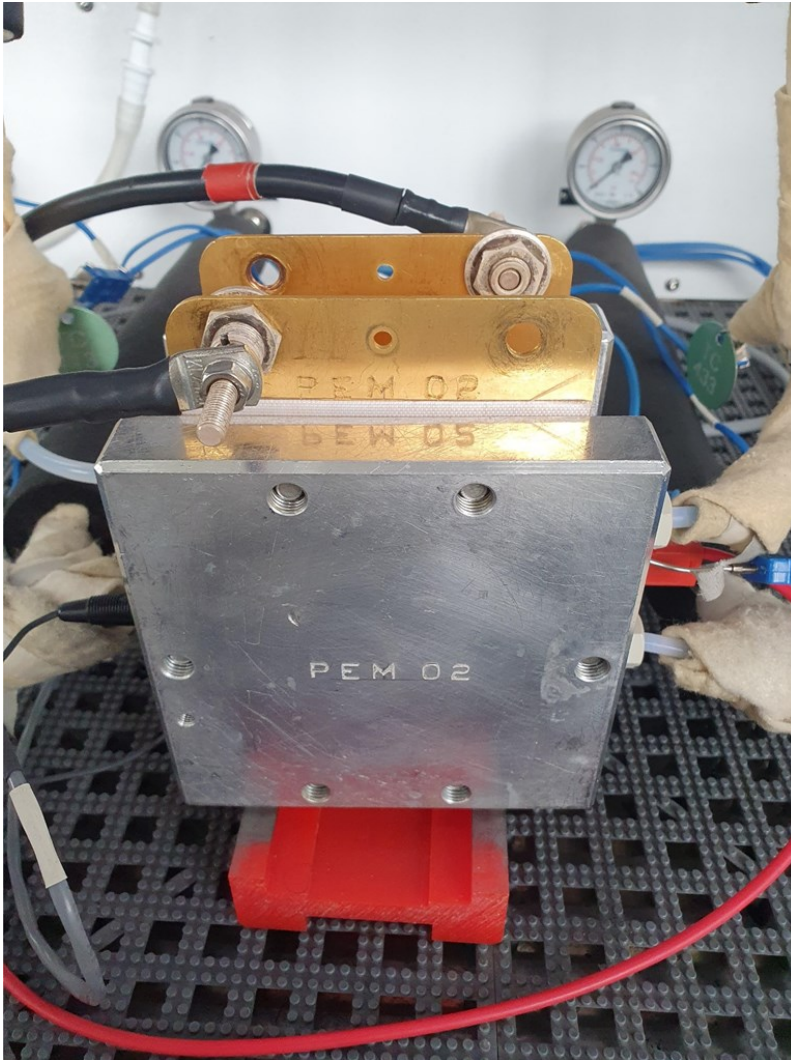
### 2.2.2. Single cell testing

The anodes were made using a spray-coating device (ExactaCoat, Sono-Tek). The stable dispersion for coating was prepared with enough sonication and stirring by mixing catalyst material, Nafion ionomer (Ion Power Inc.), DI water and n-propanol (Merck), which was sprayed on a decal sheet. All cathodes used here were made with a doctor-blade (Coatmaster 510, Erichsen GmbH & Co. KG). The ink for the cathode was prepared as a mixture of catalyst (60 % Pt/C, FC catalyst), Nafion ionomer, DI water and 2-butanol (Merck), dispersed by a dispersion device (Ultra-Turrax, IKA) and homogenizer (Sonopuls HD3400, Bandelin). The cathode loading was  $0.8 \text{ mg} \cdot \text{cm}^{-2}$ . The cathode possessed 20 wt% of Nafion content, while 11 wt% of Nafion was chosen for the anode. The coated catalyst layers ( $25 \text{ cm}^2$ ) were transferred onto the Nafion membrane (N117, Chemours) by hot-pressing at  $130 \text{ }^\circ\text{C}$  with applying a joining time of 3 min at  $1.6 \text{ kN} \cdot \text{cm}^{-2}$  of pressure. As porous transport layer (PTL) on the anode, both-sided iridium sputtered Titanium fiber mesh (Bekipor® ST Titanium Grade 1, Bekaert) was used. The thickness of the sputtered iridium layer was 20 nm, and its amount was  $0.05 \text{ mg}_{\text{Ir}} \cdot \text{cm}^{-2}$  per side.

For single cell testing, an ETS E100 electrolyzer test station (Greenlight Innovation) was used. The operation temperature was set to  $80 \text{ }^\circ\text{C}$  while water flow of  $50 \text{ mL} \cdot \text{min}^{-1}$  was maintained at atmospheric pressure. The first 2 hours in the beginning were used for preliminary conditioning and equilibration. Afterwards, the cell was operated for 30 min at a current density of  $0.2 \text{ mA} \cdot \text{cm}^{-2}$ , followed by an increased current density to  $1.0 \text{ mA} \cdot \text{cm}^{-2}$ , which was held for another 30 min. The last step for the activation was a continual operation step with 1.7 V of cell potential for 8 hours. For the performance test, potentiostatic testing was performed and each measurement point was held for 5 min until the maximum voltage of 2.0 V was reached. For each test, forward and backward scans were used.

The cell was disconnected from the test station and connected to a potentiostat (HCP1005 Biologic) for potentiostatic electrochemical impedance spectroscopy (PEIS) measurements. The sinus amplitude was set to 10 mV and a frequency range from 10 kHz to 100 mHz was chosen for each measurement. The basic measurement protocol was the same for all tests as below, except that the degradation test was performed either of them.

1. Activation
2. 10 times of polarization curves scanned forward and backward
3. High Frequency Resistance (HFR) analysis
4. 3 times of polarization curves scanned forward and backward
5. Degradation test: Cycling for certain times between 1.45 V and 2 V,  
or holding the potential at 2 V for 500 hours
6. 10 times of polarization curves scanned forward and backward
7. HFR analysis



**Figure 22.** Single cell after finishing the assembly.

### 3. Results and discussion

Here, three different electrocatalysts were designed and synthesized considering the approaches discussed previously. First, the materials were based on the iridium mainly, since iridium is still irreplaceable for OER in acidic condition in reality. Second, it was intended to achieve the structural advantages for catalysts as much as possible. Although the composition is the same, the physical and chemical properties of materials can be totally different depending on the nanostructure, which naturally affects the electrocatalytic performance. In this research, how each catalyst structure was acquired in the synthesis was studied in detail, with understanding the behavior of iridium in the synthesis, and the morphologies and properties of structures were characterized. In the design of the electrocatalyst structures, 3d transition metals were positively adopted, as the transition metals are effective to control the morphology in synthesis, as well as to expect the improvement in the activity and stability via alloying and doping effect. Considering their prices, for example nickel is over 6,000 times cheaper than iridium (Iridium: 4,000 USD/ozt, Nickel: 9.4 USD/lb), it is also economically beneficial to utilize them in a long-term aspect. The transition metals were used as initial templates for structures or alloyed elements here. The electrocatalytic performance of synthesized electrocatalysts were evaluated using a three-electrode system or fabricating single cells, and the changes in structures after testing were also observed.

Bimetallic NiIr hollow nanoframes were fabricated by wet chemical synthesis. Nanoframes are three-dimensional (3D) hollow structures consisting of very thin walls, so they can minimize the bulk inside area that cannot participate in the reaction, as well as utilize the atoms placed inside of the structures. However, nanoframes have a difficulty to withstand the structures during electrocatalytic reactions due to the thin wall thickness. The NiIr hollow nanoframes here were synthesized from the initial NiIr hexagonal nanostructures which have nickel core part and iridium on the vertices and edges. The nickel core part was selectively removed by etching solution, which successfully induced the well-alloyed NiIr hollow nanoframes by Kirkendall effect in the process. The NiIr hollow nanoframes showed highly improved electrocatalytic activity which is 29 times higher mass activity than commercial IrO<sub>2</sub> nanoparticles and



well-maintained morphology after 1,000 cycles of durability test, driven by the synergy effect from the frame structure, bimetallic composition, and more. However, it has a challenging point that the production beyond the lab-scale is difficult owing to the synthesis condition that should be delicately controlled, which will be the direction to be researched further.

Next, uniform IrO<sub>2</sub> nanospheres were synthesized by utilizing MnO<sub>2</sub> nanostructures as initial templates by cation exchange reaction. By adopting the already prepared template materials, the synthesis could be controlled more facile. Besides, the manganese was fully exchanged with iridium during the reaction, which completed the final nanostructures consisting of iridium solely. It avoided the potential resistance that can be caused by vulnerable manganese in acidic condition but acquired the uniform morphology of iridium nanostructures with the surface property favorable for OER. It was worthy to study the behavior of iridium nanostructures as electrocatalysts, since iridium catalysts have been usually reported in the literature as being supported by additional elements to form an alloy or decorate the surface, due to its difficulty in forming a specific structure. With the IrO<sub>2</sub> nanospheres, it was verified again that the structured and uniform morphology can enhance the electrocatalytic activity, supported by three-fold boosted iridium-specific mass activity for OER compared to commercial IrO<sub>2</sub>. Furthermore, it was revealed that the well-designed synthesis with utilizing transition metals can accomplish the preferable surface property for OER without any additional post-treatment such as etching or annealing procedure.

From the previous research, it was confirmed that the specific structures and the collaboration with transition metals can be beneficial to the improvement of electrocatalytic performance. The smart design of synthesis procedure was also highlighted. The third catalyst structure was designed considering them including the fabrication process as well. As competent and economical electrocatalysts, iridium has been reported in several ways, such as particle size reduction<sup>144</sup>, fabrication of hollow nanostructures<sup>56,82,83</sup>, assisting with supporting materials<sup>58,59,145</sup>, and more. Unfortunately, most of the ways reported often have some limitations to be applied at a large scale in reality due to limited yield of production, easy agglomeration during the electrode fabrication, loss of catalysts and additional materials that may end up as

resistance in the system. From this point of view, Ir-Ni aerogel was fabricated as an electrocatalyst structure. Aerogel is self-supporting 3D structure, which is unnecessary to be supported by other materials. This enables not only to prevent the cell degradation possibly caused from the dissolved additional materials, but also to utilize the volume more efficiently instead of it. Next, it supplies a large specific surface area with the hierarchical and porous morphology. Due to the physical properties, the density is significantly low that is known as  $0.003 - 0.15 \text{ mg}\cdot\text{cm}^{-3}$  depending on the material, which has a possibility to save the cost for cell design. Furthermore, it is environmentally friendly reaction compared with other synthesizing methods for materials preparation, because the syntheses for aerogel are based on the water in general, not toxic chemicals. The Ir-Ni aerogel was successfully synthesized here that consists of hollow nanoparticles mixed with iridium and nickel, achieved by controlling the reaction rate without post-treatment, called as '*in-situ* leaching out effect' here. The Ir-Ni aerogel was evaluated in single cells and showed the catalytic activity corresponding to the commercial IrO<sub>2</sub> after 500 hours of durability test. It enabled the observation of cell characteristics when the electrocatalysts alloyed with 3d transition metals are applied in comparison with original cell using the commercial IrO<sub>2</sub> and showed the potential to substitute the state-of-the-art IrO<sub>2</sub> catalysts. In the following chapters, each nanostructure will be introduced.

### 3.1. Bimetallic Nilr hollow nanoframes<sup>146</sup>

#### 3.1.1. Synthesis of bimetallic Nilr hollow nanoframes

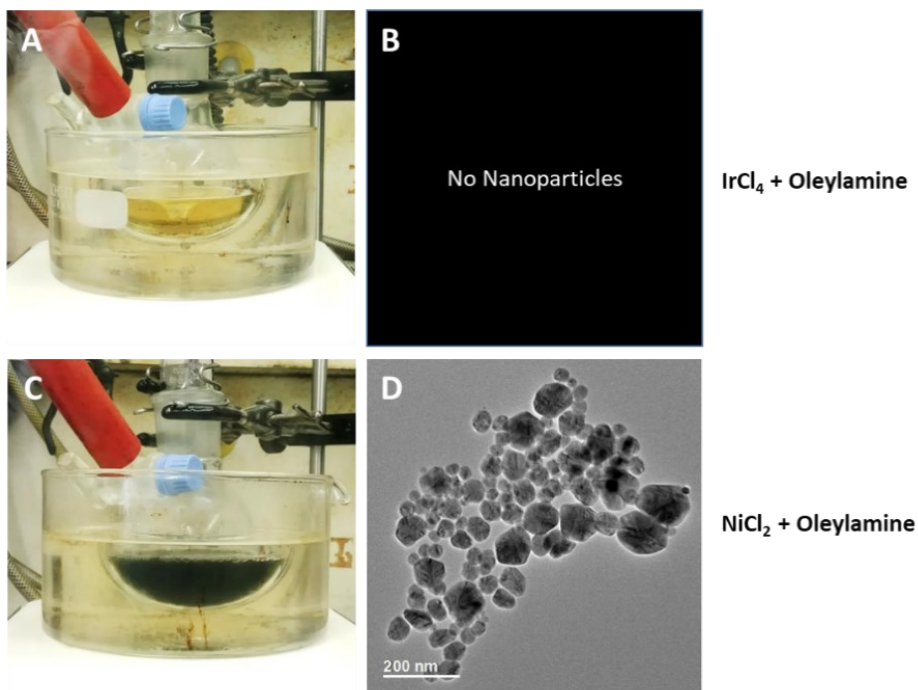
The synthesis of bimetallic Nilr hollow nanoframes was proceeded as two steps. Firstly, Nilr hexagonal nanostructures were synthesized by mixing 0.09 mmol of IrCl<sub>4</sub> and 0.12 mmol of NiCl<sub>2</sub> with 24.3 mmol of oleylamine in a round-bottom flask (100 ml). The oleylamine operated as reducing and capping agent at the same time. The flask was placed in an oil bath that was already heated at 100 °C and stirred for 30 min with flowing Ar gas. After that, the oil bath was heated to 260 °C and maintained at the temperature for 30 min. After the 30 min, the flask was cooled down naturally under the Ar atmosphere. When the solution was cooled to room temperature, it was washed with a mixture of toluene and ethanol several times until the transparent supernatant was achieved. Finally, the dark precipitates were obtained and dried overnight under vacuum conditions.

Next, the bimetallic Nilr hollow nanoframes were formed from the Nilr hexagonal nanostructures via leaching out procedure. The dried Nilr hexagonal nanostructures were dispersed again in the mixed solution of toluene, ethanol, and HCl with a 1:1:1 volume ratio. The mixture was then placed in a preheated oil bath at 70 °C for 1 hour. After being taken out, it was cooled down naturally to ambient temperature. The cooled solution was washed with ethanol three times. The precipitates were dried overnight under vacuum.

#### 3.1.2. Structure characterization

To fabricate the Nilr hollow nanoframes, uniform Nilr hexagonal nanostructures were synthesized first by *in-situ* wet chemical synthesis. *In-situ* synthesis requires highly delicate control of kinetics for the materials in the reaction under the experimental conditions since all the reactants can interact and affect each other at the same time. Accordingly, it is important to achieve a template first, followed by fabrication or deposition of the next materials. In this synthesis, nickel nanoparticles were formed first as the templates, and the iridium was deposited onto the nickel structure surface by the reduction of the iridium precursor. For verifying it each precursor was reacted alone under the same experimental conditions (**Figure 23**).

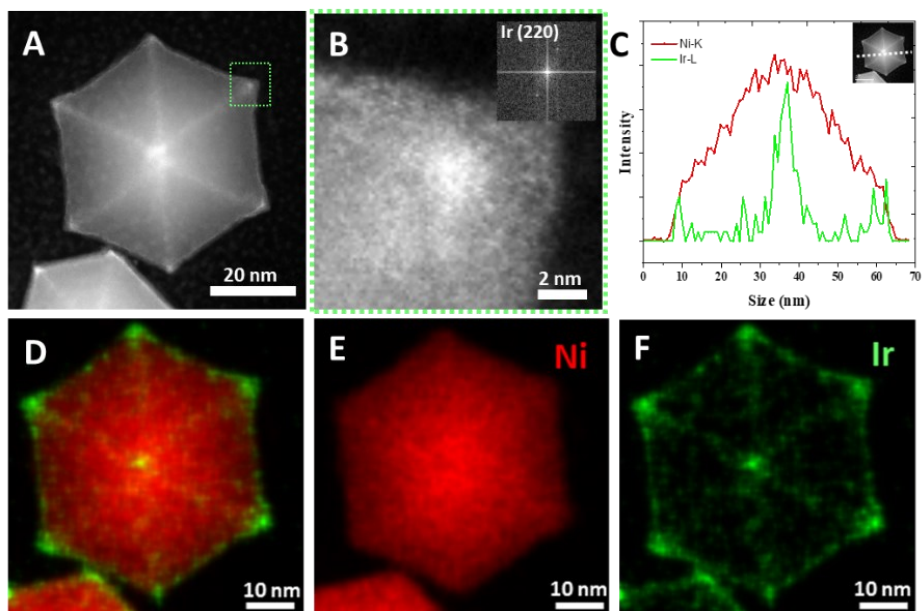
When iridium precursor was participated in the reaction without nickel precursor, iridium nanoparticles were not synthesized (**Figure 23A, B**), however, in the case that nickel precursor was reacted without iridium precursor, nickel nanoparticles with irregular shapes were observed (**Figure 23C, D**). It proves that nickel particles can be formed by themselves and the growth of iridium is induced during the synthesis in the presence of nickel nanoparticles.



**Figure 23.** Role of the metal precursors. (A, B) Photo when the iridium precursor is reacted alone; (C, D) photo when the nickel precursor is reacted alone and the TEM image of the corresponding product.

The uniform NiIr hexagonal nanostructures were observed by HAADF-STEM (**Figure 24**). **Figure 24A** shows a hexagonal nanostructure shape with a size of  $42 \pm 5$  nm, and **Figure 24B** indicated the enlarged high-resolution HAADF-STEM image

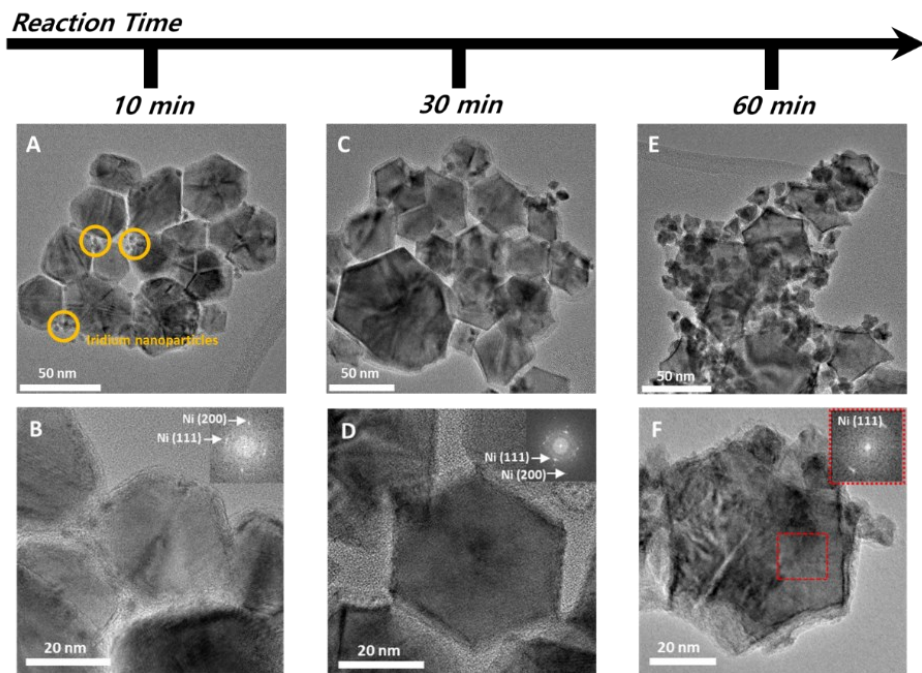
and Fast Fourier transformation (FFT) pattern of the area marked as green dash line in **Figure 24A**. It revealed the FCC structure of iridium by confirming the iridium (220) at the vertex of the shell. **Figure 24C** shows the line profile scanning along the white dash line of NiIr hexagonal nanostructure in inset, which indicates that the inner part of the nanostructure consists of nickel symmetrically (red line) and the iridium is mostly distributed on the edges and vertices (green line). The strong intensity in the center emphasizes its hexagonal structure and iridium focused on the vertices that is explained by the overlapped area along the white line. The corresponding elemental distributions by EDX elemental mapping confirmed visually that iridium atoms are concentrated on the edges and vertices of nickel nanostructure that have higher surface energy than facets, which are also more active for catalytic reaction (**Figure 24D-F**).<sup>65,147</sup> The atomic composition of NiIr hexagonal nanostructure was analyzed as 97.0 at% of nickel and 3.0 at% of iridium by EDX.



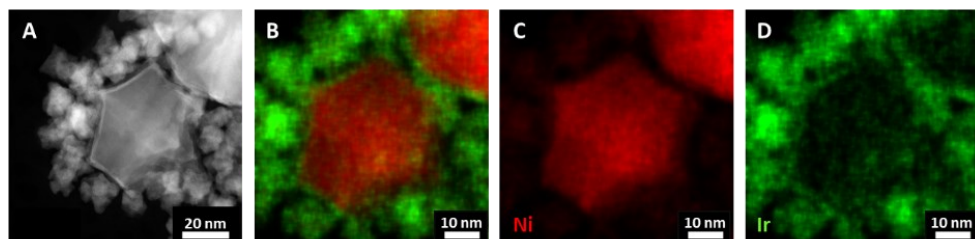
**Figure 24.** Morphology and composition profile analysis of the pristine NiIr hexagonal nanostructure. (A) HAADF-STEM image; (B) magnified view of the selected

green area with high resolution HAADF-STEM and FFT pattern; (C) line scan analysis of NiIr hexagonal nanostructure along the white dash line of inset; and (D-F) the corresponding elemental distribution of nickel and iridium maps.

For better understanding of the growth mechanism of NiIr hexagonal nanostructures, the growth of particles was studied as the reaction time by TEM characterization (**Figure 25**). After 10 min of the reaction start, nickel nanoparticles were already observed with the size of around 20 nm but showed irregular shapes (**Figure 25A**). From the FFT pattern, (111) and (200) for nickel FCC structure were confirmed (**Figure 25B**). In the meantime, small iridium nanoparticles started to form, which are observed between the nickel nanoparticles. When the reaction continues for 30 min, the nickel emerges as a hexagonal structure (**Figure 25C, D**). It presents a uniform size distribution with the clear and thin outer shells. Meanwhile, the further growth of iridium nanoparticles is barely observed, but the small iridium nanoparticles formed the outer shell of the NiIr hexagonal nanostructures. If the reaction goes further until 60 min, the nickel nanoparticles overly grow and transform to irregular shapes (**Figure 25E, F**). Moreover, the iridium nanoparticles cease to form the shell thicker further but progress their own nucleation again. Xia et al. reported that iridium requires lower energy for homogeneous nucleation than that for heterogeneous nucleation, which explains why iridium started to grow itself, rather than being deposited onto the structures further.<sup>148</sup> **Figure 26** shows the dramatically increased amount of iridium nanoparticles with the size of around 5 nm surrounding the overly grown NiIr nanostructures when the reaction proceeds for 60 min. Accordingly, the reaction time here was restricted as 30 min to achieve the desired structure.

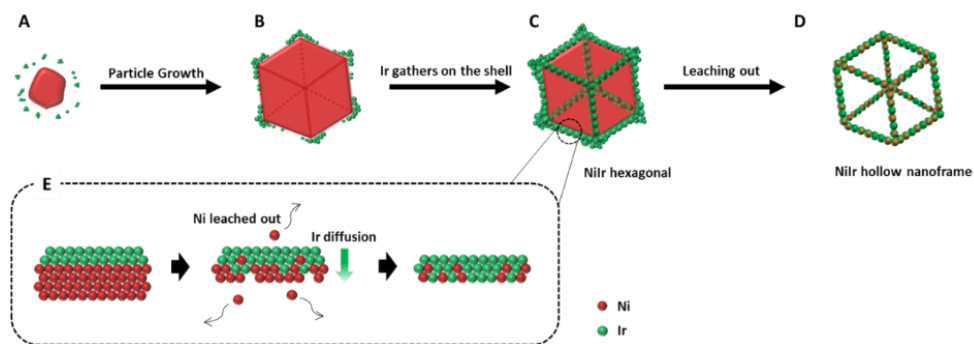


**Figure 25.** Growth study of NiIr nanostructures as the reaction time. High resolution TEM images of the products and magnified views when the reaction time was (A, B) 10 min; (C, D) 30 min; (E, F) 60 min with the FFT patterns (each inset in B, D, F)



**Figure 26.** (A) HAADF-STEM image and (B-D) corresponding elemental distribution of nickel (red) and iridium (green) across the EDX composition maps for the reaction products at 60 min.

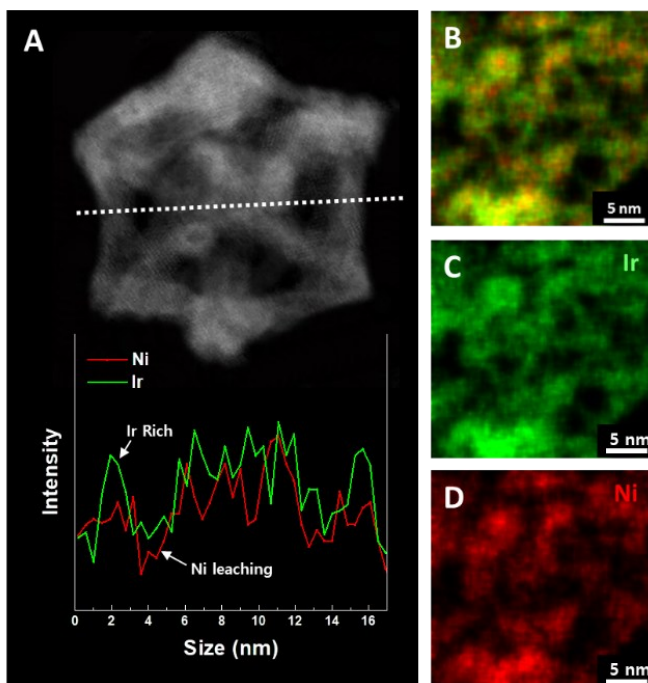
To fabricate the NiIr hollow nanoframes, the NiIr hexagonal nanostructures underwent leaching out using 4 M of strong acidic solution as the etchant. Through the leaching step, the nickel core part was removed from the structure, and in the meantime, the well-alloyed hollow nanoframe structure was achieved via 'Kirkendall effect'. To assist the explanation, the entire fabrication procedure of NiIr hollow nanoframes was described in a schematic illustration briefly (**Figure 27**). As explained previously, the irregular shape of nickel nanoparticle starts to form a structure first at the beginning of reaction and small iridium nanoparticles surround it (**Figure 27A**). As the reaction proceeds, the iridium nanoparticles gather near the high surface energy area such as edges and vertices of nickel nanostructure and attach along the edges of it to form the NiIr hexagonal nanostructure (**Figure 27B, C**). The synthesized NiIr hexagonal nanostructure loses the nickel inner part through leaching out procedure, which induces the NiIr hollow nanoframe. **Figure 27E** illustrates what occurs during the leaching step especially in the edge area closer. When the nickel atoms are etched, vacancies are generated and those can be utilized as paths for the migration of iridium atoms. Along the vacancies that nickel atoms made, iridium atoms diffuse inward, which leads the well-distributed alloy frame with the remaining nickel (**Figure 27D**).



**Figure 27.** Schematic illustration of the formation of the NiIr hollow nanoframe. (A-C) Formation of the NiIr hexagonal nanostructure; (D) the NiIr hollow nanoframe after the leaching out step; and (E) the enlarged description of the edge area during the leaching.

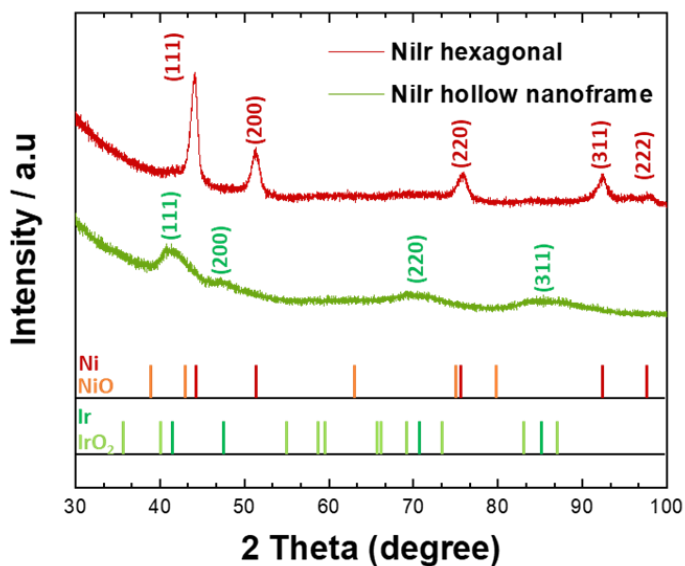


**Figure 28** shows the NiIr hollow nanoframe after the leaching procedure. The hollow nanoframe preserves the original hexagonal-shaped structure well, but without the nickel bulk inside (**Figure 28A**). The line scan profile along the white dash line confirms the hollow area caused by the loss of inner nickel with the low intensity (red line) and iridium-rich frame through the stronger intensity for iridium (green line) than nickel overall. The corresponding EDX elemental mappings demonstrate again that nickel and iridium were evenly distributed with the composition of 28 at% of nickel and 72 at% of iridium (**Figure 28B-D**).



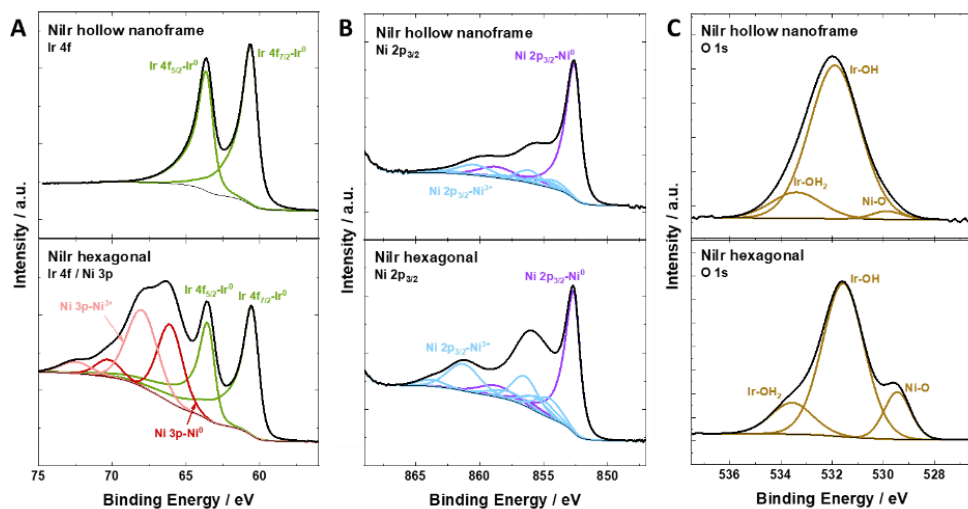
**Figure 28.** Morphology and composition profile analysis of the NiIr hollow nanoframes. (A) A high-resolution HAADF-STEM image of NiIr hollow nanoframe and a line scan profile along the white dash line; (B-D) the elemental distribution of iridium (green) and nickel (red) in the EDX.

XRD analysis was performed to observe the change in crystallinity of the NiIr nanostructures before and after the leaching step, presented in **Figure 29**. The diffraction patterns for Ni (red), NiO (orange), Ir (green), IrO<sub>2</sub> (light green) were indicated at the bottom of the graph. The NiIr hexagonal nanostructure presents the nickel FCC structure (JCPDS 04-0850) by showing the nickel (111), (200), (220), and (311) peaks, which supports the nickel inner structure clearly. The XRD pattern for iridium was not distinguished in the XRD spectrum, which is attributed to the thickness of the iridium wall less than 2 nm on the nickel hexagonal nanostructures. In contrast, from the XRD pattern for the NiIr hollow nanoframes after leaching, nickel peaks disappeared but the XRD pattern for metallic iridium FCC (JCPDS 06-0598) appeared broadly with a slight shift. It reflects that the nanostructure mainly consists of iridium and alloying with nickel affects the crystallinity.



**Figure 29.** XRD patterns of NiIr hexagonal nanostructures (before leaching) and NiIr hollow nanoframes (after leaching).

XPS was performed to determine the oxidation and chemical states of the surface of the NiIr hexagonal nanostructures and NiIr hollow nanoframes (**Figure 30**). The nickel 2p and iridium 4f regions were studied to compare the change of metallic and oxide surface species. **Figure 30A** shows the Ir 4f region of NiIr hexagonal nanostructures and NiIr hollow nanoframes, indicating that both materials have metallic iridium surface with Ir<sup>0</sup> spectra. The Ni 2p<sub>3/2</sub> region presents that the NiIr hexagonal nanostructures possess mixed composition with metallic Ni<sup>0</sup> and Ni<sup>3+</sup> components as 1:1 ratio (**Figure 30B**). It is also confirmed in the Ni 3p region which is overlapped with the Ir 4f signal. However, after leaching out the nickel spectra in the Ni 3p region vanished in the NiIr hollow nanoframes, moreover, the oxidized nickel peaks in Ni 2p<sub>3/2</sub> region decreased remarkably from 50.7 at% to 30.9 at%. It proves that the unstable nickel on the surface of the NiIr hexagonal nanostructures was removed during leaching out, which remained mostly a metallic nickel on the surface in the end. Meanwhile, **Figure 30C** indicates the XPS spectra in O 1s region that are related to nickel oxide, iridium hydroxide, and adventitious peak usually meaning adsorbed water (marked as Ni-O, Ir-OH, Ir-OH<sub>2</sub>). When compared with NiIr hexagonal nanostructure, NiIr hollow nanoframe shows drastically weakened Ni-O peak from 14.0 at% to 2.7 at% and Ir-OH peak that became stronger as 83.2 at% than before (71.4 at%). The peak indicating Ir-OH<sub>2</sub> rarely showed a difference with 14.6 at% to 14.1 at%, which explains that the increase of Ir-OH on the surface after leaching out mostly originated from the decrease of Ni-O spectra. During the leaching out procedure, the oxygen atoms lose their binding partners due to the absence of nickel, which induces the linkage of proton in the electrolyte to form the hydroxyl group. The hydroxyl group on the catalyst surface has been reported a lot as one of the factors boosting the OER more efficiently,<sup>149–152</sup> which will be discussed later with the electrochemical performance. To sum up, the XPS result supports that the surface of NiIr hollow nanoframes consists of metallic iridium, metallic nickel, and increased Ir-OH.



**Figure 30.** XPS result of NiIr hexagonal nanostructures and NiIr hollow nanoframes in the (A) Ir 4f / Ni 3p, (B) Ni 2p<sub>3/2</sub>, and (C) O 1s regions.

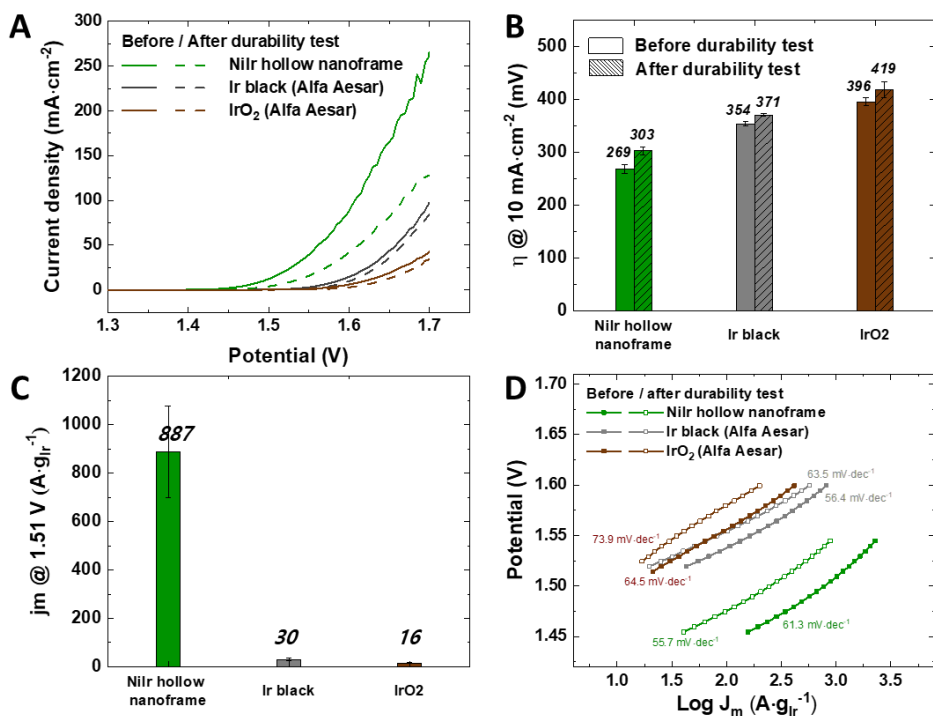
### 3.1.3. Electrochemical measurements

The electrocatalytic performance of the NiIr hollow nanoframes was evaluated via a three-electrode system by comparison with commercial iridium nanoparticles, Ir-black and IrO<sub>2</sub> from Alfa Aesar (**Figure 31**). **Figure 31A** shows the OER polarization curves for NiIr hollow nanoframes and commercial iridium nanoparticles. For the overpotentials to reach 10 mA·cm<sup>-2</sup>, NiIr hollow nanoframes requested 269 mV, on the contrary, the commercial Ir-black and IrO<sub>2</sub> needed 354 mV and 396 mV, respectively (**Figure 31B**). The calculated average-iridium mass activity at 1.51 V for the NiIr hollow nanoframes was 887 A·g<sub>Ir</sub><sup>-1</sup>, when the commercial Ir-black and IrO<sub>2</sub> presented 30 A·g<sub>Ir</sub><sup>-1</sup> and 16 A·g<sub>Ir</sub><sup>-1</sup> respectively (**Figure 31C**), which is 29-fold improved mass activity than the commercial ones. This remarkable improvement is explained as the structural merits the NiIr hollow nanoframes have. Its hollow structure can decrease the materials inside that cannot be involved in the electrocatalytic reaction. Moreover, it enables the atoms on the inner wall of the structures accessible to the catalytic reaction. As shown in the STEM images of the NiIr hollow nanoframe, it exposed the

iridium on the surface very efficiently, which leads to the better utilization of iridium.<sup>107,153</sup> Furthermore, it was confirmed that the NiIr hollow nanoframe has FCC structure with (111) facets. The (111) facet is the most preferred for electrocatalysts in general cases, since it possess the higher atomic packing density than other facets, which induces more possibility of occurrence for the reaction.<sup>154</sup> Besides, the surface of NiIr hollow nanoframe consists of metallic iridium and nickel, with increased Ir-OH species achieved during leaching. The metallic surface is more beneficial than oxidized surface for catalytic reactions, and in particular, the Ir-OH species are known as a critical factor in the improvement of OER.<sup>149–152</sup> The hydroxyl group (Ir-OH) is reported to be generated when the nickel is leached out. During leaching of nickel, the oxygen atom that is held by iridium and nickel loses nickel at one side, and then captures proton from electrolyte instead, which forms the hydroxyl group on iridium (Ir-OH). Abbott et al. reported that the presence of Ir-OH species on the surface of IrO<sub>x</sub> are strongly connected to the high catalytic activity via the study using operando X-ray absorption spectroscopy (XAS) and XPS.<sup>149</sup> Four kinds of iridium oxide were prepared depending on the different synthetic conditions, which gave them different properties in surface area, pore conditions and surface property. The materials were evaluated as electrocatalysts, and when their electrocatalytic activity was normalized with their surface area, the results showed the correlation between the improvement in the electrocatalytic activity and the hydroxide layer on the catalyst surface. Godínez-Salomón et al. showed that the interaction between iridium and nickel on the surface can lower the activation energy for OER via DFT.<sup>151</sup> In this study, two-dimensional (2D) Ni-Ir nanoframes were prepared by thermal treatment at the two different temperature of 200 °C (NiIr-200) and 300 °C (NiIr-300) and chemical leaching, which was analyzed that both of materials possessed the hydroxyl group on the surface that achieved during synthesis. The NiIr-200 showed a relatively higher ratio of hydroxyl group than the NiIr-300, which is attributed to the higher mass activity of the NiIr-200. From the XPS results for NiIr hollow nanoframes here, it was confirmed that the decrease of Ni-O species and the increased Ir-OH species on the surface of NiIr hollow nanoframes were acquired with the chemical leaching step, which contributes to the boosted electrocatalytic activity.

To evaluate the durability of electrocatalyst, an aging test was performed by

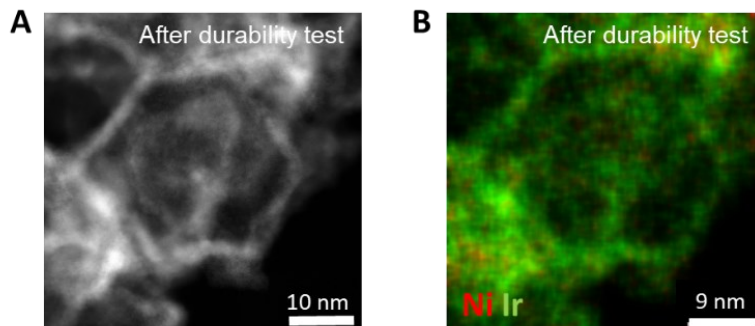
cycling in the load range between 1.1 V and 1.6 V with a scan rate of 100 mV·s<sup>-1</sup> for 1,000 times. After the durability test, it was confirmed that the overpotential of the NiIr hollow nanoframes increased by 13 %, when Ir-black and IrO<sub>2</sub> increased by 5 % and 6 %, respectively. However, the NiIr hollow nanoframes still presented the lower overpotential than the commercial iridium nanoparticles (**Figure 31B**). Based on the results, Tafel slopes were analyzed to study the kinetics of the OER process (**Figure 31D**). In the beginning, the Tafel slopes were all similar around 60 mV·dec<sup>-1</sup>, which is a typically observed Tafel slope for iridium catalysts. It means that the reaction for oxygen evolution is mostly focused on the formation of the 'activated hydroxyl group' on the surface as a rate-determining step.<sup>155</sup> The Tafel slopes after the aging test were not degraded much, but showed slight increases from 56.4 mV·dec<sup>-1</sup> to 63.5 mV·dec<sup>-1</sup> and from 64.5 mV·dec<sup>-1</sup> to 73.9 mV·dec<sup>-1</sup> for Ir-black and IrO<sub>2</sub>, respectively. In contrast, the NiIr hollow nanoframes showed the opposite result that the Tafel slope even decreased after the 1,000 cycles from 61.3 mV·dec<sup>-1</sup> to 55.7 mV·dec<sup>-1</sup>. It is speculated that the decrease in Tafel slopes is caused by the unstable nickel leached during the measurements. Since the electrochemically leached nickel will generate additional hydroxyl group on the catalyst surface likewise, the kinetics for OER can be boosted.



**Figure 31.** Electrocatalytic performance of the NiIr hollow nanoframes by comparison with commercial Ir-black and IrO<sub>2</sub>. (A) OER polarization curves of the NiIr hollow structures and commercial Ir-black and IrO<sub>2</sub> measured in 0.5 M H<sub>2</sub>SO<sub>4</sub> before and after the durability test; (B) bar graphs displaying the overpotentials to drive 10 mA·cm<sup>-2</sup>; (C) Ir mass activities at 1.51 V (vs. RHE); (D) Tafel plots before and after the durability test.

The NiIr hollow nanoframe was characterized after the durability test to study its structural stability (**Figure 32**). As shown in TEM images, it sustained the frame structure well without collapse; however from the corresponding elemental mapping, it was observed that most of the nickel was leached and remained only less than 3 at%. To confirm that the nickel was leached electrochemically, ICP-MS was performed with the electrolyte after the durability test. Within the electrolyte, 0.9 wt% of iridium

and 18.0 wt% of nickel among the amount coated onto the electrode were detected.



**Figure 32.** (A) Morphological characterization of the NiIr hollow nanoframe after the durability test and (B) the corresponding elemental mapping.

Although most of nickel is electrochemically leached during the measurements, it contributed to the improved kinetic for OER by forming more hydroxyl group on the electrocatalyst surface. Besides, the hollow structure was maintained without any destruction, even though the frame-shaped structures normally have a weakness regarding the structural durability due to the thin walls. The structural stability shown here can be achieved from the bimetallic effect.<sup>125,156,157</sup> Beermann et al. showed that the third element doping can even help the stabilization of nanostructures by suppression of the migration for the other elements.<sup>125</sup> Wu et al. explained that the effect can be released via dealloying and re-alloying that repeated during cycling.<sup>129</sup> Through the *in-situ* / operando high-energy synchrotron X-ray diffraction, they analyzed the atomic phase structures and strains with their Pt-Pd-3d transition metal nanoparticles, which revealed that alloy catalysts with optimal alloying elements can achieve the efficient compressive strain after cycling and it is related to the improvement in the activity and thermodynamic stability. Based on these, it is interpreted that the 3 at% of remaining nickel in the NiIr hollow nanoframe structure is working for the structural robustness, and it will prolong the lifespan of electrocatalysts



by refraining the agglomeration or destruction of electrocatalysts.

### 3.1.4. Summary

The nickel nanostructure was used here as a basic template to control the shape of the final structure. While the growth mechanism was investigated, it was found that the nickel nanostructures were formed first and the iridium nanoparticles grew on the nickel surface, which is explained by the fact that they required different amounts of energy for nucleation and growth. The synthesis was sensitively controlled as the results could be dramatically changed depending on the reaction time.

The NiIr hexagonal nanostructure was synthesized as core-shell structure first, and it went through selective leaching out step to remove the nickel core part and induce the hollow structure. The NiIr hollow nanoframe was obtained as well-alloyed iridium-rich (72 at%) hollow nanostructure via Kirkendall effect, with the increased hydroxyl group on the surface that was achieved from the leaching of nickel. The NiIr hollow nanoframe showed  $887 \text{ A}\cdot\text{g}_{\text{Ir}}^{-1}$  of highly improved electrocatalytic activity (29-fold) at 1.51 V compared with commercial iridium nanoparticles, which is interpreted as the combined effect of structural advantages the NiIr hollow nanoframe has. After the 1,000 cycles of durability test, it still maintained the hollow frame-shaped structure well without any structural collapse despite the frame wall was thin less than 2 nm. Considering other studies,<sup>125,156,157</sup> it is explained that the remaining nickel less than 3 at% in the structure is working for the structural durability as the bimetallic composition effect by constraining the migration of atoms and alloying with iridium stronger as the cycles proceed. In conclusion, the NiIr hollow nanoframe was successfully synthesized for electrocatalysts and showed the enhanced electrocatalytic activity and stability in acidic media, which can be explored further for being tuned or applied to a single cell.

## 3.2. Highly uniform IrO<sub>2</sub> nanospheres<sup>158</sup>

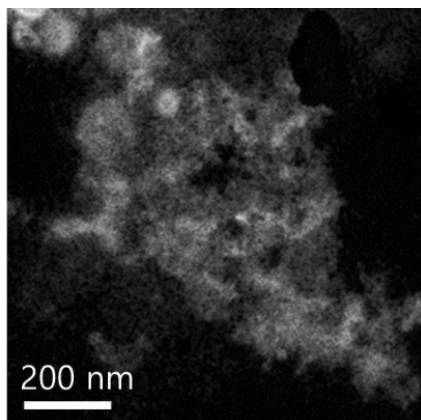
### 3.2.1. Synthesis of highly uniform IrO<sub>2</sub> nanospheres

To synthesize  $\alpha$ -MnO<sub>2</sub> nanowire, 2.8 mmol of KMnO<sub>4</sub> was dissolved in DI water with addition of 11.2 mmol of HCl. A total 60 ml of aqueous solution was stirred for 20 min and transferred to a Teflon autoclave cell. The solution was heated to 240 °C and kept for 3 hours. After 3 hours, the solution was cooled down naturally to room temperature and washed with ethanol and DI water by vacuum filtration. The obtained dark brownish precipitates were dried overnight under vacuum conditions.

The uniform IrO<sub>2</sub> nanospheres were fabricated by polyol method. For the first step, 0.009 mmol of Polyvinylpyrrolidone (PVP) and 1.7 mmol of L-Ascorbic acid were mixed with 25 ml of Ethylene glycol (EG) in a Schlenk flask (volume: 250 ml). The materials were vigorously stirred in a preheated oil bath at 100 °C with Ar flowing. After 1 hour,  $\alpha$ -MnO<sub>2</sub> nanowires dispersed in 25 ml of EG was added, followed by heating to 220 °C. At 220 °C, H<sub>2</sub>IrCl<sub>6</sub> was dissolved in 15 ml of EG and injected. The reaction was kept for 20 min and cooled down naturally. After the solution cooled down to room temperature, the content was washed with ethanol and acetone by centrifugation until the transparent supernatant was achieved. The dark precipitates were dried overnight under vacuum conditions.

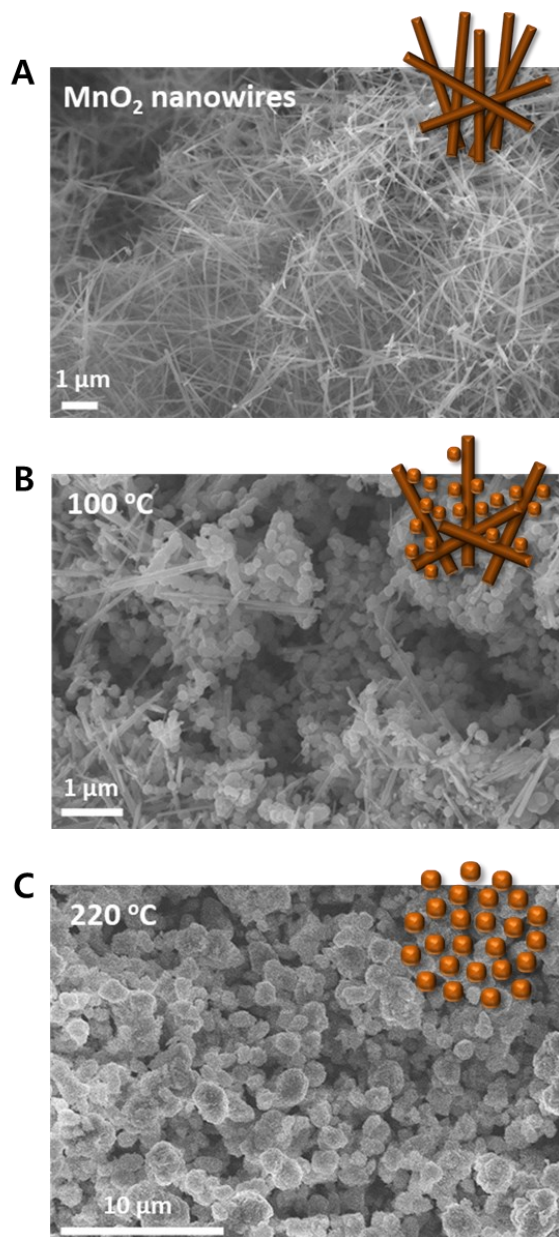
### 3.2.2. Structure characterization

For the design of a well-controlled structure for iridium oxide nanoparticles, MnO<sub>2</sub> nanoparticle was utilized as a template, since it can be easily prepared in a large scale and frequently reported for cation exchange reaction.<sup>159–162</sup> The existence of a sacrificial template in this synthesis is crucial in the final morphology of iridium oxide nanoparticles because when iridium precursor was reacted alone, it rarely showed a certain structure (**Figure 33**).



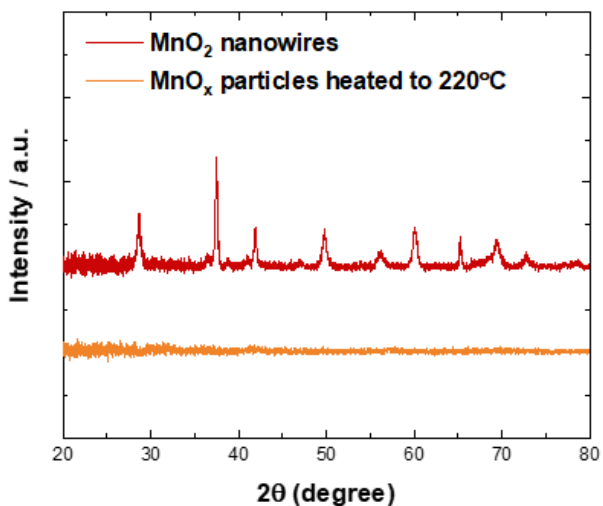
**Figure 33.** HAADF-STEM image of iridium product when the reaction is proceeded without manganese material.

The  $\text{MnO}_2$  nanowires were simply prepared by the hydrothermal method. To investigate the effect of temperature condition, the  $\text{MnO}_2$  nanowires were observed during heating, which revealed that the  $\text{MnO}_2$  nanowires transformed into round particles while the temperature was raised to 220 °C for reaction (**Figure 34**). The thermodynamic properties of manganese oxide have been reported previously.<sup>163–165</sup> Manganese oxide experiences changes in structure and morphology depending on the heat treatment and oxygen partial pressure. In general, when the temperature increases,  $\text{MnO}_2$  is reduced to  $\text{Mn}_2\text{O}_3$ ,  $\text{Mn}_2\text{O}_3$  is reduced to  $\text{MnO}$  with structural transformation, and this change is accompanied by oxygen evolution. In this synthesis, the transformation might be more facilitated since the reaction was carried out under Ar flowing to sustain an inert atmosphere. The observed morphological changes of our  $\text{MnO}_2$  nanowires by SEM were presented with schematic illustrations as insets (**Figure 34**). In the beginning, the pristine  $\text{MnO}_2$  nanowires showed clear wire-shaped structures (**Figure 34A**), but during heating to 100 °C, some of the nanowires turned into roundish particles (**Figure 34B**). When the temperature reached 220 °C, the  $\text{MnO}_2$  nanowires completely transformed into the aggregated round-shaped particles (**Figure 34C**).



**Figure 34.** SEM images with illustration for morphological change of MnO<sub>2</sub> nanowires as the heating temperatures; (A) pristine MnO<sub>2</sub> nanowires, and when heated to (B) 100 °C, (C) 220 °C.

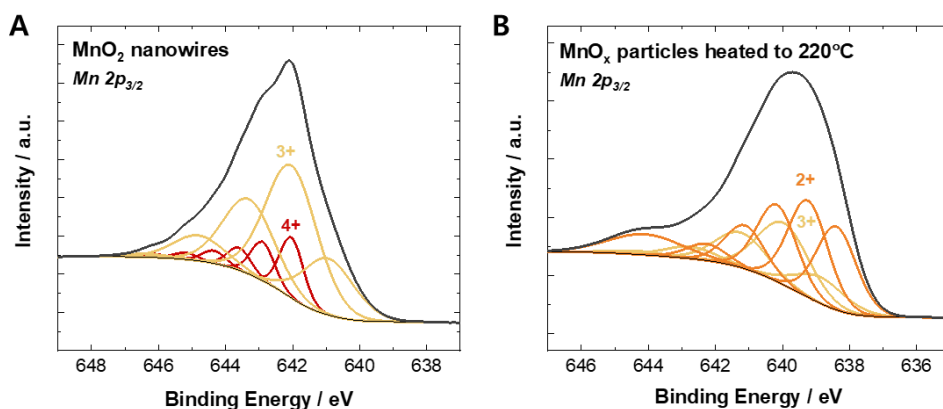
XRD measurements were performed to investigate the changes in crystallinity for the pristine MnO<sub>2</sub> nanowires and the MnO<sub>x</sub> particles heated at 220 °C (**Figure 35**). It shows that the pristine MnO<sub>2</sub> nanowires have peaks matching to the  $\alpha$ -phase MnO<sub>2</sub> (JCPDS No.44-0141). However, these became amorphous after being heated to 220 °C, which implies that the thermal treatment strongly affects the loss of crystallinity.



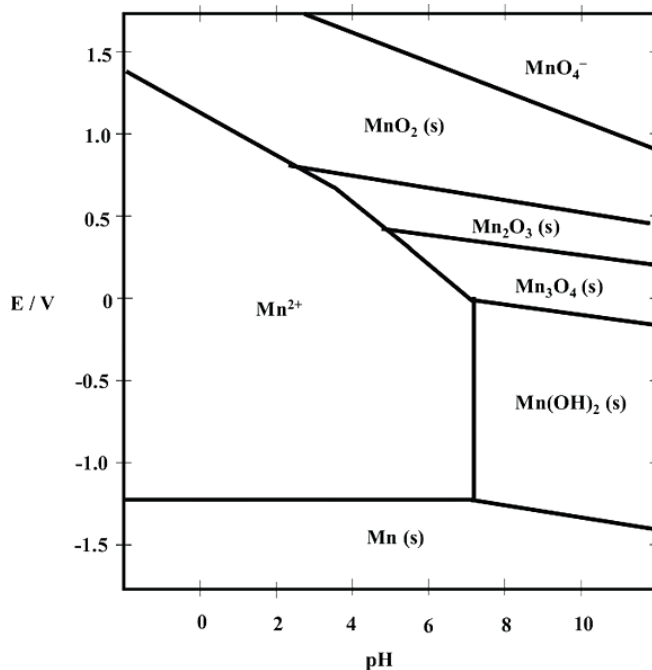
**Figure 35.** XRD pattern for the pristine MnO<sub>2</sub> nanowires and MnO<sub>x</sub> particles after heating to 220 °C.

To determine a change in the oxidation and chemical states of the surfaces, XPS was measured (**Figure 36**). The pristine MnO<sub>2</sub> nanowires indicated the majority of Mn<sup>4+</sup> with 69.1 at% and Mn<sup>3+</sup> with 30.9 at% in the Mn 2p<sub>3/2</sub> spectral region (**Figure 36A**). However, the MnO<sub>x</sub> particles heated at 220 °C showed Mn<sup>3+</sup> peaks weakened to 33.3 at% and Mn<sup>2+</sup> peaks intensified with 66.7 at% of higher ratio. It confirms not only the formation of MnO but also the reduction of manganese from Mn<sup>4+</sup> to Mn<sup>2+</sup> induced by temperature heating. When considered the Pourbaix diagram for manganese, this reduction of MnO<sub>2</sub> nanowires operates in favor of the cation exchange reaction which will occur later (**Figure 37**). Below pH 7, manganese prefers

to exist as  $Mn^{2+}$  ions at zero potential. Considering that the reaction solution was in the pH range of 3 - 5 because of the L-ascorbic acid used as a reducing agent, and iridium precursor solution which will be added later is a strongly acidic solution (pH 0 - 1), it is no doubt that manganese dissolves as  $Mn^{2+}$  ions. Accordingly, the change of oxidation state to 2+ for manganese will accelerate the dissolution of manganese, which will lead to the spontaneous exchange reaction when the iridium precursors will be injected.



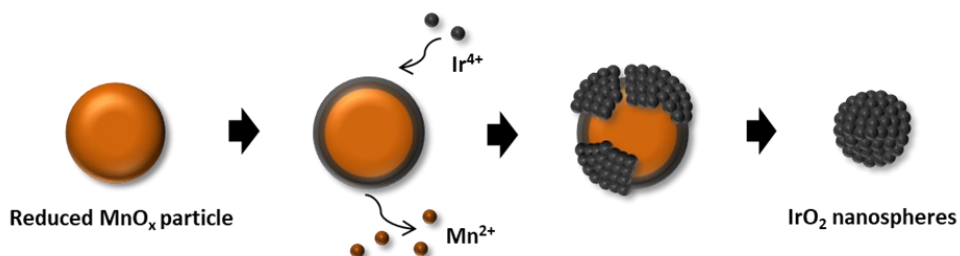
**Figure 36.** XPS spectra for (A) the pristine MnO<sub>2</sub> nanowires and (B) MnO<sub>x</sub> particles after heating to 220 °C.



**Figure 37.** The Pourbaix diagram for manganese.

When the temperature reached 220 °C, the iridium precursor was injected into the solution and the cation exchange reaction was initiated, as illustrated in **Figure 38**. The MnO<sub>x</sub> particles dissolved as Mn<sup>2+</sup> ions and the injected iridium ions were exchanged with the Mn<sup>2+</sup> ions via their kinetics at the reaction temperature; for example, the allowed energy for the dissolution of manganese and the precipitation of iridium, or the difference of solvent solubility of outgoing cation and ingoing cation.<sup>166</sup> It is speculated that the reducing agent also assisted the reduction and the exchange for iridium as well. During the reaction, PVP acted as a capping agent, converting the particles into smaller and uniform forms by preventing their aggregation. As the reaction was proceeded in the closed system, the intermediates could not be observed, however, ICP-MS was performed after finishing the reaction to detect the dissolved manganese and to prove the cation exchange reaction. At the end of the synthesis, the first supernatant from the washing process was obtained and analyzed. As a result,

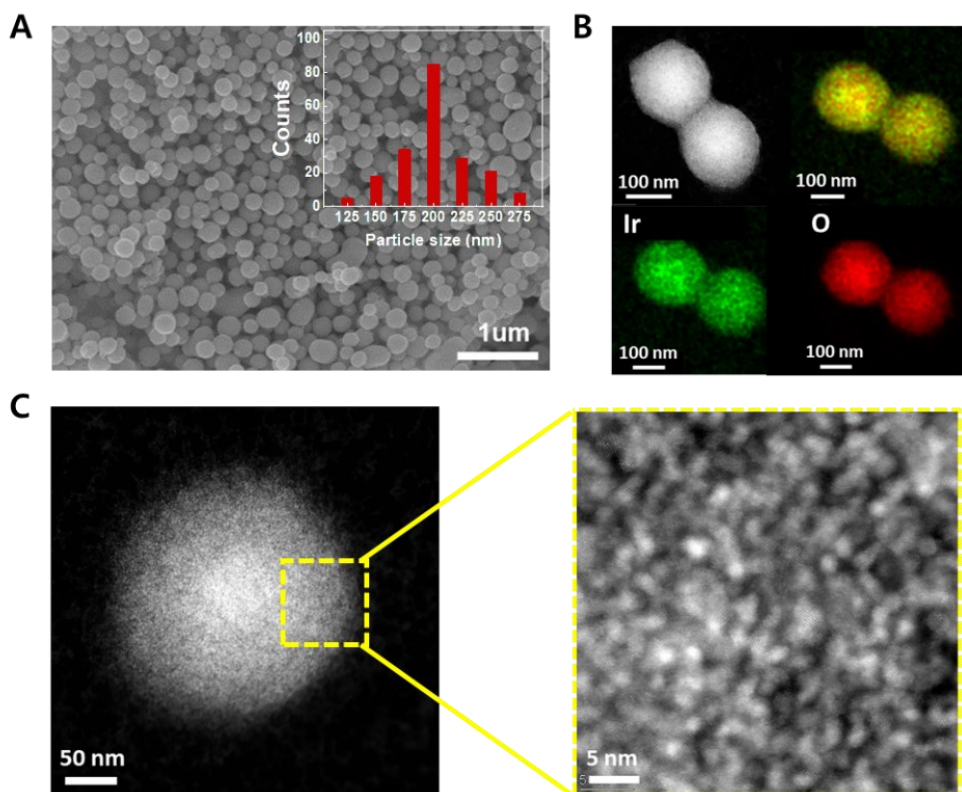
75 % of the manganese was detected in the first supernatant, showing that the manganese was successfully sacrificed and exchanged during the reaction. The remaining 25 % of the manganese was detected in the next washing steps.



**Figure 38.** Schematic illustration of the fabrication for  $\text{IrO}_2$  nanospheres.

**Figure 39A** shows the morphology of the synthesized  $\text{IrO}_2$  nanospheres observed using SEM. It shows the size distribution of the  $\text{IrO}_2$  nanospheres with  $201 \pm 32$  nm (inset). From the HAADF-STEM images and EDX analysis, it is clearly shown that the  $\text{IrO}_2$  nanospheres have a uniform spherical shape and are uniformly mixed with iridium and oxygen inside the structure (**Figure 39B**). The enlarged high-resolution HAADF-STEM images presented that the  $\text{IrO}_2$  nanospheres are composed of countless 2 nm of iridium oxide nanoparticles with some gap between the particles, suggesting that they were assembled by some surface interaction, for example, a ligand on the surface formed during synthesis (**Figure 39C**).

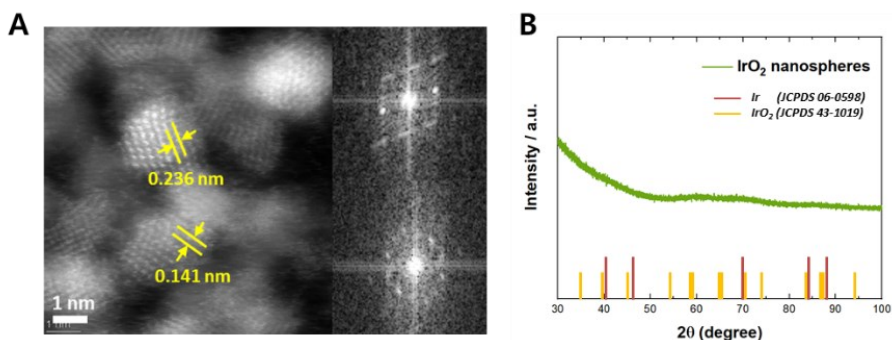




**Figure 39.** Morphological observation of IrO<sub>2</sub> nanospheres. (A) SEM image in low magnification, (B) HAADF-STEM images with elemental mapping, and (C) high-resolution HAADF-STEM image.

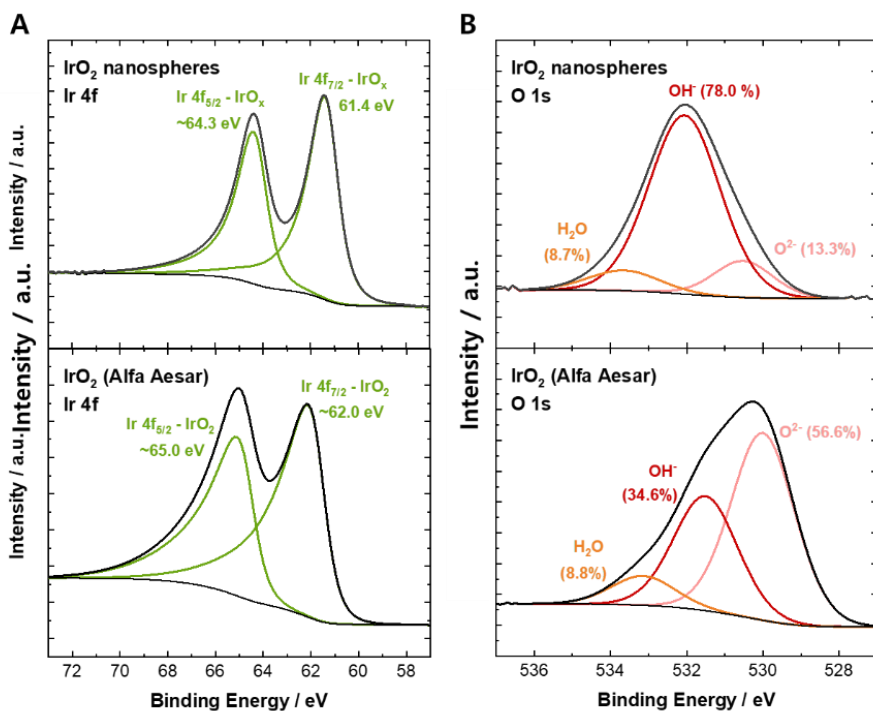
From the FFT pattern that applied to the high-resolution HAADF-STEM image, (200) planes with the d-spacing 0.236 nm and (310), (112), (301) planes with 0.141 nm for iridium oxide were revealed (**Figure 40A**). XRD was also analyzed to verify the crystallinity of the IrO<sub>2</sub> nanospheres (**Figure 40B**), however no diffraction peaks were detected. It is noteworthy that this inconsistent results between XRD and TEM analyses for crystallinity can take place for nanoscale materials.<sup>167,168</sup> For the samples are nanomaterials below 50 nm, it is tough to acquire a significant signal from the XRD measurement. When the particle size decreases, the intensity of peaks can be

diminished and the width of them becomes broader. Especially, in the case of nanoparticles below 5 nm, it is highly challenging to interpret the crystallinity of materials with only XRD results. Moreover, it should be more cautious in the evaluation of results if the orientations of the particles are not in the same direction, since the mixed orientations may offset the final intensity of the resulting peaks due to the misalignment. Considering that the IrO<sub>2</sub> nanospheres are assembled by numerous small iridium oxide nanoparticles (~2 nm) in random order, it is understandable that they present the amorphous pattern in the bulk XRD measurement.



**Figure 40.** The crystallinity of IrO<sub>2</sub> nanospheres; (A) FFT patterns from high-resolution HAADF-STEM image and (B) XRD pattern.

To determine the surface property XPS measurement was performed for IrO<sub>2</sub> nanospheres and commercial IrO<sub>2</sub> (**Figure 41**). **Figure 41A** shows the XPS spectra in the Ir 4f region indicating that both materials have the oxidized peaks that normally reported for IrO<sub>2</sub>, except that the doublets for IrO<sub>2</sub> nanospheres are placed in the slightly lower binding energy. The negatively shifted positions around 0.6 eV of IrO<sub>2</sub> nanospheres implicate that the electronic structure of iridium was affected. Meanwhile, the oxygen spectra presented considerably interesting results (**Figure 41B**).



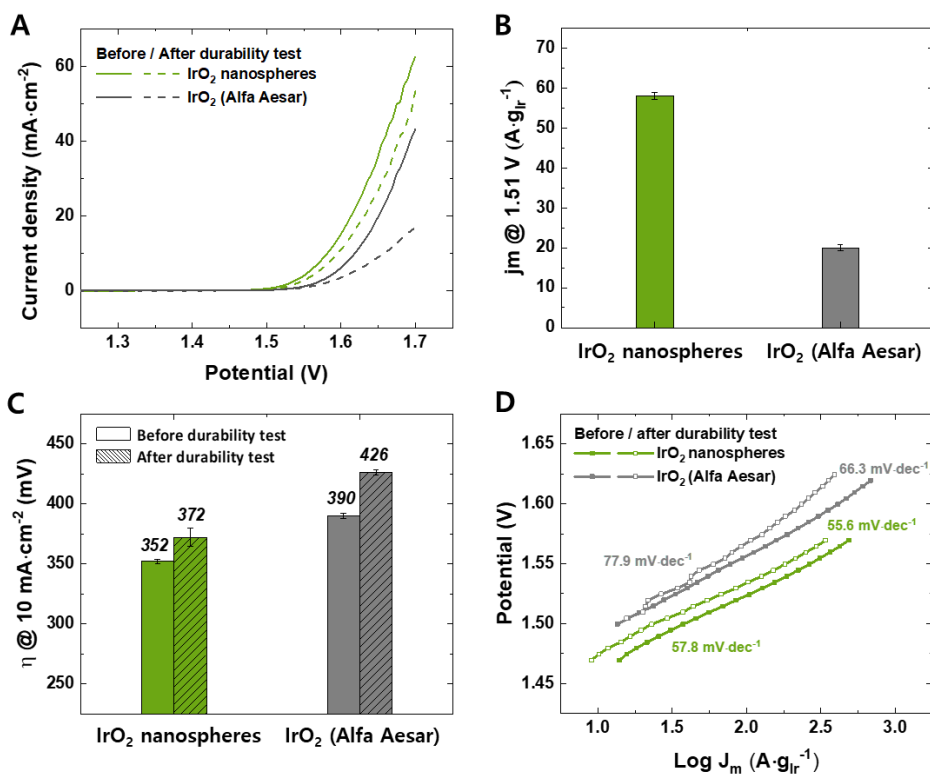
**Figure 41.** XPS spectra for IrO<sub>2</sub> nanospheres compared with commercial IrO<sub>2</sub> (Alfa Aesar) in (A) Ir 4f and (B) O 1s region.

In the O 1s region, oxygen spectra can be normally deconvoluted into three peaks: lattice oxygen (O<sup>2-</sup>), oxygen from hydroxyl group (OH<sup>-</sup>), and adventitious oxygen usually related to adsorbed water. In case of the IrO<sub>2</sub> nanospheres, it displays a strong hydroxide peak and lower oxide peak, with 78.0 % and 13.3 %, respectively. In contrast, the commercial IrO<sub>2</sub> possesses 56.6 % of higher oxide peak and 34.6 % of relatively lower hydroxide peak. The adventitious oxygen spectra were almost the same for both materials as 8.8 % and 8.7 %, which means that the different proportions of hydroxide for both materials are highly related to the proportions of oxide. It is speculated that the synthesis for IrO<sub>2</sub> nanospheres affected the surface property; in other words, the cation exchange reaction induced more hydroxyl group on the surface. The increased hydroxyl group could also explain the shift to the lower binding energy of Ir 4f doublets

for IrO<sub>2</sub> nanospheres, because the weaker bonding of hydroxyl group would be used instead of the stable divalent oxygen connected with iridium.<sup>152</sup>

### 3.2.3. Electrochemical measurements

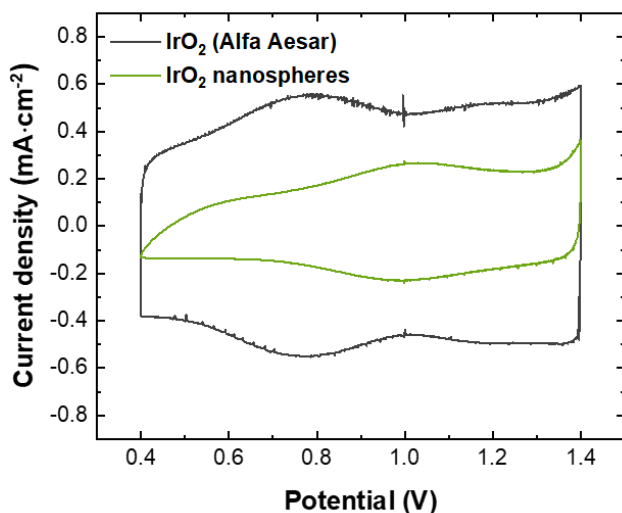
The IrO<sub>2</sub> nanospheres were evaluated as electrocatalysts for OER in 0.5 M H<sub>2</sub>SO<sub>4</sub> electrolyte. Prior to the evaluation of electrocatalytic performance, the electrochemically active surface area (ECSA) was determined by comparison with commercial IrO<sub>2</sub>. Since both materials have an oxidized surface, it was obtained by adopting the total anodic charges from the CV profiles after the double layer corrected in the potential range of 0.4 V – 1.25 V (vs. RHE), and 440  $\mu\text{C}\cdot\text{cm}^{-2}$  was used in the calculation as the electrical charge constant for the anodic processes.<sup>169</sup> To avoid the distortion of the result, the electrodes were swept enough from 0.05 V to 1.53 V (vs. RHE) until the cyclic voltammogram was stabilized. As a result, the ECSA for IrO<sub>2</sub> nanospheres and the commercial IrO<sub>2</sub> were confirmed as 16.45  $\text{m}^2\cdot\text{g}_{\text{Ir}}^{-1}$  and 20.43  $\text{m}^2\cdot\text{g}_{\text{Ir}}^{-1}$  respectively. Even though the final particle size is around 200 nm, the reason that IrO<sub>2</sub> nanospheres could achieve the comparable ECSA value may be attributed to the morphological uniformity, as well as the reachable surface of iridium oxide nanoparticles inside the structure. However, it is speculated that the actual surface area may be larger than the measured surface area value, since the ECSA still has some limitations such as an assumption that catalysts have a flat surface,<sup>170,171</sup> which is inconsistent to the IrO<sub>2</sub> nanospheres here. Meanwhile, Stevens et al. reported that a more uniform surface area is a competent characteristic as electrocatalysts since it boosts the frequency of adsorption with reactants as electrocatalysts.<sup>172</sup> From this point of view, it can be expected that IrO<sub>2</sub> nanospheres has an advantage to utilize their surface more efficiently than the irregular morphology of commercial IrO<sub>2</sub> as electrocatalysts.



**Figure 42.** Electrochemical measurements of IrO<sub>2</sub> nanospheres by comparison with commercial IrO<sub>2</sub> (Alfa Aesar). (A) OER polarization curves measured in 0.5 M H<sub>2</sub>SO<sub>4</sub> before and after chronoamperometry (CA) test for 5 hours (till 1.6 V vs. RHE); (B) Ir mass activities at 1.51 V (vs. RHE); (C) bar graphs displaying the overpotentials to drive 10 mA·cm<sup>-2</sup> before and after the CA test; (D) Tafel plots derived from OER polarization curves.

The electrochemical performance of IrO<sub>2</sub> nanospheres was compared to commercial IrO<sub>2</sub> in **Figure 42**. In advance of measuring OER performance, the electrocatalysts coated on GCE were activated by potential sweeping in the range of 0.4 V and 1.4 V (vs. RHE) at a scan rate of 500 mV·s<sup>-1</sup> for 45 cycles. The activation was followed by CV for the same load range, but at a slower scan rate of 50 mV·s<sup>-1</sup> to observe redox

peaks. In the case of commercial IrO<sub>2</sub>, it presented two oxidation peaks indicating oxidations of Ir(III) to Ir(IV) (~ 0.8 V) and Ir(IV) to Ir(V) (~ 1.2 V).<sup>173–175</sup> On the contrary, an exceptional oxidation peak was observed at ~ 1.0 V for the IrO<sub>2</sub> nanospheres, indicating not only the continuous oxidation from Ir(III) to Ir(V) but also the existence of hydrous oxide on the surface (**Figure 43**), which also supports the oxygen spectra for both electrocatalysts analyzed by XPS (**Figure 41B**).<sup>175</sup>



**Figure 43.** Cyclic voltammograms for IrO<sub>2</sub> nanospheres and commercial IrO<sub>2</sub> (Alfa Aesar).

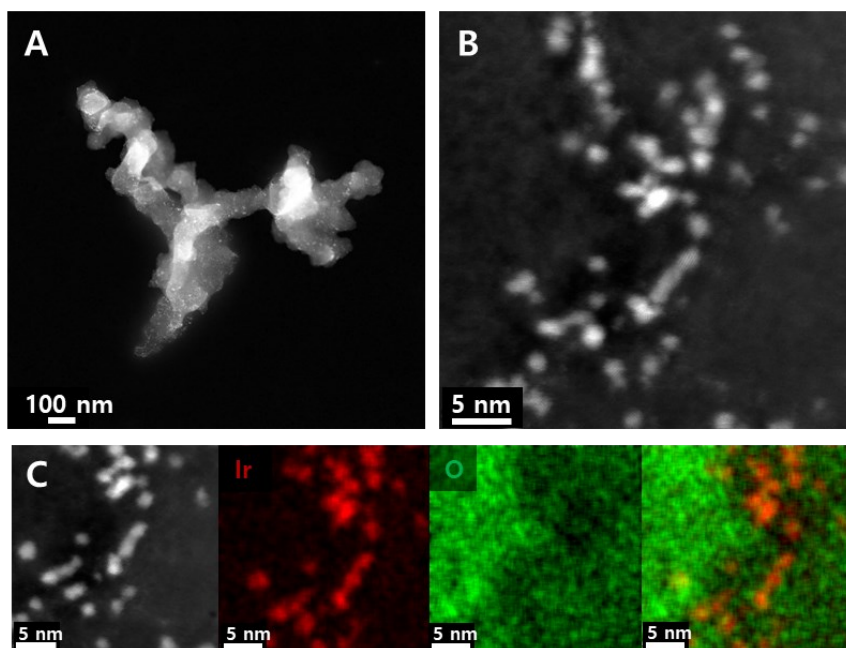
The OER activity was evaluated by LSV from 0.4 V to 1.7 V (vs. RHE) with a scan rate of 5 mV·s<sup>-1</sup> in oxygen saturated electrolyte (**Figure 42A**). The IrO<sub>2</sub> nanospheres showed higher activity of 58 A·g<sub>Ir</sub><sup>-1</sup> than the commercial IrO<sub>2</sub> of 20 A·g<sub>Ir</sub><sup>-1</sup> at 1.51 V, which corresponds to a threefold enhanced activity approximately (**Figure 42B**). It can be insisted that this improvement is attributed to the structural advantages of the IrO<sub>2</sub> nanospheres, the uniform structural morphology and the higher amount of hydroxyl group on the surface that generated during synthesis. Due to the irregular shapes and

uneven size distribution, commercial iridium nanoparticles are known to agglomerate and cause low efficient porosity and surface utilization,<sup>176</sup> whereas the uniform morphology of IrO<sub>2</sub> nanospheres can expose the surface more efficiently, which promotes the catalytic reaction eventually.<sup>177–181</sup> As reported earlier by others, particle size distribution is closely related to the catalytic activity and stability, which has been demonstrated on Pt/C nanoparticles by Liu et al.<sup>177</sup> This study proved that the specific activity of Pt/C always decreased when the particle size distribution is widened via theoretical calculation and modeling supported by experimental data. Furthermore, Wu et al. explained that electrode polarizations can be caused when particles have a wide size distribution, which is connected to a degradation and poor electrochemical performance.<sup>178</sup>

As shown in the XPS results, the IrO<sub>2</sub> nanospheres possess more hydroxyl group on the surface than commercial IrO<sub>2</sub>, which was generated during the synthesis of IrO<sub>2</sub> nanospheres. It was already explained in the previous chapter that the hydroxyl group is well known to play an important role in the improvement of electrocatalytic activity. To achieve the active hydroxyl group onto the surface of electrocatalysts, there have been some research intermittently reported that proceeded certain treatments after synthesizing the materials.<sup>149–151</sup> Here, it should be pointed out that the template material was fully exchanged during the synthesis and the hydroxyl group on the surface of electrocatalysts was acquired without any additional treatment. With the well-designed synthesis, further experimental steps can be avoided, as well as the degradation possibly caused from the dissolution of transition metals remaining in the structure can be prevented. Based on the previous research, it is convinced that the improved electrocatalytic activity of IrO<sub>2</sub> nanospheres is strongly affected by the increased hydroxyl group on the surface.

The durability for both electrocatalysts was evaluated by applying a constant potential of 1.6 V (vs. RHE) for 5 hours. The OER polarization curves after the 5 hours of test were described as dashed lines in **Figure 42A**. When compared the overpotentials to obtain 10 mA·cm<sup>-2</sup> before and after the durability test (**Figure 42C**), the IrO<sub>2</sub> nanospheres required 352 mV, which increased 5.7 % after the durability test. On the contrary, the overpotential of the commercial IrO<sub>2</sub> was raised by 9.2 % from 390 mV to 426 mV. For better understanding of kinetic behaviors of the electrocatalysts,

Tafel plots were analyzed from the OER polarization curves before and after the durability test (**Figure 42D**). The IrO<sub>2</sub> nanospheres indicated 57.8 mV·dec<sup>-1</sup> of the Tafel slope in the beginning that is a generally reported value for iridium materials (~ 60 mV·dec<sup>-1</sup>), meaning that the OER here is mainly determined by the step for the conversion to the 'activated hydroxyl group (-OH)'.<sup>155</sup> After the durability test, the Tafel slope barely changed (55.6 mV·dec<sup>-1</sup>). In contrast, the commercial IrO<sub>2</sub> showed a higher initial Tafel slope of 66.3 mV·dec<sup>-1</sup> than IrO<sub>2</sub> nanospheres, and it was increased to 77.9 mV·dec<sup>-1</sup> after 5 hours. It should be pointed out that the commercial IrO<sub>2</sub> showed very unstable plots before it entered the kinetically controlled region (< 1.55 V), which suggests that the measurement conditions for the durability test affected the stability of commercial IrO<sub>2</sub>. It is guessed that the result is highly related to the morphological vulnerability of commercial IrO<sub>2</sub>, since it is favorable to particle aggregation and ripening.<sup>182,183</sup> To investigate the morphology of IrO<sub>2</sub> nanospheres after the durability test, they were observed by HAADF-STEM (**Figure 44**).



**Figure 44.** (A, B) High-resolution HAADF-STEM images of IrO<sub>2</sub> nanospheres after the



durability test, and (C) elemental mapping by EDX.

**Figure 44** presented that the IrO<sub>2</sub> nanospheres were disassembled into small nanoparticles, rather than agglomerated to larger particles. It may be occurred because the ligand or covalent bonds connecting between the small iridium oxide nanoparticles were electrochemically decomposed during the measurement and it could be correlated to the disassembly of IrO<sub>2</sub> nanospheres. Electrochemical potential leads to structural changes and destruction in various ways such as a detachment of particles from structures, selective dissolution, re-coarsening, and more.<sup>184,185</sup> Those degradations in catalyst structures can be connected to the loss of active surface area.<sup>186</sup> When considering the Tafel slopes and morphology of electrocatalysts after the test, the degradation observed in OER activity for IrO<sub>2</sub> nanospheres here is interpreted as the loss of catalysts material on the electrode during measurements, not the weakened catalytic activity of electrocatalyst itself.

#### 3.2.4. Summary

In this study, highly uniform IrO<sub>2</sub> nanospheres were synthesized as electrocatalysts using MnO<sub>2</sub> as a sacrificial template and cation exchange reaction. Utilizing the already prepared template, the synthesis was more well-controlled. During the reaction, the MnO<sub>2</sub> underwent a transformation in its properties such as morphology and phase, which enabled and induced the cation exchange with iridium. The uniform IrO<sub>2</sub> nanospheres were achieved as the well-organized nanostructures assembled by 2 nm size of numerous small iridium oxide nanoparticles with high crystallinity. Through the surface characterization, it was confirmed that the IrO<sub>2</sub> nanospheres possess more hydroxyl groups (78.0 %) on the surface than commercial IrO<sub>2</sub> (34.6 %), which was generated during the synthesis. The IrO<sub>2</sub> nanospheres were evaluated as electrocatalysts for OER under acidic conditions and presented threefold improved mass activity at 1.51 V (58 A·g<sub>Ir</sub><sup>-1</sup>) compared to commercial IrO<sub>2</sub> (20 A·g<sub>Ir</sub><sup>-1</sup>). Besides, it showed 3.5 % enhanced stability after the test that applied 1.6 V for 5 hours to evaluate its durability. Based on the comparison study between the synthesized IrO<sub>2</sub> nanospheres and commercial IrO<sub>2</sub>, it is interpreted that the improved electrocatalytic

performance of IrO<sub>2</sub> nanospheres originated from the structural advantages, that is, morphological uniformity and high hydroxide content on the surface. With this well-designed nanostructure based on only iridium, it was proved that the structuring and increased uniformity for electrocatalysts is important in the improvement of electrocatalytic performance. Moreover, this study presented that the cleverly constructed synthesis plan enables more efficient fabrication procedure of nanostructures by obtaining the preferable surface property without additional treatment, which provided a good guidance and strategy to the following research.

### 3.3. Ir-Ni hollow aerogel<sup>187</sup>

#### 3.3.1. Synthesis of Ir-Ni hollow aerogel

The Ir-Ni aerogel was synthesized by wet chemistry. 0.05 M of  $\text{H}_2\text{IrCl}_6$  (7.5 ml) and  $\text{NiCl}_2$  (2.5 ml) were added in 900 ml of DI water. After enough stirring, 50 mmol of  $\text{NaBH}_4$  that dissolved in 100 ml of DI water was rapidly added under stirring. After 2 min, the solution was closed and stayed for approximately 2 days at ambient temperature. The synthesized Ir-Ni aerogel was washed in DI water several times and dried under vacuum conditions.

#### 3.3.2. Structure characterization

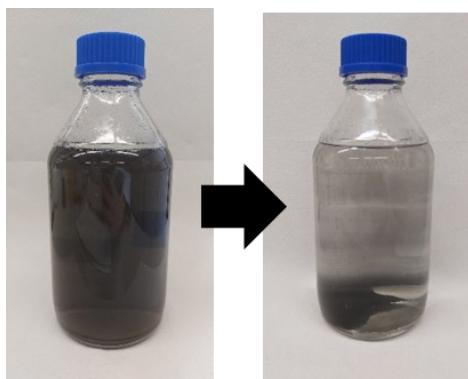
The Ir-Ni aerogel was synthesized by simple wet chemistry. Each precursor solution was added in DI water and stirred until a homogeneous solution was achieved. After that, an aqueous solution dissolving  $\text{NaBH}_4$  operating as a reducing agent was rapidly added into the solution with vigorous stirring.



**Figure 45.** The color change of solution for 15 seconds from the moment that the reducing agent ( $\text{NaBH}_4$ ) was added.

**Figure 45** shows how the color of solution was changed for the first 15 seconds from the moment that the reducing agent was added. In the beginning, the solution presented the brownish color due to the higher ratio of iridium precursor ( $\text{H}_2\text{IrCl}_6$ ),

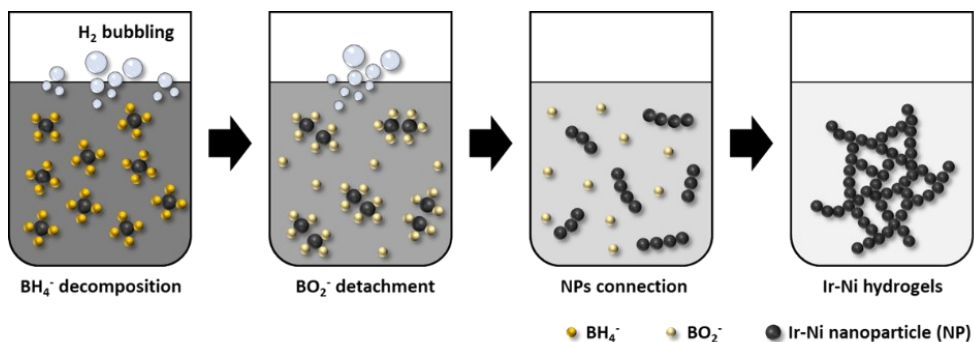
however, with the addition of reducing agent, the color was changed dramatically from orange to yellow, light green, grey, and dark grey in the end. At the same time, it accompanies a vigorous bubbling. The solution was stirred for few minutes additionally and stayed at ambient temperature with being capped. When the reaction is being completed as time goes by, the dark solution becomes transparent with some product sank on the bottom, which will be the Ir-Ni aerogel. **Figure 46** shows that the solution in the beginning of reaction was altered to a transparent solution after approximately two days.



**Figure 46.** The change in transparency of the reaction solution after two days.

To explain the mechanism of the fabrication for Ir-Ni aerogel, schematic illustration was described in **Figure 47**. In the beginning of the reaction, the metal salts in the solution are reduced in a short time with the enough amount of  $\text{NaBH}_4$  that is 100 times of total precursors. The reduced Ir-Ni nanoparticles that are presented as dark black color in the solution are suspended with cations ( $\text{Na}^+$ ) and anions ( $\text{BH}_4^-$ ) from the overly provided reducing agent. The  $\text{BH}_4^-$  ions attaching on the surface of Ir-Ni nanoparticles decompose to  $\text{BO}_2^-$  with the generation of  $\text{H}_2$  bubbling in the solution. Since the  $\text{BO}_2^-$  has lower affinity than  $\text{BH}_4^-$  with metallic surface, it is easily detached from the surface of nanoparticles, which exposes the surface of Ir-Ni nanoparticles.<sup>188</sup> Through the detachment of  $\text{BO}_2^-$  and  $\text{H}_2$  bubbling, enough collisions can occur among

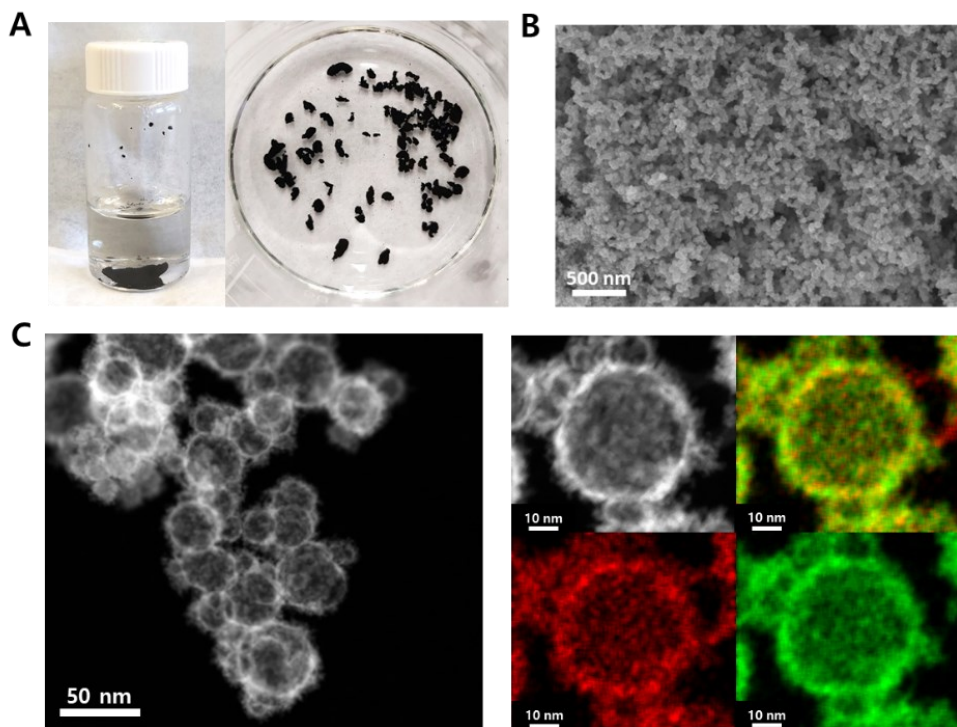
the nanoparticles, which induces them to be connected each other and form 3D structures via high surface energy and van der Waals force. As a result, the suspended nanoparticles are collected and subsided on the bottom as time goes on, which is confirmed as the transparency of solution. Interestingly, the formed structure was sustainable even after breaking of the connection. The settled Ir-Ni aerogel was destroyed instantly with a vigorous shaking, yet it was re-constructed via their surface interaction.



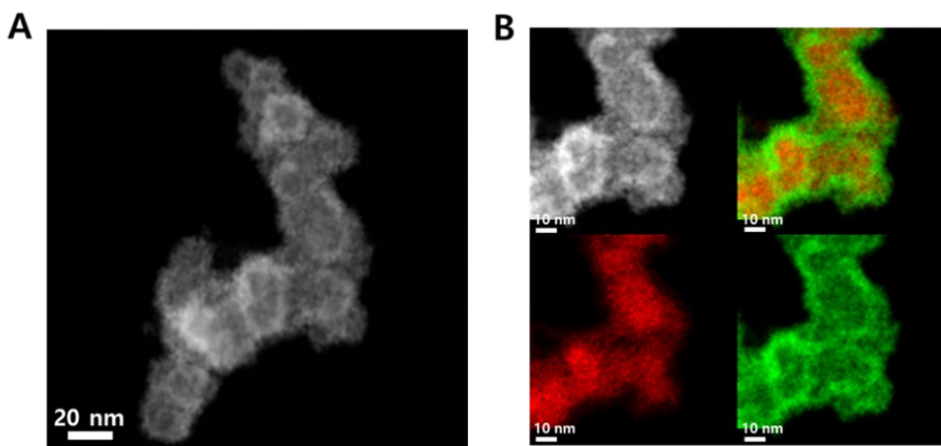
**Figure 47.** Schematic illustration describing the mechanism for the fabrication of Ir-Ni aerogel.

**Figure 48A** shows the synthesized Ir-Ni aerogel after washing. Its final morphology was easily changeable as the methods for sample management, but in most cases, it can be achieved as the bulk owing to the characteristic for self-assembly. The Ir-Ni aerogel was observed overall by SEM, and as shown in **Figure 48B**, it presents a highly well-connected structure of nanoparticles and the size of nanoparticles is less than 30 nm on average. The morphology of Ir-Ni aerogel was observed in detail by HAADF-STEM (**Figure 48C**), which confirms the well-connected Ir-Ni aerogel again. Interestingly, it was observed that the aerogel is composed of hollow Ir-Ni nanoparticles, even though there was no treatment for leaching out. This ‘*in-situ* leaching out effect’ can be explained with the Kirkendall effect. As explained in the previous study, iridium is barely formed themselves first, but coated onto the area

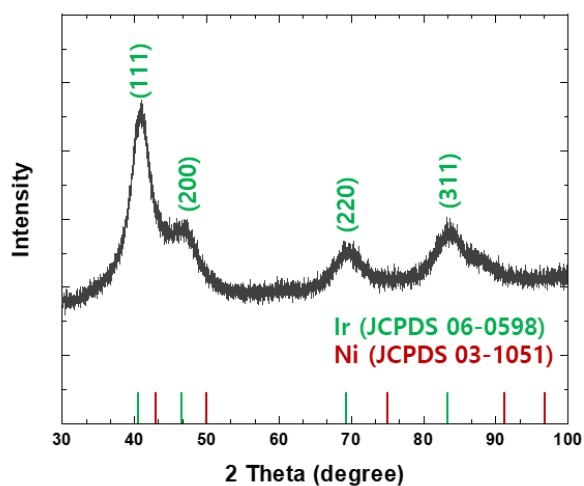
having high surface energy.<sup>146</sup> Besides, considering the kinetics between the two elements iridium and nickel, when iridium and nickel react together, it is spontaneous that nickel forms core part first and the formation of iridium shell is followed, which was reported by Wang et al. via DFT calculation.<sup>189</sup> The formation of core-shell nanostructure for aerogel was observed in a different experimental condition that boosted the speed of reactions induced by heating at 100 °C (**Figure 49**). In this condition, nickel formed core structure quickly due to the fast reduction rate and the coating of iridium on the nickel surface was followed, which synthesized core-shell aerogels consisting of nickel core (red) and iridium shell (green). However, in the synthesis condition for Ir-Ni aerogel here with a slower reaction rate, the nickel was directly leached during the synthesis with the enough reaction time due to the acidic environment made by the iridium precursor, and with the vacancies that the leached nickel made, iridium and nickel formed well-alloyed hollow nanoparticles. From the corresponding elemental mapping by EDX, it was observed that Ir-Ni hollow nanoparticles consist of 60 at% of iridium and 40 at% of nickel, which is also confirmed by ICP-MS.



**Figure 48.** Morphological observation of Ir-Ni aerogel. (A) Photos after synthesis, (B) SEM image, and (C) HAADF-STEM image with elemental mapping for iridium (green) and nickel (red) by EDX.



**Figure 49.** (A) High-resolution HAADF-STEM image of Ir-Ni aerogel with core-shell structure and (B) elemental mapping by EDX for iridium (green) and nickel (red) in a different reaction condition with a faster reaction rate.



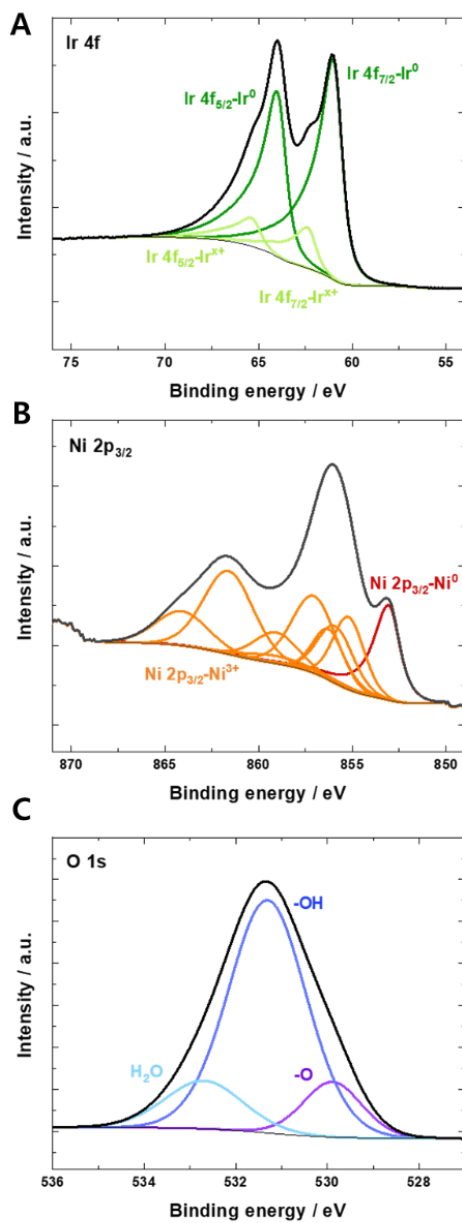
**Figure 50.** XRD pattern of Ir-Ni aerogel.

The crystallinity of Ir-Ni aerogel was studied by XRD (**Figure 50**). It presents the



significant peaks identical to (111), (200), (220), and (311) planes implying the typical FCC structure of metallic iridium (JCPDS 06-0598). The pattern also explains the bimetallic composition with nickel by presenting the broadened peaks. The peak around  $45^\circ$  that especially observed as a shoulder-like peak indicates the presence of a strong nickel (111) peak (JCPDS 03-1051), mentioned often in the alloyed materials of iridium and nickel.<sup>146,190</sup>

To determine the chemical and oxidation state of the surface for Ir-Ni aerogel, XPS was analyzed (**Figure 51**). **Figure 51A** shows the iridium species in the Ir 4f region, indicating that the surface of Ir-Ni aerogel possesses metallic iridium species with 85.0 at% and oxidized iridium ( $\text{Ir}^{x+}$ ) with 15.0 at% on the surface. It is interpreted that the sensitive metallic surface was already slightly oxidized in the ambient experimental environment when considered the confirmed metallic iridium property from the XRD results. The XPS spectra of Ir-Ni aerogel in Ni  $2p_{3/2}$  region showed highly oxidized nickel as  $\text{Ni}^{3+}$  with 80.7 at% and  $\text{Ni}^0$  of metallic species with 19.3 at%, which suggests that the nickel has a metallic core and an oxidized shell considered as  $\gamma\text{-NiOOH}$  (**Figure 51B**).<sup>191,192</sup> It implies that the nickel on the Ir-Ni aerogel surface has mostly oxidized surface mixed with oxide and hydroxyl group. **Figure 51C** shows the O 1s region describing peaks for oxide (-O), hydroxide (-OH), and adventitious spectra which is normally related to adsorbed water ( $\text{H}_2\text{O}$ ) with the portion of 12.9 at%, 72.2 at%, and 14.9 at%, respectively. In the case of oxide peak, both of iridium and nickel contribute to it. It is speculated that the hydroxide spectra are also affected by more than one factor, considering that the  $\gamma\text{-NiOOH}$  possesses a lower intensity for hydroxide species than that for oxide species,<sup>191,193</sup> and it is explained that the leached nickel during the synthesis may also contribute to the hydroxide species, as hydroxyl group can be generated on the surface when nickel is leached from the structure. Overall, the Ir-Ni aerogel surface consists of metallic iridium and oxidized nickel which is the majority of nickel oxyhydroxide.



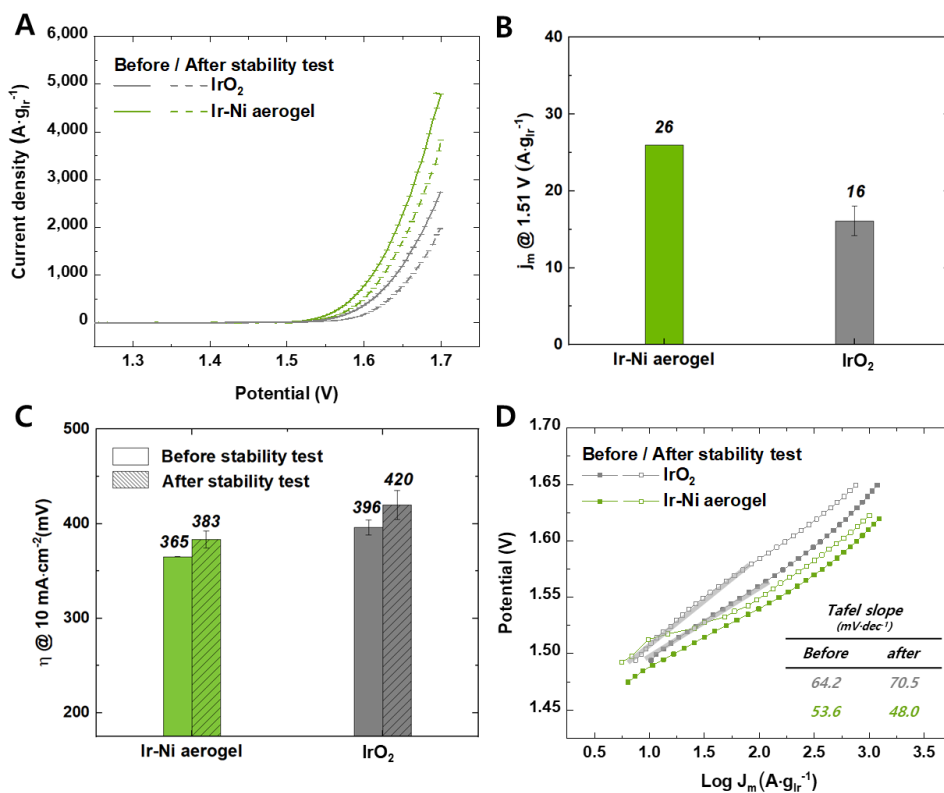
**Figure 51.** X-ray photoelectron spectra of Ir-Ni aerogel in the (A) Ir 4f, (B) Ni 2p<sub>3/2</sub>, (C) O 1s regions.

### 3.3.3. Electrochemical measurements

The Ir-Ni aerogel was evaluated as an electrocatalyst for OER in acidic media with a three-electrode system using RDE. Prior to evaluating the electrocatalytic performance, the ECSA was determined for Ir-Ni aerogel in comparison with commercial IrO<sub>2</sub>. The total anodic charge of a CV after double layer corrected was applied to measure ECSA in the potential range of 0.4 V to 1.25 V (vs. RHE) using a conversion factor of 440  $\mu\text{C}\cdot\text{cm}^{-2}$  after proper CV cycling to achieve the stabilized oxidized surface.<sup>169</sup> The determined ECSA values for commercial IrO<sub>2</sub> was 20.4  $\text{m}^2\cdot\text{g}^{-1}$ , on the contrary, Ir-Ni aerogel presented 15.5  $\text{m}^2\cdot\text{g}^{-1}$  that is much lower than expected from the observed morphology. To compare with the ECSA result, Brunauer-Emmett-Teller (BET) was also analyzed, and from the N<sub>2</sub> adsorption / desorption measurements, the surface area was determined as  $28.9 \pm 1.2 \text{ m}^2\cdot\text{g}^{-1}$  that is doubled value of ECSA. This kind of discrepancy between methods to measure surface area can occur for many reasons, since not any one method perfectly reflects the real surface area for electrocatalytic reactions. It is speculated that the lower value of Ir-Ni aerogel here is caused by the lack of access to the inside of the porous structure between particles with the current ECSA evaluation method and the bulk-scaled physical BET measurement. The assumption that the electrocatalysts have flat surface for the current ECSA calculation could also affect. Furthermore, it is still uncertain that the calculation can be applied to bimetallic or multimetallic composition. As proved by other literature showing unclear aspects for the surface area determination, it is still challenging to achieve reliable result for iridium-based catalysts.<sup>150,151,194</sup>

To evaluate the electrocatalytic activity, the catalyst coated electrode was potentially swept for activation between 0.4 V and 1.4 V (vs. RHE) with a scan rate of 500  $\text{mV}\cdot\text{s}^{-1}$  for 45 cycles first, followed by CV in the same load range, but with a lower scan rate (50  $\text{mV}\cdot\text{s}^{-1}$ ) to observe the redox peaks. After the CV sweeping, the OER activity was evaluated by LSV from 0.4 V to 1.7 V (vs. RHE) with a scan rate of 5  $\text{mV}\cdot\text{s}^{-1}$  in oxygen saturated electrolyte. **Figure 52A** shows the initial OER polarization curves for Ir-Ni aerogel and the commercial IrO<sub>2</sub>, presenting that the Ir-Ni aerogel showed superior activity with 7.8 % lower overpotential than commercial IrO<sub>2</sub>. The

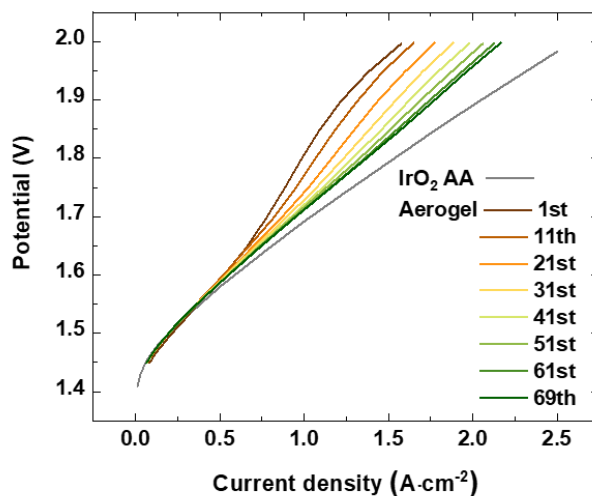
iridium mass activities at 1.51 V for each electrocatalyst were indicated in **Figure 52B**. As an aging test to evaluate the stability of electrocatalysts, the materials were cycled from 1.1 V to 1.6 V at 100 mV·s<sup>-1</sup> for 1,000 times. In a result, the overpotential for the Ir-Ni aerogel was increased 4.9 %; however, the commercial IrO<sub>2</sub> showed relatively higher degradation with 6.1 % (**Figure 52C**).



**Figure 52.** Electrochemical measurements of Ir-Ni aerogel by comparison with commercial IrO<sub>2</sub> (Alfa Aesar). (A) OER polarization curves measured in 0.5 M H<sub>2</sub>SO<sub>4</sub> before and after stability test; (B) Ir mass activities at 1.51 V (vs. RHE); (C) bar graphs displaying the overpotentials to drive 10 mA·cm<sup>-2</sup> and (D) Tafel plots before and after the stability test.

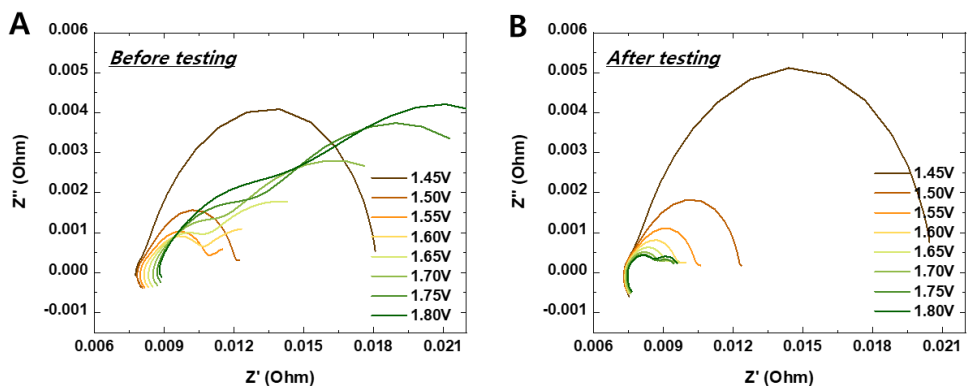
To figure out kinetic behaviors of the electrocatalysts, the Tafel slopes were analyzed from their OER polarization curves (**Figure 52D**). Before the stability test, the Ir-Ni aerogel revealed  $53.6 \text{ mV}\cdot\text{dec}^{-1}$  of Tafel slope, meaning that the rate-determining step for OER is mostly focused on the formation of chemically active hydroxyl group on the electrocatalyst surface.<sup>155</sup> After the durability test, it showed even a lower slope than before the stability test as  $48.0 \text{ mV}\cdot\text{dec}^{-1}$ . It is interpreted that nickel in the structure is electrochemically leached out during the test, which facilitated the formation of active hydroxyl group. Meanwhile, the commercial IrO<sub>2</sub> that started with  $64.2 \text{ mV}\cdot\text{dec}^{-1}$  showed increased Tafel slope after the stability test as  $70.5 \text{ mV}\cdot\text{dec}^{-1}$ , which is attributed to the morphological degradation of IrO<sub>2</sub>, since the irregular shapes of commercial IrO<sub>2</sub> easily goes through the particle agglomeration and coarsening during the cycling.<sup>176,182,183</sup>

The electrochemical performance of Ir-Ni aerogel was evaluated in single cell polarization tests by comparison with the commercial IrO<sub>2</sub>. The details for the fabrication of membrane electrode assembly (MEA) and single cell were explained in the chapter **Electrochemical measurements**. To initiate the single cell testing, each cell was started with activation step, followed by 10 times of forward / backward scanning and HFR analysis. During the scanning, interestingly, it was observed that the polarization curves for Ir-Ni aerogel show the increasing current density as the cycles proceeded. To study further, the forward and backward scanning were continued until the polarization curve is stabilized. **Figure 53** shows the increase in the current density of Ir-Ni aerogel during cycling and the comparison with commercial IrO<sub>2</sub> that normally achieved. As shown in graph, it started with lower current density in the beginning, which is around  $1.58 \text{ A}\cdot\text{cm}^{-2}$ . However, as cycles proceeded, the current density is improved until 50 cycles, which seemed stabilized at around  $2.2 \text{ A}\cdot\text{cm}^{-2}$  after 70 cycles. When considered that the typical cells show degradation during testing<sup>182,194</sup>, this result was interpreted as the effect from the electrochemically leached nickel, working as further activation of electrode by generating more surface area and more hydroxyl group on the catalyst surface. Moreover, there was a subtle kink in slopes around 1.75 V that observed until 20 cycles, which was also speculated as a change in the reaction caused by the electrochemically leached nickel. As the cycles progressed, it slowly faded away.



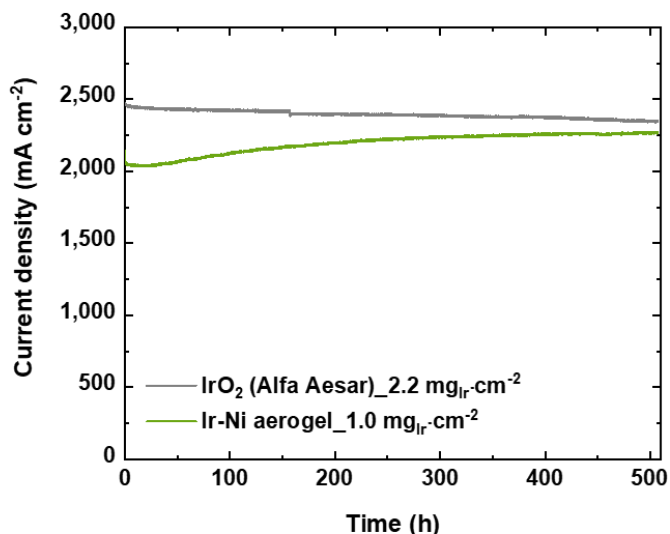
**Figure 53.** Single cell testing of Ir-Ni aerogel with continuous scanning for 70 cycles with  $1.0 \text{ mg}\cdot\text{cm}^{-2}$  of loading by comparison with commercial  $\text{IrO}_2$  ( $1.1 \text{ mg}\cdot\text{cm}^{-2}$ ).

EIS measurements were carried out to study the characteristics of their behaviors. It was implemented before and after testing by screening from 1.45 V to 2.0 V continuously. **Figure 54** shows the Nyquist plots plotting from 1.45 V to 1.80 V with every 0.05V before and after testing. In general, the HFR was decreased after testing, for example, from  $0.2 \text{ }\Omega\cdot\text{cm}^2$  to  $0.18 \text{ }\Omega\cdot\text{cm}^2$  at 1.6 V, meaning that the ohmic resistance for the reaction decreased during the testing. Moreover, it achieved better reaction kinetics with the decreased charge transfer resistance after testing than before. Meanwhile, the cell before testing showed abstruse curves when high potentials were applied, which are not common to be observed in the measurements for iridium catalysts.<sup>58,144,195,196</sup> It seems that some additional unexpected reaction related with nickel happened at the double-layer on the surface, but it disappeared after cycling.



**Figure 54.** Nyquist plots recorded from 1.45 V to 1.80 V for every 0.05 V for the single cell (A) before and (B) after testing.

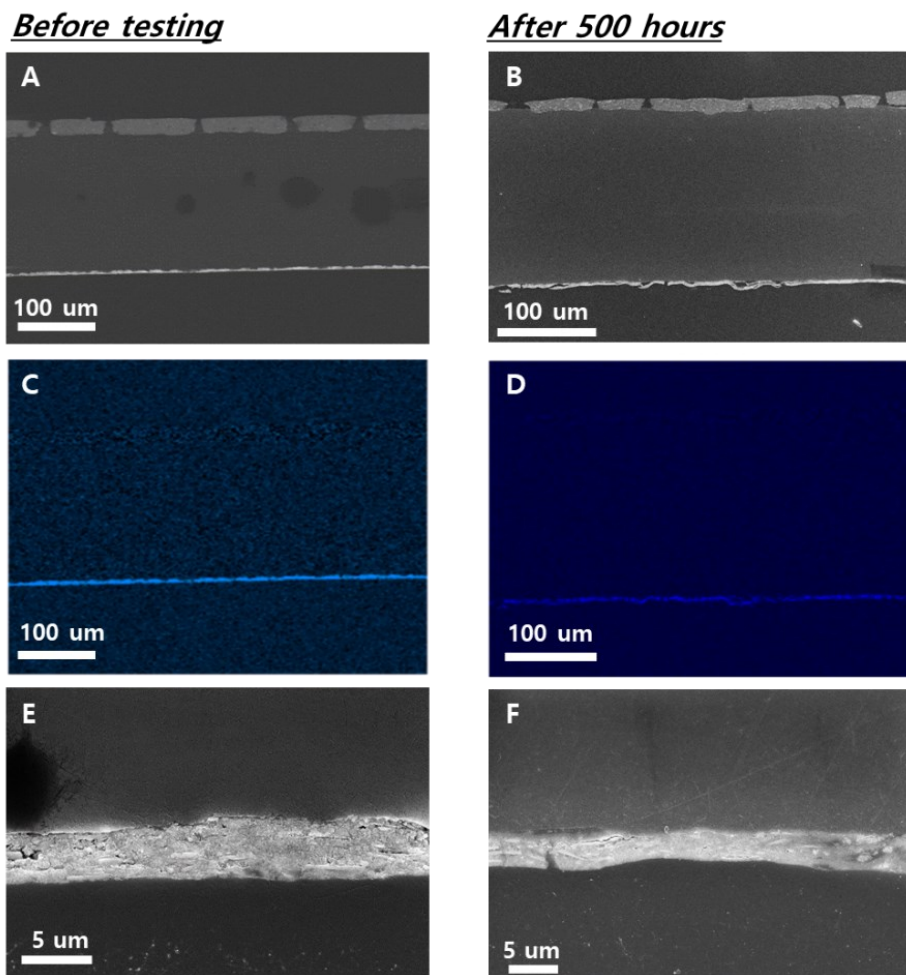
To evaluate the stability of Ir-Ni aerogel, a long-term test was implemented by applying a constant potential of 2.0 V for 500 hours. A  $1.0 \text{ mg}\cdot\text{cm}^{-2}$  iridium loading of electrode was prepared, and it was compared with the result for commercial  $\text{IrO}_2$  electrode with  $2.2 \text{ mg}\cdot\text{cm}^{-2}$  of iridium loading. **Figure 55** indicates the current densities of single cells for Ir-Ni aerogel and commercial  $\text{IrO}_2$  for 500 hours. During the test, the commercial  $\text{IrO}_2$  initially presented the current density over  $2.46 \text{ A}\cdot\text{cm}^{-2}$ , but it was degraded till  $2.35 \text{ A}\cdot\text{cm}^{-2}$  as time goes by, which is usually observed from the typical single cell.<sup>182,194,195</sup> In contrast, the Ir-Ni aerogel showed  $2.07 \text{ A}\cdot\text{cm}^{-2}$  in the beginning, but it continuously increased and reached  $2.27 \text{ A}\cdot\text{cm}^{-2}$  when the time passed 500 hours. Besides, from the polarization curves achieved after the 500 hours of stability test, it was confirmed that the ‘activation’ of Ir-Ni aerogel kept continued, so the activity was improved further and recorded  $2.31 \text{ A}\cdot\text{cm}^{-2}$ . This explains that the long-term stability test worked as an evolving process for the Ir-Ni aerogel, not the deteriorating condition for other catalysts. It is also pointed out that the Ir-Ni aerogel implemented the comparable performance to the state-of-the-art  $\text{IrO}_2$  electrocatalyst for OER even with the lower loading ( $1.0 \text{ mg}\cdot\text{cm}^{-2}$ ), which can bring the cost reduction effect for PEM water electrolyzer.<sup>182,197</sup>



**Figure 55.** The current density of Ir-Ni aerogel during the long-term stability test by applying 2.0 V for 500 hours.

To find out what changes the electrocatalysts underwent during the long-term stability test, the MEA before and after testing were analyzed by various measurements. The morphological changes were observed by measuring the cross-section of the MEA (**Figure 56**). Comparison of the cross-section shows that the coated cathode and anode layers detached slightly from the membrane after the test (**Figure 56A, B**), suggesting that the layers were damaged when the cell was disassembled or affected during the sample preparation for the SEM measurement. However, the electrode layers themselves showed stabilized layer quality with no wrinkled area after the test. From the enlarged images highlighted with blue color, it was again evident that the anode side was hardly destroyed and the coated layer sustained well after the test (**Figure 56C-F**). Meanwhile, it seems that the thicknesses of the electrodes decreased, which is understandable considering that the electrodes were subjected to the 1.6 kN·cm<sup>-2</sup> of high pressure with the metal plate during the fabrication of MEA and the single cell.

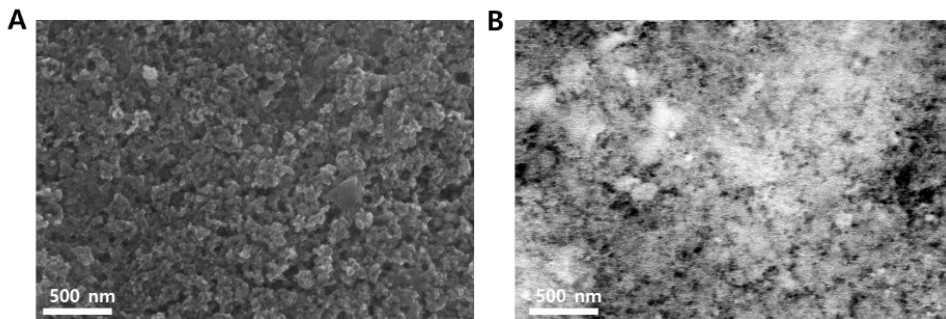




**Figure 56.** (A, B) Cross section observation for MEA before and after testing and (C, D) the corresponding elemental mapping for iridium marked as blue color. (E, F) Enlarged anode side.

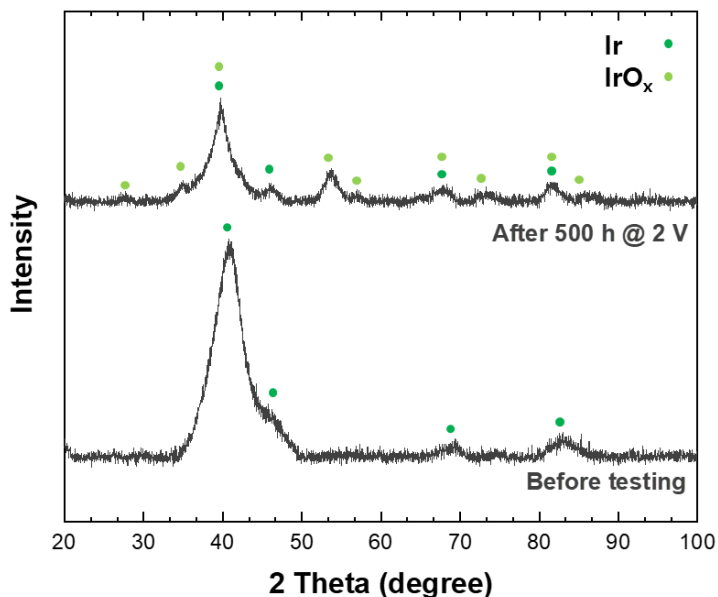
**Figure 57** shows the surface morphology of the anode side after testing. Even after the long-term test, it rarely showed an agglomerated particle but maintained the aerogel structure well. From the backscattered image, the porous structure was also highly sustained (**Figure 57B**). However, it was confirmed that only 4 at% of nickel

was remained by EDX, indicating that the rest of nickel was leached out during the electrochemical measurements.



**Figure 57.** (A) Surface morphology of anode side after testing and (B) the corresponding backscattered image.

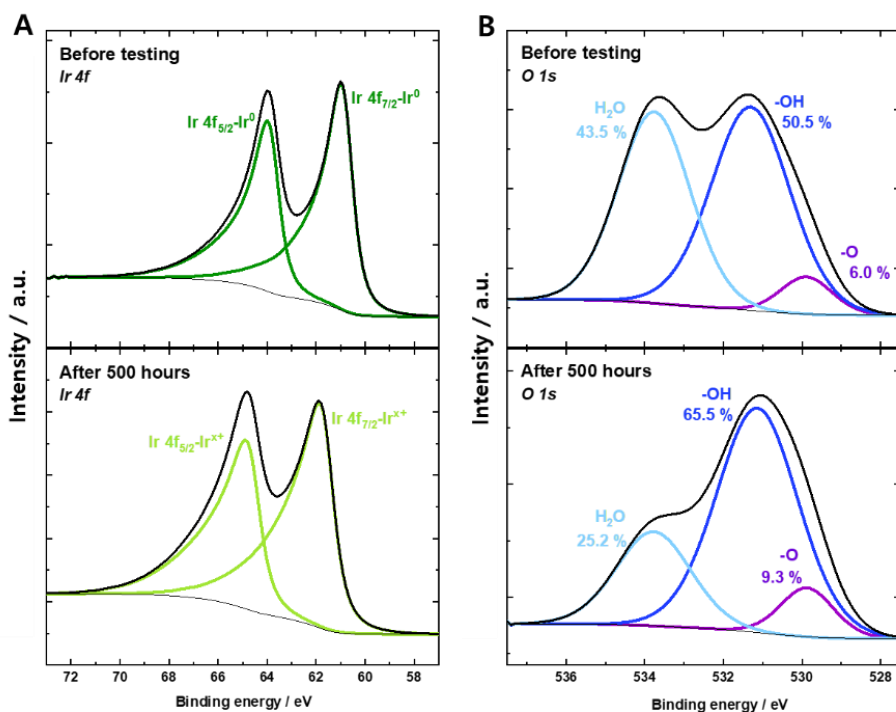
XRD measurement was performed for the anode side before and after the long-term test. (**Figure 58**). Before testing, it showed the XRD peaks fit to the pattern (JCPDS 06-0598) for metallic iridium FCC structure. The peak at  $45^\circ$  appeared as a broad shoulder, which is easily observed from bimetallic materials composed of iridium and nickel due to the nickel having a strong peak near there. After the long-term test, the anode showed a clear change that the intensity of peaks for metallic iridium were decreased overall and the peaks suspected as oxidized iridium were appeared.<sup>198–200</sup> It implies that the oxidation of iridium in Ir-Ni aerogel is considerably proceeded.



**Figure 58.** XRD measurements for the anode side before and after testing.

To determine the changes in chemical and oxidation states of the anode before and after testing, XPS analysis was performed (**Figure 59**). Unfortunately, the specific nickel spectra could not be achieved due to the strong intensity of fluoride peak included in Nafion that is nearly posited with nickel.<sup>201</sup> **Figure 59A** presents the iridium spectra in Ir 4f region before and after testing, which clearly shows that the iridium on the surface was oxidized during testing. Before testing, the anode side possessed only metallic iridium species located at 60.9 and 63.9 eV. However, it was entirely converted to the oxidized iridium spectra possessing 61.9 and 64.9 eV of binding energies, which is easily anticipated when considering the XRD results above. The O 1s region also presented remarkable changes in species. Before testing, it possessed a small portion for oxide spectra (-O) of 6.0 at%, relatively high amount of hydroxide spectra (-OH), and adventitious spectra that will be adsorbed water with 43.5 %. However, after testing it was observed that both of oxide and hydroxide spectra were increased to 9.3 %, 65.5 %, respectively. Moreover, a shift of the hydroxide peak was also observed,

which is speculated as a result of leached nickel during the electrochemical measurements. When considered that most of the nickel was leached from the anode, it is interpreted that the oxide spectra originate from the oxidized iridium and the hydroxide spectra are related to the generated hydroxyl group from the leached nickel, explaining the improved electrocatalytic performance during the long-term test.



**Figure 59.** XPS spectra for the anode before and after testing in (A) Ir 4f region and (B) O 1s region.

### 3.3.4. Summary

In this study, Ir-Ni aerogel was synthesized as an electrocatalyst for oxygen evolution reaction. It consists of bimetallic hollow nanoparticles uniformly alloyed with iridium and nickel, which was induced by the reaction rate control, called the *in-situ* leaching out effect here. Thanks to the facile and simple synthesis procedure, the increased yield was also obtained. When tested in a three-electrode system, the Ir-Ni aerogel exhibits higher electrocatalytic performance than the commercial IrO<sub>2</sub>. However, when it was applied in single cells to figure out its performance in the real condition, the Ir-Ni aerogel showed the interesting result that the performance kept increasing as the measurements proceeded. In the long-term stability test for 500 hours, it showed 2.07 A·cm<sup>-2</sup> in the beginning but remarked 2.31 A·cm<sup>-2</sup> after the long-term test, which is comparable to the commercial IrO<sub>2</sub> showing 2.35 A·cm<sup>-2</sup> under degradation. This enhancement in the electrocatalytic performance for Ir-Ni aerogel is attributed to the nickel gradually leached out from the aerogel structure that generates more surface area and hydroxyl group on the catalyst surface. It should be also pointed out that the iridium loading of Ir-Ni aerogel electrode was much lower as 1.0 mg·cm<sup>-2</sup> than the tested commercial IrO<sub>2</sub> electrode (2.2 mg·cm<sup>-2</sup>), which suggests that the Ir-Ni aerogel has a potential to bring the cost down for PEM water electrolyzer for the same performance. From the characterization of MEA after the single cell test, it was confirmed that the morphology of aerogel structure was preserved well without any coarsening or agglomeration that is easily observed from the disordered and irregular nanoparticles, which is associated with the improved electrocatalytic stability. To sum up, this Ir-Ni aerogel study shows that well-designed synthesis plan enables a facile and efficient synthesis, and bimetallic electrocatalysts alloyed with transition metals have a possibility to be applied in real cells by substituting the commercial IrO<sub>2</sub> with a reduced iridium loading.

## 4. Conclusions

In this study, three types of novel nanostructures were synthesized and evaluated as electrocatalysts for OER in PEM water electrolysis. The nanostructures aimed to achieve superior activity and stability to the commercial IrO<sub>2</sub>, which was approached from a material structure point of view. In the design of catalyst structure, 3d transition metals (nickel or manganese here) were mainly utilized. The synthesized nanostructures were physically and chemically characterized as electrocatalysts. Each structure was electrochemically evaluated for OER in comparison with commercial iridium catalysts, and the performance was studied and discussed in relation to the structural properties.

The bimetallic NiIr hollow nanoframes were delicately fabricated with a controlled reaction time. The design of this structure was built from the pristine core-shell NiIr hexagonal nanostructures consisting of 97 at% of nickel and 3 at% of iridium, which planned the shaped iridium-based hollow nanostructures by selective etching of nickel. The etching process was efficient to remove the nickel core part and induce the well-alloyed bimetallic composition by Kirkendall effect. The achieved NiIr hollow nanoframe (72 at% iridium and 28 at% nickel) maximized the utilization of iridium with the 3D hollow nanostructures, as well as acquired more electrocatalytically active surface via the removal of nickel, supported by the increased hydroxyl group (71.4 % → 83.2 %) on the catalyst surface. In the electrochemical measurements compared with the commercial iridium particles, the NiIr hollow nanoframes showed 269 mV of overpotential and 887 A·g<sub>Ir</sub><sup>-1</sup> of iridium mass activity at 1.51 V, which is 29-fold improved. In addition, the bimetallic composition with small amounts of nickel less than 3 at% resulted in the structural robustness of the frame-shaped nanostructures that sustained 1,000 cycles of durability test. This study proved that a well-designed structure of the electrocatalyst can improve the electrocatalytic activity and stability at the same time. Accordingly, it is required to put the efforts to realize the production for this kind of delicate nanostructures beyond the lab-scale.

The uniform IrO<sub>2</sub> nanospheres were synthesized using a sacrificial template by cation exchange reaction. The already prepared template material contributed to the more facile synthesis process. MnO<sub>2</sub> was used as a sacrificed template for the

electrocatalyst; it excluded the possibly dissolved transition metal from the electrocatalysts during measurement by exchanging manganese entirely with iridium. Nonetheless, the participation of manganese dioxide in the reaction was absolutely necessary, since iridium barely showed any specific structure in the synthesis condition without it. The finally obtained IrO<sub>2</sub> nanospheres show uniform morphology in size distribution and spherical shape, as well as the higher portion of hydroxyl groups (78.0 %) on the catalyst surface compared to the commercial IrO<sub>2</sub> (38.6 %), which was achieved during the exchange reaction. The IrO<sub>2</sub> nanospheres present three times boosted electrocatalytic activity than commercial IrO<sub>2</sub>, which is explained as the effect from the uniform morphology and favorable surface property to the reaction with the increased hydroxyl group. Through these IrO<sub>2</sub> nanospheres, the fundamental importance of structures for materials was highlighted. It was also suggested that a well-established synthesis can avoid an unnecessary post-treatment process to achieve desired catalyst structures.

The Ir-Ni aerogel was designed to achieve the advantages of bimetallic nanostructures, but also to overcome the limited yield in the lab-scale. It was prepared by a simple sol-gel process, which completed bimetallic hollow nanostructures with the hierarchical morphology by controlling the reaction rate without additional treatment. The Ir-Ni aerogel possessing metallic surface property was applied to the single cells, which showed an interesting result that the electrocatalytic activity continuously improving throughout the measurements, and after 500 hours of stability test it had almost the same activity of 2.31 A·cm<sup>-2</sup> with commercial IrO<sub>2</sub>, while the commercial IrO<sub>2</sub> degraded from 2.46 A·cm<sup>-2</sup> to 2.35 A·cm<sup>-2</sup>, even when the iridium loading for Ir-Ni aerogel electrode was lower as 1.0 mg·cm<sup>-2</sup> than that for commercial IrO<sub>2</sub> electrode (2.2 mg·cm<sup>-2</sup>). This is mainly attributed to the electrochemically leached nickel from the aerogel structure during the measurements that will induce a more active catalytic surface and expose more surface area as hollow nanostructures. The well-preserved original morphology after testing was also beneficial to the improving catalytic activity. With the Ir-Ni aerogel, it was confirmed that the bimetallic hollow nanostructures have a potential to substitute the commercial IrO<sub>2</sub>. Moreover, it also enabled to observe and understand the behavior of bimetallic iridium-based electrocatalysts with 3d transition metals in single cells. Accordingly, it is considered

that the Ir-Ni aerogel structure has a worth to be investigated and modified further.

In summary, three different structured electrocatalysts were synthesized, characterized, and evaluated for OER. Each nanostructure showed its advantages and limitations as electrocatalysts but proved that electrocatalytic performance can be improved by efficient structuring of electrocatalysts in the end. To significantly reduce iridium consumption, the use of transition metals seems to be inevitable and highly recommended, as it allows the preparation of more diverse iridium materials and increases the electrocatalytic performance. However, it also brings some side effects, such as an increase in resistivity due to the unavoidable dissolution under the acidic working conditions. Therefore, attentive and prudent use is required. Well-designed synthesis plans can be helpful to reduce the risk and make the fabrication process easier. Although much research has been and is being done in the field of catalyst nanostructures, the investigation of catalyst materials to be used on a large scale seems to be still insufficient. More realistic research should be done, not only developing catalyst structures but also considering the possibility of implementation in real cells.



## 5. References

1. The National Hydrogen Strategy. (2020).
2. In focus: Hydrogen – driving the green revolution | European Commission. [https://ec.europa.eu/info/news/focus-hydrogen-driving-green-revolution-2021-abr-14\\_en](https://ec.europa.eu/info/news/focus-hydrogen-driving-green-revolution-2021-abr-14_en).
3. Renewable Energy - Our World in Data. <https://ourworldindata.org/renewable-energy>.
4. Infographic: Low Renewable Costs Allow To Power Past Coal. </newsroom/articles/2021/Jun/Low-Renewable-Costs-Allow-To-Power-Past-Coal>.
5. Finance & Investment. <https://www.irena.org/financeinvestment>.
6. Renewable Power – Analysis - IEA. <https://www.iea.org/reports/renewable-power>.
7. Rain or shine: Germany’s renewable energy production defies fickle weather. <https://www.handelsblatt.com/english/politics/rain-or-shine-germanys-renewable-energy-production-defies-fickle-weather/23583028.html?ticket=ST-45443-GLSNcl7vjCzE39ZjA5jH-ap4>.
8. Renewable Energy Challenges. <https://esrl.noaa.gov/gsd/renewable/challenges.html>.
9. Declining Renewable Costs Drive Focus on Energy Storage | News | NREL. <https://www.nrel.gov/news/features/2020/declining-renewable-costs-drive-focus-on-energy-storage.html>.
10. Energy storage is key for incorporating renewables into EU grid, new study suggests | European Commission. [https://ec.europa.eu/info/news/energy-storage-key-incorporating-renewables-eu-grid-new-study-suggests-2020-may-11\\_en](https://ec.europa.eu/info/news/energy-storage-key-incorporating-renewables-eu-grid-new-study-suggests-2020-may-11_en).
11. International Renewable Energy Agency, T. *RENEWABLE POWER-TO-HYDROGEN INNOVATION LANDSCAPE BRIEF*. (2019).
12. *A sustainable pathway for the global energy transition*. [www.hydrogencouncil.com](http://www.hydrogencouncil.com).
13. Heat values of various fuels - World Nuclear Association. <https://world->

- nuclear.org/information-library/facts-and-figures/heat-values-of-various-fuels.aspx.
14. *Hydrogen decarbonization pathways A life-cycle assessment*. www.hydrogencouncil.com. (2021).
  15. Koch Blank, T. & Molly, P. *Hydrogen's Decarbonization Impact for Industry Near-term challenges and long-term potential*. www.rmi.org (2020).
  16. Energy Agency, I. The Future of Hydrogen.
  17. Guo, Y., Li, G., Zhou, J. & Liu, Y. Comparison between hydrogen production by alkaline water electrolysis and hydrogen production by PEM electrolysis. *IOP Conf. Ser. Earth Environ. Sci.* **371**, 042022 (2019).
  18. Kuckshinrichs, W., Ketelaer, T. & Koj, J. C. Economic analysis of improved alkaline water electrolysis. *Front. Energy Res.* **5**, 1 (2017).
  19. Brauns, J. & Turek, T. Alkaline Water Electrolysis Powered by Renewable Energy: A Review. *Process.* 2020, Vol. 8, Page 248 **8**, 248 (2020).
  20. Carmo, M., Fritz, D. L., Mergel, J. & Stolten, D. A comprehensive review on PEM water electrolysis. *Int. J. Hydrogen Energy* **38**, 4901–4934 (2013).
  21. Zhou, Z., Nadimpalli, V. K., Pedersen, D. B. & Esposito, V. Degradation Mechanisms of Metal-Supported Solid Oxide Cells and Countermeasures: A Review. *Mater.* 2021, Vol. 14, Page 3139 **14**, 3139 (2021).
  22. Sohal, M. S. *et al.* Degradation issues in solid oxide cells during high temperature electrolysis. *J. Fuel Cell Sci. Technol.* **9**, (2012).
  23. Mayyas, A., Ruth, M., Pivovar, B., Bender, G. & Wipke, K. Manufacturing Cost Analysis for Proton Exchange Membrane Water Electrolyzers. (2019).
  24. Shiva Kumar, S. & Himabindu, V. Hydrogen production by PEM water electrolysis – A review. *Mater. Sci. Energy Technol.* **2**, 442–454 (2019).
  25. Markets single - MINING.COM.  
<https://www.mining.com/markets/commodity/iridium/>.
  26. Kim, J. *et al.* Theoretical and Experimental Understanding of Hydrogen Evolution Reaction Kinetics in Alkaline Electrolytes with Pt-Based Core-Shell Nanocrystals. *J. Am. Chem. Soc.* **141**, 18256–18263 (2019).
  27. Dubouis, N. & Grimaud, A. The hydrogen evolution reaction: from material to interfacial descriptors. *Chem. Sci.* **10**, 9165–9181 (2019).

28. Mahmood, J. *et al.* An efficient and pH-universal ruthenium-based catalyst for the hydrogen evolution reaction. *Nat. Nanotechnol.* 2017 125 **12**, 441–446 (2017).
29. Nørskov, J. K. *et al.* Trends in the Exchange Current for Hydrogen Evolution. *J. Electrochem. Soc.* **152**, J23 (2005).
30. Halck, N. B., Petrykin, V., Krtil, P. & Rossmeisl, J. Beyond the volcano limitations in electrocatalysis – oxygen evolution reaction. *Phys. Chem. Chem. Phys.* **16**, 13682–13688 (2014).
31. Reier, T., Nong, H. N., Teschner, D., Schlögl, R. & Strasser, P. Electrocatalytic Oxygen Evolution Reaction in Acidic Environments – Reaction Mechanisms and Catalysts. (2016) doi:10.1002/aenm.201601275.
32. Fabbri, E. & Schmidt, T. J. Oxygen Evolution Reaction The Enigma in Water Electrolysis. (2018) doi:10.1021/acscatal.8b02712.
33. Bockris, J. O. M. Kinetics of Activation Controlled Consecutive Electrochemical Reactions: Anodic Evolution of Oxygen. *J. Chem. Phys.* **24**, 817 (2004).
34. Castelli, P., Trasatti, S., Pollak, F. H. & O’Grady, W. E. Single crystals as model electrocatalysts. Oxygen evolution on RuO<sub>2</sub> (110). *J. Electroanal. Chem.* **210**, 189–194 (1986).
35. Rossmeisl, J., Qu, Z. W., Zhu, H., Kroes, G. J. & Nørskov, J. K. Electrolysis of water on oxide surfaces. *J. Electroanal. Chem.* **607**, 83–89 (2007).
36. Pham, C. Van, Escalera-López, D., Mayrhofer, K., Cherevko, S. & Thiele, S. Essentials of High Performance Water Electrolyzers – From Catalyst Layer Materials to Electrode Engineering. *Adv. Energy Mater.* **11**, (2021).
37. McCrory, C. C. L. *et al.* Benchmarking Hydrogen Evolving Reaction and Oxygen Evolving Reaction Electrocatalysts for Solar Water Splitting Devices. *J. Am. Chem. Soc.* **137**, 4347–4357 (2015).
38. Trasatti, S. Electrocatalysis in the anodic evolution of oxygen and chlorine. *Electrochim. Acta* **29**, 1503–1512 (1984).
39. Shan, J. *et al.* Charge-Redistribution-Enhanced Nanocrystalline Ru@IrO<sub>x</sub> Electrocatalysts for Oxygen Evolution in Acidic Media. *Chem* **5**, 445–459 (2019).
40. Lee, Y., Suntivich, J., May, K. J., Perry, E. E. & Shao-Horn, Y. Synthesis and

- Activities of Rutile IrO<sub>2</sub> and RuO<sub>2</sub> Nanoparticles for Oxygen Evolution in Acid and Alkaline Solutions. *J. Phys. Chem. Lett.* **3**, 399–404 (2012).
41. Stoerzinger, K. A., Qiao, L., Biegalski, M. D. & Shao-Horn, Y. Orientation-dependent oxygen evolution activities of rutile IrO<sub>2</sub> and RuO<sub>2</sub>. *J. Phys. Chem. Lett.* **5**, 1636–1641 (2014).
  42. Rossmeisl, J., Logadottir, A. & Nørskov, J. K. Electrolysis of water on (oxidized) metal surfaces. *Chem. Phys.* **319**, 178–184 (2005).
  43. Li, G., Li, S., Ge, J., Liu, C. & Xing, W. Discontinuously covered IrO<sub>2</sub>-RuO<sub>2</sub>@Ru electrocatalysts for the oxygen evolution reaction: How high activity and long-term durability can be simultaneously realized in the synergistic and hybrid nano-structure. *J. Mater. Chem. A* **5**, 17221–17229 (2017).
  44. Hodnik, N. *et al.* New Insights into Corrosion of Ruthenium and Ruthenium Oxide Nanoparticles in Acidic Media. *J. Phys. Chem. C* **119**, 10140–10147 (2015).
  45. Cherevko, S. *et al.* Oxygen and hydrogen evolution reactions on Ru, RuO<sub>2</sub>, Ir, and IrO<sub>2</sub> thin film electrodes in acidic and alkaline electrolytes: A comparative study on activity and stability. *Catal. Today* **262**, 170–180 (2016).
  46. Wang, Z., Guo, X., Montoya, J. & Nørskov, J. K. Predicting aqueous stability of solid with computed Pourbaix diagram using SCAN functional. *npj Comput. Mater.* **2020 61 6**, 1–7 (2020).
  47. Schulz, K., Seal, R., Bradley, D. & Deyoung, J. Critical mineral resources of the United States—Economic and environmental geology and prospects for future supply. *Prof. Pap.* (2017) doi:10.3133/PP1802.
  48. sheryl singerling, B. & schulte, ruth F. Platinum-Group metals-2018 [aDVanCe release] Platinum-Group Metals. (1AD).
  49. Minke, C., Suermann, M., Bensmann, B. & Hanke-Rauschenbach, R. Is iridium demand a potential bottleneck in the realization of large-scale PEM water electrolysis? *Int. J. Hydrogen Energy* **46**, 23581–23590 (2021).
  50. Babic, U., Suermann, M., Büchi, F. N., Gubler, L. & Schmidt, T. J. Review-Identifying Critical Gaps for Polymer Electrolyte Water Electrolysis Development. *J. Electrochem. Soc.* **164**, F387–F399 (2017).
  51. Bernt, M. *et al.* Current Challenges in Catalyst Development for PEM Water

- Electrolyzers. *Chemie Ing. Tech.* **92**, 31–39 (2020).
52. Fu, L., Yang, F., Cheng, G. & Luo, W. Ultrathin Ir nanowires as high-performance electrocatalysts for efficient water splitting in acidic media. *Nanoscale* **10**, 1892–1897 (2018).
  53. Li, G. *et al.* Nanoporous IrO<sub>2</sub> catalyst with enhanced activity and durability for water oxidation owing to its micro/mesoporous structure. *Nanoscale* **9**, 9291–9298 (2017).
  54. Wang, C. *et al.* Synthesis of Cu–Ir nanocages with enhanced electrocatalytic activity for the oxygen evolution reaction. *J. Mater. Chem. A* **3**, 19669–19673 (2015).
  55. Liu, M. *et al.* Facile synthesis of Pd–Ir bimetallic octapods and nanocages through galvanic replacement and co-reduction, and their use for hydrazine decomposition. *Phys. Chem. Chem. Phys.* **15**, 11822 (2013).
  56. Kwon, T. *et al.* Cobalt Assisted Synthesis of IrCu Hollow Octahedral Nanocages as Highly Active Electrocatalysts toward Oxygen Evolution Reaction. *Adv. Funct. Mater.* **27**, 1604688 (2017).
  57. Pei, J. *et al.* Ir–Cu nanoframes: one-pot synthesis and efficient electrocatalysts for oxygen evolution reaction. *Chem. Commun.* **52**, 3793–3796 (2016).
  58. Li, G. *et al.* Boosted Performance of Ir Species by Employing TiN as the Support toward Oxygen Evolution Reaction. *ACS Appl. Mater. Interfaces* **10**, 38117–38124 (2018).
  59. Hartig-Weiss, A. *et al.* Iridium Oxide Catalyst Supported on Antimony-Doped Tin Oxide for High Oxygen Evolution Reaction Activity in Acidic Media. *ACS Appl. Nano Mater.* (2020) doi:10.1021/acsnm.9b02230.
  60. Lebedev, D. & Copéret, C. Small, Narrowly Distributed Iridium Nanoparticles Supported on Indium Tin Oxide for Efficient Anodic Water Oxidation. *ACS Appl. Energy Mater.* **2**, 196–200 (2019).
  61. Antolini, E. & Gonzalez, E. R. Ceramic materials as supports for low-temperature fuel cell catalysts. *Solid State Ionics* **180**, 746–763 (2009).
  62. Rabis, A., Rodriguez, P. & Schmidt, T. J. Electrocatalysis for polymer electrolyte fuel cells: Recent achievements and future challenges. *ACS Catalysis* vol. 2 864–890 (2012).

63. Macauley, N. *et al.* Carbon Corrosion in PEM Fuel Cells and the Development of Accelerated Stress Tests. *J. Electrochem. Soc.* **165**, F3148–F3160 (2018).
64. Ede, S. R. & Luo, Z. Tuning the intrinsic catalytic activities of oxygen-evolution catalysts by doping: a comprehensive review. *J. Mater. Chem. A* **9**, 20131–20163 (2021).
65. Back, S., Yeom, M. S. & Jung, Y. Active Sites of Au and Ag Nanoparticle Catalysts for CO<sub>2</sub> Electroreduction to CO. (2015)  
doi:10.1021/acscatal.5b00462.
66. Lee, W. H. *et al.* Carbon-Supported IrCoO<sub>x</sub> nanoparticles as an efficient and stable OER electrocatalyst for practicable CO<sub>2</sub> electrolysis. (2020)  
doi:10.1016/j.apcatb.2020.118820.
67. Fu, S., Zhu, C., Du, D. & Lin, Y. Enhanced Electrocatalytic Activities of PtCuCoNi Three-Dimensional Nanoporous Quaternary Alloys for Oxygen Reduction and Methanol Oxidation Reactions. *ACS Appl. Mater. Interfaces* **8**, 6110–6116 (2016).
68. Zhao, Y. *et al.* Understanding the Effect of Monomeric Iridium(III/IV) Aquo Complexes on the Photoelectrochemistry of IrO<sub>x</sub>-n H<sub>2</sub>O-Catalyzed Water-Splitting Systems. *J. Am. Chem. Soc.* **137**, 8749–8757 (2015).
69. Kwon, T. *et al.* Vertex-Reinforced PtCuCo Ternary Nanoframes as Efficient and Stable Electrocatalysts for the Oxygen Reduction Reaction and the Methanol Oxidation Reaction. *Adv. Funct. Mater.* **28**, 1706440 (2018).
70. Seh, Z. W. *et al.* Combining theory and experiment in electrocatalysis: Insights into materials design. *Science (80-. )*. **355**, eaad4998 (2017).
71. Zhao, M. *et al.* Hollow Metal Nanocrystals with Ultrathin, Porous Walls and Well-Controlled Surface Structures. *Adv. Mater.* **30**, 1801956 (2018).
72. Zhao, M. *et al.* Ru Octahedral Nanocrystals with a Face-Centered Cubic Structure, {111} Facets, Thermal Stability up to 400 °C, and Enhanced Catalytic Activity. *J. Am. Chem. Soc.* **141**, 7028–7036 (2019).
73. Xia, Y. & Yang, X. Toward Cost-Effective and Sustainable Use of Precious Metals in Heterogeneous Catalysts. *Acc. Chem. Res.* **50**, 450–454 (2017).
74. Wang, X. *et al.* Pt-Based Icosahedral Nanocages: Using a Combination of {111} Facets, Twin Defects, and Ultrathin Walls to Greatly Enhance Their

- Activity toward Oxygen Reduction. *Nano Lett.* **16**, 1467–1471 (2016).
75. Zhang, L. *et al.* Platinum-based nanocages with subnanometer-thick walls and well-defined, controllable facets. *Science (80-. )*. **349**, 412–416 (2015).
  76. Park, J. *et al.* Iridium-Based Multimetallic Nanoframe@Nanoframe Structure: An Efficient and Robust Electrocatalyst toward Oxygen Evolution Reaction. *ACS Nano* **11**, 5500–5509 (2017).
  77. Strasser, P. *et al.* Lattice-strain control of the activity in dealloyed core–shell fuel cell catalysts. *Nat. Chem.* **2010 26 2**, 454–460 (2010).
  78. Dubau, L. *et al.* Defects do Catalysis: CO Monolayer Oxidation and Oxygen Reduction Reaction on Hollow PtNi/C Nanoparticles. *ACS Catal.* **6**, 4673–4684 (2016).
  79. Chattot, R. *et al.* Beyond strain and ligand effects: Microstrain-induced enhancement of the oxygen reduction reaction kinetics on various PtNi/C nanostructures. *ACS Catal.* **7**, 398–408 (2017).
  80. Bu, L. *et al.* Biaxially strained PtPb/Pt core/shell nanoplate boosts oxygen reduction catalysis. *Science (80-. )*. **354**, 1410–1414 (2016).
  81. Pi, Y., Shao, Q., Zhu, X. & Huang, X. Dynamic Structure Evolution of Composition Segregated Iridium-Nickel Rhombic Dodecahedra toward Efficient Oxygen Evolution Electrocatalysis. *ACS Nano* **12**, 7371–7379 (2018).
  82. Park, J. *et al.* Hemi-core@frame AuCu@IrNi nanocrystals as active and durable bifunctional catalysts for the water splitting reaction in acidic media. *Nanoscale Horizons* **4**, 727–734 (2019).
  83. Feng, J. *et al.* Iridium-Based Multimetallic Porous Hollow Nanocrystals for Efficient Overall-Water-Splitting Catalysis. *Adv. Mater.* **29**, 1703798 (2017).
  84. Sun, X. *et al.* Gold-Based Cubic Nanoboxes with Well-Defined Openings at the Corners and Ultrathin Walls Less Than Two Nanometers Thick. *ACS Nano* **10**, 8019–8025 (2016).
  85. Shviro, M., Polani, S. & Zitoun, D. Hollow octahedral and cuboctahedral nanocrystals of ternary Pt-Ni-Au alloys. *Nanoscale* **7**, 13521–13529 (2015).
  86. Feng, Y. *et al.* Construction of hierarchical FeP/Ni<sub>2</sub>P hollow nanospindles for efficient oxygen evolution. *J. Mater. Chem. A* **6**, 14103–14111 (2018).
  87. Fu, S. *et al.* Three-dimensional PtNi hollow nanochains as an enhanced

- electrocatalyst for the oxygen reduction reaction †. (2016)  
doi:10.1039/c6ta01801g.
88. Chee, S. W. *et al.* Interface-mediated Kirkendall effect and nanoscale void migration in bimetallic nanoparticles during interdiffusion. *Nat. Commun.* **10**, 1–8 (2019).
  89. Bang, S. *et al.* Formation of double layer hollow nanostars of Pd/CuIr by utilizing a Kirkendall effect and a facile Cu atom movement along twinning boundaries and their usage as efficient water splitting catalysts. *CrystEngComm* **17**, 4084–4088 (2015).
  90. Han, L. *et al.* Alloy Cu<sub>3</sub>Pt nanoframes through the structure evolution in Cu-Pt nanoparticles with a core-shell construction. *Sci. Reports* **4**, 1–6 (2014).
  91. Wang, J. X. *et al.* Kirkendall effect and lattice contraction in nanocatalysts: A new strategy to enhance sustainable activity. *J. Am. Chem. Soc.* **133**, 13551–13557 (2011).
  92. Zhang, C. *et al.* Component-Controlled Synthesis of Necklace-Like Hollow NiXRu Nanoalloys as Electrocatalysts for Hydrogen Evolution Reaction. *ACS Appl. Mater. Interfaces* **9**, 17326–17336 (2017).
  93. Yoon, D. *et al.* Cactus-Like Hollow Cu<sub>2</sub>-xS@Ru Nanoplates as Excellent and Robust Electrocatalysts for the Alkaline Hydrogen Evolution Reaction. *Small* **13**, 1700052 (2017).
  94. Oh, M. H. *et al.* Galvanic replacement reactions in metal oxide nanocrystals. *Science* (80-. ). **340**, 964–968 (2013).
  95. Da Silva, A. G. M., Rodrigues, T. S., Haigh, S. J. & Camargo, P. H. C. Galvanic replacement reaction: Recent developments for engineering metal nanostructures towards catalytic applications. *Chemical Communications* vol. 53 7135–7148 (2017).
  96. Bratsch, S. G. Standard Electrode Potentials and Temperature Coefficients in Water at 298.15 K. *J. Phys. Chem. Ref. Data* **18**, 1–21 (1989).
  97. Sun, Y. & Xia, Y. Mechanistic Study on the Replacement Reaction between Silver Nanostructures and Chloroauric Acid in Aqueous Medium. *J. Am. Chem. Soc.* **126**, 3892–3901 (2004).



98. Rodrigues, T. S. *et al.* Hollow AgPt/SiO<sub>2</sub> nanomaterials with controlled surface morphologies: is the number of Pt surface atoms imperative to optimize catalytic performances? *Catal. Sci. Technol.* **6**, 2162–2170 (2016).
99. Au, L., Lu, X. & Xia, Y. A Comparative Study of Galvanic Replacement Reactions Involving Ag Nanocubes and AuCl<sub>2</sub><sup>-</sup> or AuCl<sub>4</sub><sup>-</sup>. *Adv. Mater.* **20**, 2517–2522 (2008).
100. Slater, T. J. A. *et al.* Correlating catalytic activity of Ag-Au nanoparticles with 3D compositional variations. *Nano Lett.* **14**, 1921–1926 (2014).
101. Hong, J. W. *et al.* Controlled Synthesis of Pd–Pt Alloy Hollow Nanostructures with Enhanced Catalytic Activities for Oxygen Reduction. *ACS Nano* **6**, 2410–2419 (2012).
102. Han, L., Wang, P., Liu, H., Tan, Q. & Yang, J. Balancing the galvanic replacement and reduction kinetics for the general formation of bimetallic CuM (M = Ru, Rh, Pd, Os, Ir, and Pt) hollow nanostructures. *J. Mater. Chem. A* **4**, 18354–18365 (2016).
103. Da Silva, A. G. M. *et al.* Controlling Size, Morphology, and Surface Composition of AgAu Nanodendrites in 15 s for Improved Environmental Catalysis under Low Metal Loadings. *ACS Appl. Mater. Interfaces* **7**, 25624–25632 (2015).
104. Rodrigues, T. S. *et al.* Probing the catalytic activity of bimetallic versus trimetallic nanoshells. *J. Mater. Sci.* 2015 5016 **50**, 5620–5629 (2015).
105. Wang, C. *et al.* Synthesis of Ni–Ir Nanocages with Improved Electrocatalytic Performance for the Oxygen Evolution Reaction. *ACS Sustain. Chem. Eng.* **5**, 9787–9792 (2017).
106. Zhang, H., Jin, M., Xiong, Y., Lim, B. & Xia, Y. Shape-controlled synthesis of Pd nanocrystals and their catalytic applications. *Acc. Chem. Res.* **46**, 1783–1794 (2013).
107. Wang, X. *et al.* Pt-Based Icosahedral Nanocages: Using a Combination of {111} Facets, Twin Defects, and Ultrathin Walls to Greatly Enhance Their Activity toward Oxygen Reduction. (2016) doi:10.1021/acs.nanolett.5b05140.
108. Zhao, M. *et al.* Synthesis and Characterization of Ru Cubic Nanocages with a Face-Centered Cubic Structure by Templating with Pd Nanocubes. *Nano Lett.*

- 16**, 5310–5317 (2016).
109. Xie, S. *et al.* Synthesis of Pd-Rh core-frame concave nanocubes and their conversion to Rh cubic nanoframes by selective etching of the Pd cores. *Angew. Chemie - Int. Ed.* **51**, 10266–10270 (2012).
  110. Yang, T. H., Shi, Y., Janssen, A. & Xia, Y. Surface Capping Agents and Their Roles in Shape-Controlled Synthesis of Colloidal Metal Nanocrystals. *Angew. Chemie Int. Ed.* **59**, 15378–15401 (2020).
  111. Huang, R., Wen, Y. H., Zhu, Z. Z. & Sun, S. G. Atomic-scale insights into structural and thermodynamic stability of Pd-Ni bimetallic nanoparticles. *Phys. Chem. Chem. Phys.* **18**, 9847–9854 (2016).
  112. Han, L., Wang, P., Liu, H., Tan, Q. & Yang, J. Balancing the galvanic replacement and reduction kinetics for the general formation of bimetallic CuM (M = Ru, Rh, Pd, Os, Ir, and Pt) hollow nanostructures. *J. Mater. Chem. A* **4**, 18354–18365 (2016).
  113. Nosheen, F., Anwar, T., Siddique, A. & Hussain, N. Noble metal based alloy nanoframes: Syntheses and applications in fuel cells. *Frontiers in Chemistry* vol. 7 (2019).
  114. Park, J. *et al.* Radially Phase Segregated PtCu@PtCuNi Dendrite@Frame Nanocatalyst for the Oxygen Reduction Reaction. *ACS Nano* **11**, 10844–10851 (2017).
  115. Wang, J. *et al.* Regulating the Catalytically Active Sites in Low-Cost and Earth-Abundant 3d Transition-Metal-Based Electrode Materials for High-Performance Zinc–Air Batteries. *Energy & Fuels* **35**, 6483–6503 (2021).
  116. Feng, Y. *et al.* Earth-abundant 3d-transition-metal catalysts for lignocellulosic biomass conversion. *Chem. Soc. Rev.* **50**, 6042–6093 (2021).
  117. Park, J. *et al.* Hollow nanoparticles as emerging electrocatalysts for renewable energy conversion reactions. *Chem. Soc. Rev.* **47**, 8173–8202 (2018).
  118. Yang, Y. *et al.* Metal Surface and Interface Energy Electrocatalysis: Fundamentals, Performance Engineering, and Opportunities. *Chem* vol. 4 2054–2083 (2018).
  119. Strasser, P., Gliech, M., Kuehl, S. & Moeller, T. Electrochemical processes on solid shaped nanoparticles with defined facets. *Chemical Society Reviews* vol.

- 47 715–735 (2018).
120. Xia, Z. & Guo, S. Strain engineering of metal-based nanomaterials for energy electrocatalysis. *Chem. Soc. Rev.* (2019) doi:10.1039/C8CS00846A.
  121. Lima, F. H. B. *et al.* Catalytic Activity-d-Band Center Correlation for the O<sub>2</sub> Reduction Reaction on Platinum in Alkaline Solutions. (2007) doi:10.1021/jp065181r.
  122. Strasser, P. *et al.* Lattice-strain control of the activity in dealloyed core-shell fuel cell catalysts. (2010) doi:10.1038/NCHEM.623.
  123. Oh, A. *et al.* Skeletal octahedral nanoframe with cartesian coordinates via geometrically precise nanoscale phase segregation in a Pt@Ni core-shell nanocrystal. *ACS Nano* **9**, 2856–2867 (2015).
  124. Kwon, T. *et al.* Vertex-Reinforced PtCuCo Ternary Nanoframes as Efficient and Stable Electrocatalysts for the Oxygen Reduction Reaction and the Methanol Oxidation Reaction. *Adv. Funct. Mater.* **28**, 1706440 (2018).
  125. Beermann, V. *et al.* Rh-Doped Pt-Ni Octahedral Nanoparticles: Understanding the Correlation between Elemental Distribution, Oxygen Reduction Reaction, and Shape Stability. *Nano Lett.* **16**, 1719–1725 (2016).
  126. Kwon, T. *et al.* Dopant-Assisted Control of the Crystallite Domain Size in Hollow Ternary Iridium Alloy Octahedral Nanocages toward the Oxygen Evolution Reaction. *Cell Reports Phys. Sci.* **1**, 100260 (2020).
  127. Lu, H. *et al.* Highly Stable PtPdCu Alloy Nanowire Networks as Oxygen Reduction Electrocatalysts. *Electrocatal.* **2021 124** **12**, 372–380 (2021).
  128. Kwon, T. *et al.* Au-Ru alloy nanofibers as a highly stable and active bifunctional electrocatalyst for acidic water splitting. *Appl. Surf. Sci.* **563**, 150293 (2021).
  129. Wu, Z. P. *et al.* Alloying–realloying enabled high durability for Pt–Pd-3d-transition metal nanoparticle fuel cell catalysts. *Nat. Commun.* **2021 121** **12**, 1–14 (2021).
  130. Huang, X., Zhao, Z., Fan, J., Tan, Y. & Zheng, N. Amine-assisted synthesis of concave polyhedral platinum nanocrystals having {411} high-index facets. *J. Am. Chem. Soc.* **133**, 4718–4721 (2011).
  131. Yu, T., Kim, D. Y., Zhang, H. & Xia, Y. Platinum Concave Nanocubes with

- High-Index Facets and Their Enhanced Activity for Oxygen Reduction Reaction. *Angew. Chemie* **123**, 2825–2829 (2011).
132. Chen, Q., Jia, Y., Xie, S. & Xie, Z. Well-faceted noble-metal nanocrystals with nonconvex polyhedral shapes. *Chemical Society Reviews* vol. 45 3207–3220 (2016).
133. Sheng, T., Tian, N., Zhou, Z. Y., Lin, W. F. & Sun, S. G. Designing Pt-Based Electrocatalysts with High Surface Energy. *ACS Energy Letters* vol. 2 1892–1900 (2017).
134. Sun, S., Zhang, X., Cui, J., Yang, Q. & Liang, S. High-index faceted metal oxide micro-/nanostructures: A review on their characterization, synthesis and applications. *Nanoscale* vol. 11 15739–15762 (2019).
135. Yu, T., Kim, D. Y., Zhang, H. & Xia, Y. Platinum concave nanocubes with high-index facets and their enhanced activity for oxygen reduction reaction. *Angew. Chemie - Int. Ed.* **50**, 2773–2777 (2011).
136. Stamenkovic, V. R. *et al.* Improved oxygen reduction activity on Pt<sub>3</sub>Ni(111) via increased surface site availability. *Science* (80-. ). **315**, 493–497 (2007).
137. Kuzume, A., Herrero, E. & Feliu, J. M. Oxygen reduction on stepped platinum surfaces in acidic media. *J. Electroanal. Chem.* **599**, 333–343 (2007).
138. Marković, N. M. & Ross, P. N. Surface science studies of model fuel cell electrocatalysts. *Surf. Sci. Rep.* **45**, 117–229 (2002).
139. Marković, N. M., Gasteiger, H. A. & Ross, P. N. Oxygen reduction on platinum low-index single-crystal surfaces in alkaline solution: Rotating ring diskPt(hkl) studies. *J. Phys. Chem.* **100**, 6715–6721 (1996).
140. SEM vs TEM | Technology Networks.  
<https://www.technologynetworks.com/analysis/articles/sem-vs-tem-331262>.
141. Kovács, A., Schierholz, R. & Tillmann, K. FEI Titan G2 80-200 CREWLEY. *J. large-scale Res. Facil. JLSRF* **2**, A43 (2016).
142. Wilschefska, S. C. & Baxter, M. R. Inductively Coupled Plasma Mass Spectrometry: Introduction to Analytical Aspects. *Clin. Biochem. Rev.* **40**, 115 (2019).
143. ICP-MS - General Instrumentation. <https://www.ru.nl/science/gi/facilities-activities/elemental-analysis/icp-ms/>.

144. Bizzotto, F. *et al.* Ir nanoparticles with ultrahigh dispersion as oxygen evolution reaction (OER) catalysts: synthesis and activity benchmarking. *Catal. Sci. Technol.* **9**, 6345–6356 (2019).
145. Pham, C. Van *et al.* IrO<sub>2</sub> coated TiO<sub>2</sub> core-shell microparticles advance performance of low loading proton exchange membrane water electrolyzers. *Appl. Catal. B Environ.* **269**, 118762 (2020).
146. Park, S. *et al.* Nickel Structures as a Template Strategy to Create Shaped Iridium Electrocatalysts for Electrochemical Water Splitting. *ACS Appl. Mater. Interfaces* **13**, 13576–13585 (2021).
147. Zalitis, C. M., Kucernak, A. R., Sharman, J. & Wright, E. Design principles for platinum nanoparticles catalysing electrochemical hydrogen evolution and oxidation reactions: Edges are much more active than facets. *J. Mater. Chem. A* **5**, 23328–23338 (2017).
148. Xia, X. *et al.* Facile Synthesis of Iridium Nanocrystals with Well-Controlled Facets Using Seed-Mediated Growth. *J. Am. Chem. Soc.* **136**, 10878–10881 (2014).
149. Abbott, D. F. *et al.* Iridium Oxide for the Oxygen Evolution Reaction: Correlation between Particle Size, Morphology, and the Surface Hydroxyl Layer from Operando XAS. *Chem. Mater.* **28**, 6591–6604 (2016).
150. Alia, S. M., Shulda, S., Ngo, C., Pylypenko, S. & Pivovar, B. S. Iridium-Based Nanowires as Highly Active, Oxygen Evolution Reaction Electrocatalysts. *ACS Catal.* **8**, 2111–2120 (2018).
151. Godínez-Salomón, F. *et al.* Self-Supported Hydrous Iridium–Nickel Oxide Two-Dimensional Nanoframes for High Activity Oxygen Evolution Electrocatalysts. *ACS Catal.* **8**, 10498–10520 (2018).
152. Reier, T. *et al.* Molecular Insight in Structure and Activity of Highly Efficient, Low-Ir Ir–Ni Oxide Catalysts for Electrochemical Water Splitting (OER). *J. Am. Chem. Soc.* **137**, 13031–13040 (2015).
153. Ren, M. *et al.* Lattice contracted Pd-hollow nanocrystals: Synthesis, structure and electrocatalysis for formic acid oxidation. *J. Power Sources* **246**, 32–38 (2014).
154. Huang, K. *et al.* Ultrathin two-dimensional metals with fully exposed (111)

- facets. *Chem. Commun.* **54**, 160–163 (2017).
155. Antolini, E. Iridium As Catalyst and Cocatalyst for Oxygen Evolution/Reduction in Acidic Polymer Electrolyte Membrane Electrolyzers and Fuel Cells. *ACS Catal.* **4**, 1426–1440 (2014).
  156. Sharma, G. *et al.* Novel development of nanoparticles to bimetallic nanoparticles and their composites: A review. *Journal of King Saud University - Science* vol. 31 257–269 (2019).
  157. Loza, K., Heggen, M. & Epple, M. Synthesis, Structure, Properties, and Applications of Bimetallic Nanoparticles of Noble Metals. *Adv. Funct. Mater.* **30**, 1909260 (2020).
  158. Park, S. *et al.* Cation-Exchange Method Enables Uniform Iridium Oxide Nanospheres for Oxygen Evolution Reaction. *ACS Appl. Nano Mater.* **5**, 4062–4071 (2022).
  159. Lentijo-Mozo, S., Deiana, D., Sogne, E., Casu, A. & Falqui, A. Unexpected Insights about Cation-Exchange on Metal Oxide Nanoparticles and Its Effect on Their Magnetic Behavior. *Chem. Mater.* **30**, 8099–8112 (2018).
  160. Luo, Z. *et al.* Mn<sub>3</sub>O<sub>4</sub>@CoMn<sub>2</sub>O<sub>4</sub>-CoxOy Nanoparticles: Partial Cation Exchange Synthesis and Electrocatalytic Properties toward the Oxygen Reduction and Evolution Reactions. *ACS Appl. Mater. Interfaces* **8**, 17435–17444 (2016).
  161. Hua, K. *et al.* Cation-exchange synthesis of manganese vanadate nanosheets and its application in lithium-ion battery. *J. Solid State Chem.* **273**, 287–294 (2019).
  162. Post, J. E. Manganese oxide minerals: Crystal structures and economic and environmental significance. *Proc. Natl. Acad. Sci.* **96**, 3447–3454 (1999).
  163. Fritsch, S. & Navrotsky, A. Thermodynamic Properties of Manganese Oxides. *J. Am. Ceram. Soc.* **79**, 1761–1768 (1996).
  164. Jacob, K. T., Kumar, A., Rajitha, G. & Waseda, Y. Thermodynamic data for Mn<sub>3</sub>O<sub>4</sub>, Mn<sub>2</sub>O<sub>3</sub> and MnO. *High Temp. Mater. Process.* **30**, 459–472 (2011).
  165. Deljoo, B., Tan, H., Suib, S. L. & Aindow, M. Thermally activated structural transformations in manganese oxide nanoparticles under air and argon atmospheres. *J. Mater. Sci.* **55**, 7247–7258 (2020).

166. Rivest, J. B. & Jain, P. K. Cation exchange on the nanoscale: an emerging technique for new material synthesis, device fabrication, and chemical sensing. *Chem. Soc. Rev.* **42**, 89–96 (2012).
167. Holder, C. F. & Schaak, R. E. Tutorial on Powder X-ray Diffraction for Characterizing Nanoscale Materials. *ACS Nano* vol. 13 7359–7365 (2019).
168. Moreau, L. M. *et al.* Defining crystalline/amorphous phases of nanoparticles through X-ray absorption spectroscopy and X-ray diffraction: The case of nickel phosphide. *Chem. Mater.* **25**, 2394–2403 (2013).
169. Tan, X., Shen, J., Semagina, N. & Secanell, M. Decoupling structure-sensitive deactivation mechanisms of Ir/IrO<sub>x</sub> electrocatalysts toward oxygen evolution reaction. *J. Catal.* **371**, 57–70 (2019).
170. Spöri, C., Kwan, J. T. H., Bonakdarpour, A., Wilkinson, D. P. & Strasser, P. The Stability Challenges of Oxygen Evolving Catalysts: Towards a Common Fundamental Understanding and Mitigation of Catalyst Degradation. *Angew. Chemie - Int. Ed.* **56**, 5994–6021 (2017).
171. Kim, Y.-T. *et al.* Balancing activity, stability and conductivity of nanoporous core-shell iridium/iridium oxide oxygen evolution catalysts. *Nat. Commun.* **8**, 1449 (2017).
172. Stevens, D. A. & Dahn, J. R. Electrochemical Characterization of the Active Surface in Carbon-Supported Platinum Electrocatalysts for PEM Fuel Cells. *J. Electrochem. Soc.* **150**, 770–775 (2003).
173. Karimi, F., Bazylak, A. & Peppley, B. A. Effect of Calcination Temperature on the Morphological and Electrochemical Characteristics of Supported Iridium Hydroxyoxide Electrocatalysts for the PEM Electrolyzer Anode. *J. Electrochem. Soc.* **164**, F464–F474 (2017).
174. Ooka, H., Yamaguchi, A., Takashima, T., Hashimoto, K. & Nakamura, R. Efficiency of Oxygen Evolution on Iridium Oxide Determined from the pH Dependence of Charge Accumulation. *J. Phys. Chem. C* **121**, 17873–17881 (2017).
175. Chen, Y. *et al.* Exceptionally active iridium evolved from a pseudo-cubic perovskite for oxygen evolution in acid. *Nat. Commun.* **10**, 1–10 (2019).
176. Rakousky, C., Shviro, M., Carmo, M. & Stolten, D. Iridium nanoparticles for the

- oxygen evolution reaction: Correlation of structure and activity of benchmark catalyst systems. *Electrochim. Acta* **302**, 472–477 (2019).
177. Liu, Y., Zhang, L., Willis, B. G. & Mustain, W. E. Importance of particle size and distribution in achieving high-activity, high-stability oxygen reduction catalysts. *ACS Catal.* **5**, 1560–1567 (2015).
  178. Wu, S. *et al.* Effect of particle size distribution on the electrochemical performance of micro-sized silicon-based negative materials. *RSC Adv.* **8**, 8544–8551 (2018).
  179. Yano, H., Watanabe, M., Iiyama, A. & Uchida, H. Particle-size effect of Pt cathode catalysts on durability in fuel cells. *Nano Energy* **29**, 323–333 (2016).
  180. García, J. R., Bidabehere, C. M. & Sedran, U. Non-uniform size of catalyst particles. Impact on the effectiveness factor and the determination of kinetic parameters. *Chem. Eng. J.* **396**, 124994 (2020).
  181. Trogadas, P. & Fuller, T. F. The Effect of Uniform Particle Size Distribution on Pt Stability. doi:10.1149/1.3635610.
  182. Alia, S. M. *et al.* Activity and Durability of Iridium Nanoparticles in the Oxygen Evolution Reaction. *J. Electrochem. Soc.* **163**, F3105–F3112 (2016).
  183. Oh, H. S. *et al.* Electrochemical Catalyst-Support Effects and Their Stabilizing Role for IrO<sub>x</sub> Nanoparticle Catalysts during the Oxygen Evolution Reaction. *J. Am. Chem. Soc.* **138**, 12552–12563 (2016).
  184. Beermann, V. *et al.* Real-time imaging of activation and degradation of carbon supported octahedral Pt-Ni alloy fuel cell catalysts at the nanoscale using: In situ electrochemical liquid cell STEM. *Energy Environ. Sci.* **12**, 2476–2485 (2019).
  185. Huang, J. *et al.* Potential-induced nanoclustering of metallic catalysts during electrochemical CO<sub>2</sub> reduction. *Nat. Commun.* **9**, (2018).
  186. Urchaga, P. *et al.* Catalyst Degradation in Fuel Cell Electrodes: Accelerated Stress Tests and Model-based Analysis. *Electrochim. Acta* **176**, 1500–1510 (2015).
  187. Park, S., Utsch, N., Carmo, M., Shviro, M. & Stolten, D. Iridium-Nickel Nanoparticle-Based Aerogels for Oxygen Evolution Reaction. *ACS Appl. Nano Mater.* (2022)



- doi:10.1021/ACSANM.2C04000/SUPPL\_FILE/AN2C04000\_SI\_003.MP4.
188. Du, R. *et al.* Unveiling reductant chemistry in fabricating noble metal aerogels for superior oxygen evolution and ethanol oxidation. doi:10.1038/s41467-020-15391-w.
  189. Wang, L. L. & Johnson, D. D. Predicted trends of core-shell preferences for 132 late transition-metal binary-alloy nanoparticles. *J. Am. Chem. Soc.* **131**, 14023–14029 (2009).
  190. Nong, H. N., Gan, L., Willinger, E., Teschner, D. & Strasser, P. IrO<sub>x</sub> core-shell nanocatalysts for cost- and energy-efficient electrochemical water splitting. *Chem. Sci.* **5**, 2955–2963 (2014).
  191. Biesinger, M. C., Payne, B. P., Lau, L. W. M., Gerson, A. & Smart, R. S. C. X-ray photoelectron spectroscopic chemical state quantification of mixed nickel metal, oxide and hydroxide systems. *Surf. Interface Anal.* **41**, 324–332 (2009).
  192. Grosvenor, A. P., Biesinger, M. C., StC Smart, R. & Stewart McIntyre, N. New interpretations of XPS spectra of nickel metal and oxides. (2006) doi:10.1016/j.susc.2006.01.041.
  193. Payne, B. P., Biesinger, M. C. & McIntyre, N. S. The study of polycrystalline nickel metal oxidation by water vapour. *J. Electron Spectros. Relat. Phenomena* **175**, 55–65 (2009).
  194. Hegge, F. *et al.* Efficient and Stable Low Iridium Loaded Anodes for PEM Water Electrolysis Made Possible by Nanofiber Interlayers. *ACS Appl. Energy Mater.* **3**, 8276–8284 (2020).
  195. Audichon, T. *et al.* Electroactivity of RuO<sub>2</sub>-IrO<sub>2</sub> mixed nanocatalysts toward the oxygen evolution reaction in a water electrolyzer supplied by a solar profile. *Int. J. Hydrogen Energy* **39**, 16785–16796 (2014).
  196. Ahmed, J. & Mao, Y. Ultrafine Iridium Oxide Nanorods Synthesized by Molten Salt Method toward Electrocatalytic Oxygen and Hydrogen Evolution Reactions. *Electrochim. Acta* **212**, 686–693 (2016).
  197. Bühler, M. *et al.* Optimization of anodic porous transport electrodes for proton exchange membrane water electrolyzers. *J. Mater. Chem. A* **7**, 26984–26995 (2019).
  198. Pfeifer, V. *et al.* The electronic structure of iridium and its oxides. *Surf.*

- Interface Anal.* **48**, 261–273 (2016).
199. Xu, S., Chen, S., Tian, L., Xia, Q. & Hu, W. Selective-leaching method to fabricate an Ir surface-enriched Ir-Ni oxide electrocatalyst for water oxidation. *J. Solid State Electrochem.* **20**, 1961–1970 (2016).
200. Pfeifer, V. *et al.* The electronic structure of iridium oxide electrodes active in water splitting. *Phys. Chem. Chem. Phys.* **18**, 2292–2296 (2016).
201. Moulder, J. F., Stickle, W. F., Sobol, P. E. ', Bomben, K. D. & Chastain, J. Handbook of X-ray Photoelectron Spectroscopy AReference Book of Standard Spectra for Identification and Interpretation of XPS Data.

## List of Figures

<b>Figure 1.</b> Renewable power generation by technology in the Sustainable Development Scenario, 2000-2030. <sup>6</sup> .....	3
<b>Figure 2.</b> The potential demand for hydrogen by 2050. <sup>12</sup> .....	4
<b>Figure 3.</b> OER mechanisms for acidic conditions (S: the active catalytic surface). .	10
<b>Figure 4.</b> The depiction about Gibbs free energies of the intermediates on O <sup>-*</sup> -covered RuO <sub>2</sub> at three different potentials (U=0, U= 1.23, and U= 1.60 V). <sup>35</sup> .....	13
<b>Figure 5.</b> The overpotentials of various catalysts after short-term stability test at 10 mA·cm <sup>-2</sup> . <sup>37</sup> .....	15
<b>Figure 6.</b> The theoretical activity of the four charge transferring steps of oxygen evolution depicted as function of the oxygen binding energy for (left) oxide surfaces and (right) metal surfaces. <sup>35</sup> .....	16
<b>Figure 7.</b> The current density for OER on Co / Ni modified RuO <sub>2</sub> (left) and volcano curve of the theoretical overpotential for OER based on the DFT calculations (right). <sup>30</sup> .....	18
<b>Figure 8.</b> Calculated Pourbaix diagram for ruthenium (left) and iridium (right). <sup>46</sup> .....	19
<b>Figure 9.</b> Schematic illustration of catalyst development strategies. <sup>70</sup> .....	22
<b>Figure 10.</b> Formation energy of Pd vacancies and a schematic illustrating interface-mediated Kirkendall effect. (A) DFT calculations of the formation energy of a Pd vacancy at different locations of the Au-Pd layered structure. (B) A schematic comparison of the conventional Kirkendall effect and the observations of interfacial void formation and void migration in this study. (Green: Au atoms, Red: Pd atoms) <sup>88</sup> .....	25
<b>Figure 11.</b> Schematic illustration of the formation process for a hollow bilayer Pd/CuIr nanostar. <sup>89</sup> .....	26
<b>Figure 12.</b> Morphology observation of AgPt nanotubes with smooth (B-F) and rough surfaces (G-K). <sup>98</sup> .....	28
<b>Figure 13.</b> Schematic illustration of the fabrication procedure for Rh nanoframe. <sup>109,110</sup> .....	31
<b>Figure 14.</b> The upshift of the d-band center when the atoms are applied by tensile strength. ....	33

<b>Figure 15.</b> (Left) Projected DOS of d-bands of Ir and IrCoNi models with corresponding d-band center as dash lines. (Right) Schematic illustration of reaction paths for OER. <sup>83</sup> .....	34
<b>Figure 16.</b> Reported polyhedral FCC shapes classified by their exposed facets, in case of palladium nanocrystals. <sup>106</sup> .....	37
<b>Figure 17.</b> Influence of the surface morphology and electronic surface properties on the kinetics of ORR. <sup>136</sup> .....	38
<b>Figure 18.</b> Schematic diagram of SEM <sup>140</sup> .....	43
<b>Figure 19.</b> Schematic diagram of TEM <sup>140</sup> .....	45
<b>Figure 20.</b> Schematic diagram of the Bragg's law.....	46
<b>Figure 21.</b> Three-electrode system for RDE measurements. ....	50
<b>Figure 22.</b> Single cell after finishing the assembly. ....	54
<b>Figure 23.</b> Role of the metal precursors. (A, B) Photo when the iridium precursor is reacted alone; (C, D) photo when the nickel precursor is reacted alone and the TEM image of the corresponding product. ....	59
<b>Figure 24.</b> Morphology and composition profile analysis of the pristine NiIr hexagonal nanostructure. (A) HAADF-STEM image; (B) magnified view of the selected green area with high resolution HAADF-STEM and FFT pattern; (C) line scan analysis of NiIr hexagonal nanostructure along the white dash line of inset; and (D-F) the corresponding elemental distribution of nickel and iridium maps. ....	60
<b>Figure 25.</b> Growth study of NiIr nanostructures as the reaction time. High resolution TEM images of the products and magnified views when the reaction time was (A, B) 10 min; (C, D) 30 min; (E, F) 60 min with the FFT patterns (each inset in B, D, F) .....	62
<b>Figure 26.</b> (A) HAADF-STEM image and (B-D) corresponding elemental distribution of nickel (red) and iridium (green) across the EDX composition maps for the reaction products at 60 min. ....	62
<b>Figure 27.</b> Schematic illustration of the formation of the NiIr hollow nanoframe. (A-C) Formation of the NiIr hexagonal nanostructure; (D) the NiIr hollow nanoframe after the leaching out step; and (E) the enlarged description of the edge area during the leaching. ....	63

<b>Figure 28.</b> Morphology and composition profile analysis of the Nilr hollow nanoframes. (A) A high-resolution HAADF-STEM image of Nilr hollow nanoframe and a line scan profile along the white dash line; (B-D) the elemental distribution of iridium (green) and nickel (red) in the EDX. ....	64
<b>Figure 29.</b> XRD patterns of Nilr hexagonal nanostructures (before leaching) and Nilr hollow nanoframes (after leaching). ....	65
<b>Figure 30.</b> XPS result of Nilr hexagonal nanostructures and Nilr hollow nanoframes in the (A) Ir 4f / Ni 3p, (B) Ni 2p <sub>3/2</sub> , and (C) O 1s regions. ....	67
<b>Figure 31.</b> Electrocatalytic performance of the Nilr hollow nanoframes by comparison with commercial Ir-black and IrO <sub>2</sub> . (A) OER polarization curves of the Nilr hollow structures and commercial Ir-black and IrO <sub>2</sub> measured in 0.5 M H <sub>2</sub> SO <sub>4</sub> before and after the durability test; (B) bar graphs displaying the overpotentials to drive 10 mA·cm <sup>-2</sup> ; (C) Ir mass activities at 1.51 V (vs. RHE); (D) Tafel plots before and after the durability test. ....	70
<b>Figure 32.</b> (A) Morphological characterization of the Nilr hollow nanoframe after the durability test and (B) the corresponding elemental mapping. ....	71
<b>Figure 33.</b> HAADF-STEM image of iridium product when the reaction is proceeded without manganese material. ....	74
<b>Figure 34.</b> SEM images with illustration for morphological change of MnO <sub>2</sub> nanowires as the heating temperatures; (A) pristine MnO <sub>2</sub> nanowires, and when heated to (B) 100 °C, (C) 220 °C. ....	75
<b>Figure 35.</b> XRD pattern for the pristine MnO <sub>2</sub> nanowires and MnO <sub>x</sub> particles after heating to 220 °C. ....	76
<b>Figure 36.</b> XPS spectra for (A) the pristine MnO <sub>2</sub> nanowires and (B) MnO <sub>x</sub> particles after heating to 220 °C. ....	77
<b>Figure 37.</b> The Pourbaix diagram for manganese. ....	78
<b>Figure 38.</b> Schematic illustration of the fabrication for IrO <sub>2</sub> nanospheres. ....	79
<b>Figure 39.</b> Morphological observation of IrO <sub>2</sub> nanospheres. (A) SEM image in low magnification, (B) HAADF-STEM images with elemental mapping, and (C) high-resolution HAADF-STEM image. ....	80
<b>Figure 40.</b> The crystallinity of IrO <sub>2</sub> nanospheres; (A) FFT patterns from high-resolution HAADF-STEM image and (B) XRD pattern. ....	81

<b>Figure 41.</b> XPS spectra for IrO <sub>2</sub> nanospheres compared with commercial IrO <sub>2</sub> (Alfa Aesar) in (A) Ir 4f and (B) O 1s region.....	82
<b>Figure 42.</b> Electrochemical measurements of IrO <sub>2</sub> nanospheres by comparison with commercial IrO <sub>2</sub> (Alfa Aesar). (A) OER polarization curves measured in 0.5 M H <sub>2</sub> SO <sub>4</sub> before and after chronoamperometry (CA) test for 5 hours (till 1.6 V vs. RHE); (B) Ir mass activities at 1.51 V (vs. RHE); (C) bar graphs displaying the overpotentials to drive 10 mA·cm <sup>-2</sup> before and after the CA test; (D) Tafel plots derived from OER polarization curves. ....	84
<b>Figure 43.</b> Cyclic voltammograms for IrO <sub>2</sub> nanospheres and commercial IrO <sub>2</sub> (Alfa Aesar).....	85
<b>Figure 44.</b> (A, B) High-resolution HAADF-STEM images of IrO <sub>2</sub> nanospheres after the durability test, and (C) elemental mapping by EDX. ....	87
<b>Figure 45.</b> The color change of solution for 15 seconds from the moment that the reducing agent (NaBH <sub>4</sub> ) was added. ....	90
<b>Figure 46.</b> The change in transparency of the reaction solution after two days. ....	91
<b>Figure 47.</b> Schematic illustration describing the mechanism for the fabrication of Ir-Ni aerogel. ....	92
<b>Figure 48.</b> Morphological observation of Ir-Ni aerogel. (A) Photos after synthesis, (B) SEM image, and (C) HAADF-STEM image with elemental mapping for iridium (green) and nickel (red) by EDX. ....	94
<b>Figure 49.</b> (A) High-resolution HAADF-STEM image of Ir-Ni aerogel with core-shell structure and (B) elemental mapping by EDX for iridium (green) and nickel (red) in a different reaction condition with a faster reaction rate. ....	95
<b>Figure 50.</b> XRD pattern of Ir-Ni aerogel. ....	95
<b>Figure 51.</b> X-ray photoelectron spectra of Ir-Ni aerogel in the (A) Ir 4f, (B) Ni 2p <sub>3/2</sub> , (C) O 1s regions. ....	97
<b>Figure 52.</b> Electrochemical measurements of Ir-Ni aerogel by comparison with commercial IrO <sub>2</sub> (Alfa Aesar). (A) OER polarization curves measured in 0.5 M H <sub>2</sub> SO <sub>4</sub> before and after stability test; (B) Ir mass activities at 1.51 V (vs. RHE); (C) bar graphs displaying the overpotentials to drive 10 mA·cm <sup>-2</sup> and (D) Tafel plots before and after the stability test. ....	99
<b>Figure 53.</b> Single cell testing of Ir-Ni aerogel with continuous scanning for 70 cycles	

with 1.0 mg·cm <sup>-2</sup> of loading by comparison with commercial IrO <sub>2</sub> (1.1 mg·cm <sup>-2</sup> ).....	101
<b>Figure 54.</b> Nyquist plots recorded from 1.45 V to 1.80 V for every 0.05 V for the single cell (A) before and (B) after testing.....	102
<b>Figure 55.</b> The current density of Ir-Ni aerogel during the long-term stability test by applying 2.0 V for 500 hours. ....	103
<b>Figure 56.</b> (A, B) Cross section observation for MEA before and after testing and (C, D) the corresponding elemental mapping for iridium marked as blue color. (E, F) Enlarged anode side. ....	104
<b>Figure 57.</b> (A) Surface morphology of anode side after testing and (B) the corresponding backscattered image.....	105
<b>Figure 58.</b> XRD measurements for the anode side before and after testing.....	106
<b>Figure 59.</b> XPS spectra for the anode before and after testing in (A) Ir 4f region and (B) O 1s region.....	107

## List of Tables

<b>Table 1.</b> Standard reduction potential for metals mostly used. <sup>96</sup> .....	27
--	----





Band / Volume 630

**Elucidation of Barocaloric Effect in Spin Crossover Compounds**

H. Shahed (2024), x, 261 pp

ISBN: 978-3-95806-758-5

Band / Volume 631

**Computational Investigation of Solvation Phenomena  
at Metal-Electrolyte Interfaces**

O. Cheong (2024), xvii, 142 pp

ISBN: 978-3-95806-759-2

Band / Volume 632

**Senkung zukünftiger Stickoxid- und Partikelemissionen in Nordrhein-  
Westfalen durch den Einsatz alternativer Energieträger und Antriebe**

J. L. Breuer (2024), vii, 339 pp

ISBN: 978-3-95806-760-8

Band / Volume 633

**Development of Model-Based Correction Methods for Temperature-  
Dependent Electromagnetic Induction (EMI) Measurement Errors in Soil  
Conductivity Estimations**

T. M. Tchantcho Amin (2024), xx, 100 pp

ISBN: 978-3-95806-761-5

Band / Volume 634

**Investigation and implementation of improved and degradation-tolerant  
fuel electrodes for solid oxide cells**

A. Schwiers (2024), VI, 163, XIII pp

ISBN: 978-3-95806-762-2

Band / Volume 635

**In Situ Time Calibration for Stationary Multichannel  
GPR Monitoring Systems**

L. Steinbeck (2024), xvi, 98, xxxi pp

ISBN: 978-3-95806-767-7

Band / Volume 636

**Erneuerbares Methanol als Ausgangsstoff für die Bereitstellung  
von flüssigen Kraftstoffen für den Transportsektor**

F. Schorn (2024), VI, 275 pp

ISBN: 978-3-95806-769-1

Band / Volume 637

**Investigation of Lower Boundary Conditions of Brominated  
Very Short-lived Species (VSLs)**

S. Zheng (2024), 2, iii, 160 pp

ISBN: 978-3-95806-770-7

Band / Volume 638

**Modellgestützte Analyse zukünftigen Mobilitätsverhaltens**

J. P. Reul (2024), XVI, 291 pp

ISBN: 978-3-95806-771-4

Band / Volume 639

**Insights into Mechanisms of Secondary Organic Aerosol Formation:  
Approaching Atmospherically Relevant Conditions  
in an Atmospheric Reaction Chamber**

Y. Baker (2024), XVII, 122 pp

ISBN: 978-3-95806-776-9

Band / Volume 640

**Advancing the representation of agricultural systems  
in Land Surface Models: systematic model evaluations  
and technical model developments**

T. S. Boas (2024), xxi, 145 pp

ISBN: 978-3-95806-777-6

Band / Volume 641

**Imaging spatial and temporal soil water content variations of the soil-plant  
continuum using ground penetrating radar**

L. Lärm (2024), xii, 303 pp

ISBN: 978-3-95806-778-3

Band / Volume 642

**Development of Iridium-based Nanostructures for Oxygen Evolution  
Reaction in PEM Water Electrolysis**

S. Park (2024), 135 pp

ISBN: 978-3-95806-779-0

Weitere **Schriften des Verlags im Forschungszentrum Jülich** unter  
<http://wwwzb1.fz-juelich.de/verlagextern1/index.asp>



Energie & Umwelt / Energy & Environment  
Band / Volume 642  
ISBN 978-3-95806-779-0

Mitglied der Helmholtz-Gemeinschaft

